QUANTUM OPTICS WITH ULTRA-COLD ATOMS

by

Lin Li

A dissertation submitted in partial fulfillment
of the requirements for the degree of
Doctor of Philosophy
(Physics)
in the University of Michigan
2016

Doctoral Committee:

Professor Alex Kuzmich, Chair
Professor Paul R. Berman
Associate Professor Hui Deng
Professor Georg A. Raithel
Professor Duncan G. Steel

To my parents

ACKNOWLEDGMENTS

I would like to start by thanking my advisor, Professor Alex Kuzmich, for his encouragement, guidance, and support during the course of my PhD. Alex has high standards and great enthusiasm in research, and as a result, he nourishes an incredibly motivating atmosphere for the lab. Alex has been a great mentor for me. He is very open to new ideas and always able to give me valuable suggestions no matter what topic I bring to him. His deep insight in experiments, great ideas, and optimism towards new research have been a continuous source of inspiration to me.

I am also indebted to Yaroslav Dudin for his invaluable help during the early years of my research. With his continuous guidance and participation, I built my first experimental setup from scratch during my first year in the lab and learned much from him about lasers, optics and electronics, and atomic physics in general. Yarik is also a great friend, helping me through the transition to a new environment. I enjoyed working with Yarik and I would like to thank him for his continuous support and friendship.

I would also like to thank Prof. Paul Berman, Prof. Georg Raithel, Prof. Duncan Steel, Prof. Hui Deng, Prof. Luming Duan and Prof. Finn Larsen for their support during my time at U of M.

I am grateful to all the past members of our research group: Alexander Radnaev, Corey Campbell, Alexander Arakelyan, Michal Piotrowicz, Ran Zhao, Shau-Yu Lan, Dima Matsukevich and Thierry Chaneliere. I had the pleasure of overlapping with Alex Radnaev and Corey Campbell during the first couple years of my PhD. Both of

them were very helpful while I was building the quantum memory experiment and I am very thankful for that. All of the Rubidium experiments in our lab build on the foundation laid by Dima, Thierry, Shau-Yu and Ran and I would like to thank them for that.

Thank you to all the current members of our lab: Pengbo Zhang, Jacob Lampen, Siwen Li, Jacob Curtis, and Jiachang Liu. I enjoyed working with them and I wish them the best with future experiments.

Last but not least, I would like to thank my parents, my grand-parents and all my friends for their unconditional support and encouragement. A special thank you goes to Mingjie Liu for her company through the ups and downs in my PhD.

TABLE OF CONTENTS

LIST OF FIGURES

LIST OF TABLES

ABSTRACT

The advances in laser cooling and trapping techniques allow samples of ultra-cold atoms to be created and controlled for the study of quantum physics. In this thesis, we focus on using ensembles of cold atoms to investigate novel quantum effects and their applications in quantum optics.

Realization of a scalable intercontinental quantum system, e.g. a global quantum internet, relies on quantum memories with long lifetimes on the order of seconds. We have reduced the differential light shifts of the atomic ground states to a sub-Hz level and achieved a lifetime of 16 seconds. Achieving fast and efficient quantum operations, on the other hand, requires strongly-interacting systems. We explore highly excited Rydberg atoms towards this goal and demonstrate Rydberg excitation blockade, many-body Rabi oscillations, trapping of Rydberg atoms, deterministic single photon source, and atom-photon entanglement.

Finally, we integrate the two essential capabilities for quantum information processing, fast quantum state generation and long-term storage, by simultaneously exploiting Rydberg levels for interactions and ground atomic levels for the storage of quantum state.

Our work advances the control of coherence properties and interactions in cold atomic ensembles to a new level and opens new opportunities for studies of complex quantum systems.

CHAPTER I

Introduction

1.1 Overview

From the primitive use of lighting methods like torches and candles, to the commercially viable incandescent lightbulb produced by Thomas Edison, to the invention of optical fibers [1] and LEDs [2–4], efforts towards better understanding, generation, and control of light have revolutionized nearly every aspect of daily life. Due to the achievements in quantum mechanics theory and quantum optics, physicists are now able to study and engineer light at the single quantum level. The word "quantum" came from the Latin "quantus", which means "how many". In 1900, to address the nature of black-body radiation, Max Planck first introduced the concept of "energy quanta" in the emission and absorption processes [5]. In 1905, Albert Einstein borrowed Planck's idea of quanta to explain the photoelectric effect and further generalize it to "quanta of light" [6], which were later called "photons" by chemist Gilbert N. Lewis.

Although these works in the early 20th century laid the foundation of quantum mechanics, quantum optics did not become a separate field of study until the invention of lasers in 1960s. To understand the physical mechanisms behind lasing, quantum mechanics was applied to treatment of the transitions between atomic levels, while light fields were still described classically. This semi-classical approach turned out to be quite powerful and explained most phenomena in laser physics and nonlinear

optics at the time. However, to investigate the fundamental properties of light, for example its high-order intensity correlations, the quantization of the light field had to be introduced. Accompanying the development of quantum optics theory, advances in photon detection allowed experimental observations of important phenomena such as the bunching and anti-bunching of light.

Over the past few decades, various systems have been adopted for studying quantum optics. Spontaneous parametric down conversion (SPDC) was used for the generation of single photons and entangled photon pairs [7]. Notable experiments such as the violation of Bell's inequalities [8] and quantum teleportation [9] were demonstrated with SPDC. With the development of laser cooling and trapping techniques, atomic systems (single atoms, ions and atomic ensembles) became attractive for studying new quantum effects. The scope of quantum optics has broadened ever since. The achievable strong interactions and exquisite quantum control in atomic systems allow effective quantum engineering of atomic and even photonic states. These capabilities have opened paths to a number of important research directions, such as long distance quantum communication, quantum computing, quantum many-body simulation, and precision measurements. Artificial atoms in solid state systems such as NV-centers [10], quantum dots [11], and superconducting circuits [12] are also promising, given their potential scalability. Hybrid quantum approaches involving two or more physical systems are also being actively explored [13].

In this thesis, I present our recent experimental results in using ultra-cold atomic ensembles to study quantum-optical phenomena. Ground states of cold atomic ensembles are excellent memories for photons because of their long coherence time and efficient storage-retrieval capability. By using the magic-valued magnetic field technique and the dynamical decoupling protocol, we have realized a quantum memory for light with an ultra-long lifetime of 16 seconds [14]. However, the weakly-interacting nature of the ground state levels only allows probabilistic protocols for quantum state prepa-

ration. For example, single photon sources can be realized within ground states using probabilistic approaches, like the Duan-Lukin-Cirac-Zoller (DLCZ) protocol [15], but these "repeat-until-success" protocols take up to a few milliseconds to generate a single photon [16]. The implementation of fast and unconditional quantum operations requires controllable, strong, and long-range interactions. We have studied Rydberg atoms, atoms in their highly excited electronic states, for this purpose. Strongly interacting Rydberg atoms provide an excellent platform for the investigation of many-body physics, quantum information science and precision measurements. We have demonstrated the Rydberg excitation blockade, the observation of many-body Rabi oscillations [17], magic trapping of Rydberg atoms, a deterministic single photon source, atom-photon entanglement [18], and most recently a quantum memory with strong and controllable interactions [19].

The rest of the thesis is structured as follows:

• Chapter I. We first review the topic of quantum statistics of light fields. The scientific motivations and accomplishments of employing cold atom systems for studying quantum physics are then discussed. The advantages and recent achievements in quantum optics with strongly-interacting Rydberg atoms are reviewed. We conclude by introducing the Rydberg blockade effect and the deterministic single photon generation protocol based on it.

• Chapter II. Our experiment on ultra-long-lived quantum memory is presented. Realization of scalable intercontinental quantum systems requires long lifetimes (seconds) for ground-level coherences of atomic ensembles. By engineering an optical lattice free of differential Stark shifts and employing Carr-Purcell-Meiboom-Gill (CPMG) dynamical decoupling sequence, we extend the ground states coherence time into the regime of a minute [14].

• Chapter III. Achieving Rydberg blockade is at the heart of many determinis-

tic quantum operations. By performing two-photon excitation to high-lying Rydberg states, we demonstrate Rydberg blockade for an ensemble containing a few hundred atoms. Many-body Rabi oscillations and the accompanying $\sqrt{N}$ enhancement in the Rydberg blockade regime [17] are observed for the first time.

• Chapter IV. One of the major limitations in quantum optics with Rydberg atoms is that the Far Off-Resonance Traps (FORTs), that are attractive for ground states would generally be repulsive for Rydberg states. Therefore, they have to be switched off in order to maintain the coherent character of the Rydberg excitation process, resulting in fast atom loss and a limited degree of quantum state control. To overcome this obstacle, we realize a state-insensitive trap which allows simultaneous trapping of both Rydberg and the ground states. With this trapping technique, we implemented a single photon source with $\sim$ 5 kHz photon generation rate [18].

• Chapter V. Achieving atom-photon entanglement in mesoscopic ensembles with Rydberg interactions is critical for atomic-ensemble-based quantum repeater architectures [20–23]. By taking advantage of the Rydberg blockade, we demonstrate the generation of entanglement between light and an optical atomic excitation in a nearly deterministic way [18].

• Chapter VI. Strongly-interacting Rydberg states usually have relatively short lifetimes, due to their magnified sensitivity to black-body radiation, ambient electric fields, and the limitation from spontaneous emission, atomic motion, and collisions. In contrast, ground atomic states are ideal for preserving quantum coherence, but implementation of fast and deterministic quantum operations is challenging due to their weak interactions. Here, we demonstrate the simultaneous achievement of fast quantum operations and long coherence times by employing Rydberg levels for interactions and ground atomic levels for storage [19]. Instead of the two-photon Rydberg excitation scheme used for previous works, a UV laser at 297 nm is employed for the direct optical coupling of ground state to Rydberg *p*-state. A quantum memory capable of

sub-μs quantum state generation and long-term storage is realized.

• Chapter VII. We review the protocols and techniques developed, summarize the experimental results that are achieved in this thesis, and give an outlook for future works.

1.2 Quantum statistics of light

The continuing efforts in generation and manipulation of non-classical light fields have led to a broad range of important quantum protocols. One of the immediate applications is quantum cryptography. Photons are the best messengers for quantum information because of their non-interacting nature and the ability to travel at light speed. Quantum information can be encoded in the polarization of a photon as $|\Phi\rangle = \alpha|H\rangle + \beta|V\rangle$. Recently, orbital angular momentum of light (OAM) was also explored for quantum information encoding [24]. By using quantum key distribution schemes, for example the iconic *BB*84 protocol [25], intrinsically secure communications can be realized. A quantum computer enabled by single photons and linear optics has also been proposed and pursued [26]. Moreover, non-classical states of light, for example squeezed light states and photonic Fock states, are critical for quantum metrology protocols, as they can greatly enhance the sensitivity of precision measurements [27].

The prerequisite for all the quantum optics applications is to understand the quantum nature of light. Intensity correlation measurements are powerful tools that have been applied to study the quantum statistics of light. In the early 1900's, Young's double-slit experiment was used in the attempt to observe quantum effects at the single photon level. However, no new effects were observed in the experiment, since classical wave theory and quantum theory give the same predictions for the first order coherence of light. The second order coherence of light wasn't observed until the Hanbury

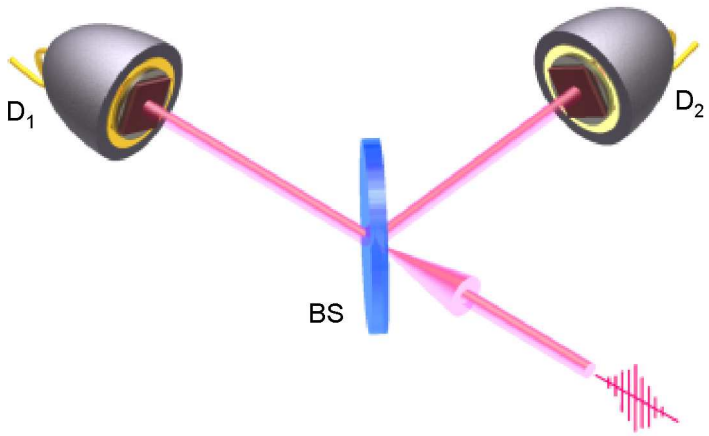

Figure 1.2.1: **Hanbury Brown-Twiss method**. Illustration of a setup using the HBT-type method measuring the second order intensity correlations.The light field is split by the BS and detected at the two detectors. The photoelectric detection events at detectors D_1 and D_2 are cross-correlated.

Brown-Twiss (HBT) method was introduced to the field of quantum optics. Named after astronomers R. Hanbury Brown and R. Q. Twiss, the method was initially proposed as a stellar interferometer for measuring the angular size of stars [28] and then used to measure the intensity correlations from a thermal light source (a mercury arc lamp) [29].

Figure 1.2.1 shows an illustration of measure the second order intensity correlations with the Hanbury Brown-Twiss method. A light field is split by a 50/50 beam-splitter (BS) and subsequently detected by two detectors D_1 and D_2. The HBT method measures the delayed coincidence probability $P_{12}(\tau)$, which represents the probability of having a detection event from detector D_1 at time t and another event from detector D_2 at time $t+\tau$. It is remarkable that such a simple yet elegant setup could reveal

some of the most profound properties of light and is still employed today as one of the primary methods for the characterization of non-trivial photonic states. The second order coherence of light, or more specifically, the second order intensity correlation function $g^{(2)}(\tau)$ can be obtained from a coincidence measurement:

$$g^{(2)}(\tau) = P_{12}(\tau)/(P_1 P_2), \tag{1.2.1}$$

where $P_{1,2}$ is the detection probability for $D_{1,2}$.

For a single-mode quantized field, $g^{(2)}(\tau)$ can be expressed as:

$$g^{(2)}(\tau) = \frac{\langle n_1(t) n_2(t+\tau)\rangle}{\langle n_1(t)\rangle \langle n_2(t+\tau)\rangle}. \tag{1.2.2}$$

The second order correlation function at zero delay, $g^{(2)}(0)$, is of particular interest:

$$\begin{aligned} g^{(2)}(0) &= \frac{\langle n_1(t) n_2(t)\rangle}{\langle n_1(t)\rangle \langle n_2(t)\rangle} \\ &= 1 + \frac{(\Delta n)^2 - \langle n\rangle}{\langle n\rangle^2}, \end{aligned} \tag{1.2.3}$$

where $\langle n\rangle$ is the mean photon number, and $(\Delta n)^2 = \langle (n - \langle n\rangle)^2\rangle$ is the variance. From (1.2.3) it is obvious that $g^{(2)}(0)$ is closely related to the statistical fluctuation of the input light fields. According to their different statistical properties, light fields can be categorized into three classifications: Poissonian, super-Poissonian, and sub-Poissonian light.

For a coherent states of light, e.g. light pulses from a monochromatic and power-stabilized laser, statistical fluctuations of the photon number are dominated by the Poisson distribution, with the probability of detecting n photons:

$$p(n) = e^{-\langle n \rangle} \frac{\langle n \rangle^n}{n!}. \tag{1.2.4}$$

From (1.2.4) one can get $(\Delta n)^2 = \langle n \rangle$ and, as a result, $g^{(2)}(0) = 1$.

For light with super-Poissonian statistics, the variance $(\Delta n)^2 > \langle n \rangle$ leads to $g^{(2)}(0) > 1$. Light fields with super-Poissonian statistics are usually incoherent (at least partially incoherent) and have a classical interpretation of light with time-varying intensity, e.g. thermal light. The situation where $g^{(2)}(0)$ larger than unity is also termed photon-bunching, where photon pairs tend to arrive at the detector together.

Unlike coherent light and bunched light, light fields with sub-Poissonian statistics have no classical equivalent and thus are often called non-classical light states. Sub-Poissonian distribution results in $g^{(2)}(0) < 1$ (photon anti-bunching). For photon number states (Fock states), the variance $(\Delta n)^2 = 0$. As a result,

$$g^{(2)}(0) = 1 - \frac{1}{n}. \tag{1.2.5}$$

For a single photon state, $g^{(2)}(0) = 0$, which means the quality of a single photon source can be easily characterized by measuring the value of $g^{(2)}(0)$ with a simple HBT setup.

1.3 Quantum physics with cold atoms

Ultra-cold atoms are ideal systems for the study of quantum physics. They offer clean platforms that are isolated from the environment, which can be well-understood and controlled. To store and process quantum information, matter qubits are preferred over photons, as it is challenging to make photons interact with each other. The ground hyperfine sub-levels of cold atoms feature long coherence times and thus are excellent

candidates as matter qubits. Moreover, unlike many solid-state counterparts, atomic systems are spectroscopically identical, which is critical for direct interface between remotely located quantum nodes through light.

In principle, the quantum evolution of a many-body system can be directly solved using its Hamiltonian. However, the computational resources required for solving problems in many-body quantum system scale exponentially with the system size, making it extremely challenging to perform direct calculation for systems containing more than tens of spins. An alternative approach was proposed by Richard Feynman a few decades ago [30]. Quantum many-body problems could be emulated with a universal quantum simulator. In the past decade, atomic systems have been actively explored for purpose of quantum simulation. Ultra-cold atoms trapped in periodic potentials, like optical lattices, can be used to simulate the electron wavefunctions in a condensed-matter system. Combined with high-resolution imaging and single site addressing ability, ultra-cold quantum gases exhibit potential of realizing important quantum Hamiltonians [31].

Making use of the ultra-cold atoms, remarkable advances have also been made in the field of precision measurements including atom frequency standards, atom interferometry, fundamental physical constants measurements, fundamental physics principle tests, and other precision measurements. For example, the de Broglie wavelengths of ultra-cold atoms are considerably longer than that of thermal clouds. This allows the implementation of atomic interferometry, which has been widely used in navigation [32], measurement of fundamental constants, and even gravitational wave detection [33]. Furthermore, by taking advantage of the long-lived, narrow linewidth transitions in ions and neutral atoms, optical clocks with unprecedented precession have been demonstrated [34].

The achievable ultra-long coherence times between atomic ground-levels are of major importance for scalable entanglement distribution protocols. As promising can-

didates for quantum memories, ground states of an ultra-cold atomic ensemble can faithfully store a quantum state in the form of collective atomic excitation, also known as a spin-wave or a polariton, which can be mapped onto a light field in a phase-coherent way [35].

For the distribution of entanglement over continental length scales $L \sim 10^3$ km, it is desirable to have an efficient (low-loss) set of the following capabilities: generation of single photons and entangled memory-light states, long-term storage of light (quantum memory), integration with telecommunication wavelengths for quantum state transmission over optical fibers, and two-qubit quantum gates for entanglement purification.

Atomic ensemble-based approaches to quantum repeaters seem to be attractive, as they have the potential for these capabilities. Generation of single photons from an atomic ensemble has been first achieved within the probabilistic, DLCZ approach [15], albeit with long, millisecond-scale generation times [16, 36]. More recently, a deterministic single photon source has been demonstrated using strong Rydberg interactions in a mesoscopic ensemble of a few hundred atoms, with microsecond-scale generation times [37]. Entanglement of memory and light has also been demonstrated [38–40]. Deterministic atom-light entanglement has recently been achieved using Rydberg atoms [18]. A conversion of quantum fields between storable and telecom wavelengths with efficiencies in excess of 60% and memory telecom light entanglement have been demonstrated in Refs. [41, 42]. The atom-photon and photon-photon gates based on high finesse cavities and Rydberg interactions [43–45] are being actively explored.

1.4 Rydberg atoms

Efficient quantum state preparation and implementation of quantum gates require strongly interacting systems. Cavity QED [46] and collision induced spin exchange [47, 48] have been exploited towards this goal. Alternatively, atoms in highly excited Rydberg states feature long-range and strong interactions that can be conveniently switched on and off, opening the door to fully deterministic quantum operations [49, 50]. When an atom is promoted into a Rydberg level with a principal quantum number n, the valence electron is in an orbit that is $\sim n^2$ larger than that of the ground-level atom. The atomic dipole moment is correspondingly larger, so that the interaction of two atoms is increased by $\sim n^4$ in the dipole-dipole regime and by $\sim n^{11}$ in the van der Waals regime [49, 51]. For an atom pair separated $\lesssim 10$ μm, excitations to high-lying Rydberg states ($n \gtrsim 70$) results in the interaction strength $V \gtrsim 1$ MHz, allowing sub-μs entanglement protocols. Significant advances have been made in employing Rydberg interactions for entanglement of pairs of neutral atoms [52–54] and study many-body physics [55, 56].

An ultra-cold atomic ensemble in a quantum superposition of a ground and Rydberg state allows both for a fast and deterministic preparation of quantum states and their efficient transfer into single-photon light fields [37, 57, 58]. Motivated by these considerations, ultra-cold gases coupled to Rydberg levels have been studied with an eye towards scalable quantum networking architectures [20–23]. Notable achievements include demonstration of deterministic Rydberg single-photon sources [37, 57], atom-photon entanglement [18], many-body Rabi oscillations [17, 59–61], photon anti-bunching and interaction-induced phase shifts [62, 63], single-photon switch [58] and transistors [64, 65].

For two nearby atoms (separated by $\lesssim 10$ μm), the Rydberg-Rydberg interactions could be sufficiently strong that one excited atom prevents the excitation of the other,

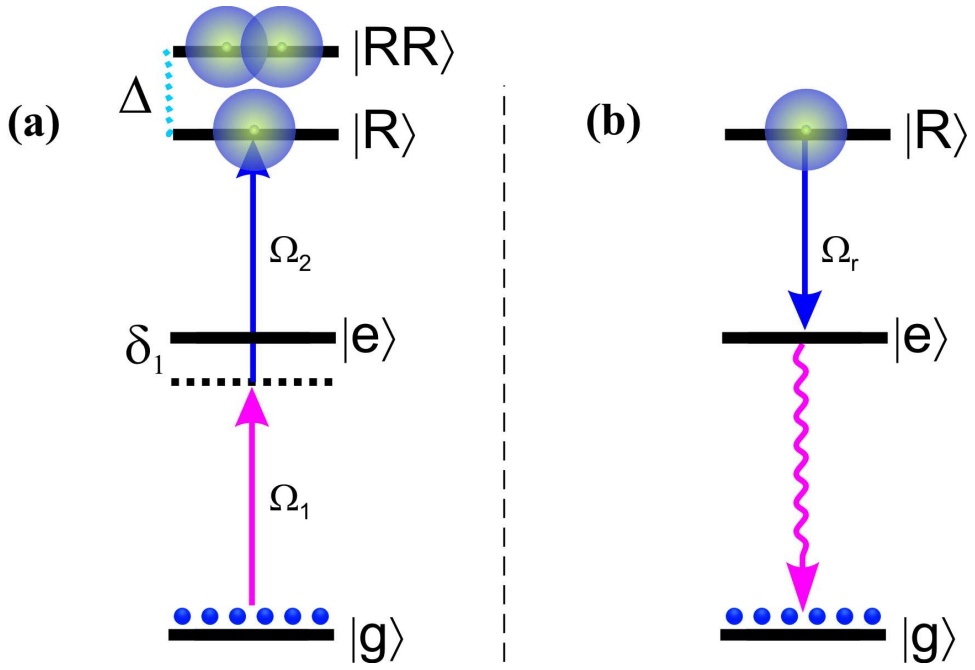

Figure 1.4.1: **Rydberg blockade and single photon source. (a)**. Illustration of Rydberg excitation blockade. Excitation to Rydberg states is performed by the laser fields Ω_1 and Ω_2. Strong inter-atomic interactions shift the resonant frequencies of double excitations away from single excitation spectrum. **(b)**. Deterministic single-photon generation enabled by Rydberg interaction.

giving rise to the "dipole blockade" effect [50, 66]. The illustration of the blockade effect is shown in Figure 1.4.1 (a). Rydberg excitation is performed by two-photon excitation with laser fields Ω_1 and Ω_2. The Ω_1 and Ω_2 fields are detuned from the intermediate state $|e\rangle$ by two-photon detuning δ_1 to avoid decoherence due to spontaneous emission. A singly excited Rydberg state $|R\rangle$ is created if the interaction-induced spectrum shift Δ for Rydberg pair state $|RR\rangle$ is larger than the spectrum width of the excitation lasers. The singly excited $|R\rangle \equiv 1/\sqrt{N}\sum_{j=1}^{N}|g\rangle_1...|r\rangle_j...|g\rangle_N$ is a W state in which one atom out of the N atoms in the ensemble is in the Rydberg level $|r\rangle$.

One direct and important application of Rydberg blockade is a deterministic single photon source [37, 57, 66], as shown in Figure 1.4.1 (b). The Rydberg single excitation $|R\rangle$ can be transferred into a single photon by applying a laser field Ω_r resonant with an intermediate level. In many experiments, the intermediate level for retrieval is set to be

the same as the one used for excitation ($|e\rangle$). During the Rydberg excitation process, the Ω_1 and Ω_2 fields imprint a spatial phase grating on the Rydberg-ground coherence :

$$|R\rangle = 1/\sqrt{N}\sum_{j=1}^{N} e^{i\Delta\vec{k}\cdot\vec{r}_j}|g\rangle_1...|r\rangle_j...|g\rangle_N, \tag{1.4.1}$$

where $\vec{r}_j$ is the atomic position, the wave-vector mismatch is $\Delta\vec{k} = \vec{k}_1 + \vec{k}_2$, $\vec{k}_1$ and $\vec{k}_2$ are the wave-vector of the two excitation fields Ω_1 and Ω_2, respectively. When illuminated with the resonant read-out field Ω_r (see Figure 1.4.1 (b)), state $|R\rangle$ is transferred into state:

$$|E\rangle = 1/\sqrt{N}\sum_{j=1}^{N} e^{i(\Delta\vec{k}-\vec{k}_r)\cdot\vec{r}_j}|g\rangle_1...|e\rangle_i...|g\rangle_N, \tag{1.4.2}$$

where $\vec{k}_r$ is the wave-vector of the retrieving field. The atomic excitations in the intermediate state $|e\rangle$ would be converted into photons, with the probability of emitting into mode $\vec{k}$:

$$\begin{aligned} P(\vec{k}) &\propto 1/N|\sum_{j=1}^{N} e^{i\varphi_j}|^2 \\ &\sim 1/N|\sum_{j=1}^{N} e^{i(\Delta\vec{k}-\vec{k}_r-\vec{k})\cdot\vec{r}_j}|^2 \end{aligned} \tag{1.4.3}$$

When the wave-vector of the read out field Ω_r matches that of the field Ω_2, along the direction of $\vec{k} = \vec{k}_1$ the phases $\varphi_j \sim 0$ for all the atoms, leading to a collectively enhanced emission [66]. At the same time, the emissions into other modes are suppressed due to the averaging of random phases. As a result the single Rydberg excitation is converted into a single photon with the same spatial mode as the Ω_1 field.

CHAPTER II

Ultra-long-lived memory for photons

This chapter is based on Ref. [14].

2.1 Introduction

A quantum memory with lifetime on the time scale of seconds or even minutes is a crucial component for realization of scalable inter-continental lengths scale quantum systems. It requires suppression of broadening between the energy levels of an optically thick material medium to a sub-Hz level. We use an optically confined ultra-cold atomic gas with compensation of differential Stark shifts a magnetic field of "magic" value 4.20(2) G and employ dynamical decoupling microwave pulse sequence between the two hyperfine ground levels to realize such a medium. We employ it to achieve storage and retrieval of coherent states of light on the one minute scale, with 1/e lifetime of 16 s. Our results represent the longest light storage in atomic systems to date, a significant advance on the previous value of ~ 0.3 s in ultra-cold atoms and the ~ 1 s solid-state storage. The experiment is done in the low-noise regime similar to the previous realization of 0.1 s quantum memory, making our system suitable for scalable quantum networking applications. The achieved long coherence times are also promising for implementations of compact microwave clocks, measurements of ground-level polarizabilities, and other types of precision measurements.

2.2 EIT and light storage

While photons are the best messengers of quantum information, it's difficult to localize and store them. To achieve a practical quantum network, ideally we would like to efficiently store photons into the local matter qubits in each node for quantum states manipulation and map them back into photons at desired time with low losses. This requires coherent absorption and re-emission of photons by matter qubits and preserving the coherence during the storage. A dense and cold atomic ensemble is an excellent candidate since it can interact strong with photons and provide long storage time.

Atomic ensemble can be used as an efficient quantum memory for light by taking an advantage of the Electromagnetically Induced Transparency (EIT). As shown in Figure 2.3.1, a weak probe light connects the atomic ground state $|a\rangle$ to the electronically excited $|e\rangle$, which is strongly coupled to another ground state $|b\rangle$ by a control field. The probe light, usually at the level of signal photons, is much weaker than the control field. In this case, the susceptibility of the media can be effectively modulated with the intensity of the control field. When propagating in such medium, the probe light is coupled with the wave of flipped atomic spins, forming dark-state polariton (DSP) which is a superposition of photons and atomic spin-wave. By adiabatically turning off the control field, the group velocity of the DSP can be reduced to zero which means the DSP becomes purely atomic spin-wave and photonic quantum state is successfully stored into atomic levels. The stored states can be retrieved by simply turning on the control field and re-accelerating the DSP into photonic state.

In order to achieve ultra-long lifetime for light storage, it's important to understand the sources of decoherence that limit the storage time in atomic ensemble. After the storage process, the probe field is converted to a collective excitation ("spin-wave") [35]. For the i-th atom in the ensemble, its excitation amplitude is proportional to $e^{-i(\vec{k}_c-\vec{k}_p)\vec{r}_i}$, where $\vec{k}_c$ and $\vec{k}_p$ are the wave vector of the control and probe field, and $\vec{r}$ is

the atomic position. The storage process imprints a momentum of $\hbar\Delta\vec{k} = \hbar(\vec{k}_c - \vec{k}_p)$ on the atoms, thus generating a phase grating along the $\Delta\vec{k}$ direction. In our experiment, the spin-wave grating has a period of $\Lambda \approx 2\pi/|\Delta\vec{k}| = 35\ \mu m$. The phase coherence between atoms in the spin-wave grating has to be preserved in order to achieve long coherence times.

For a gas of atoms of mass M at a temperature T, the particle speeds are described by the Maxwell-Boltzmann distribution:

$$f(v) = (m/2\pi K_B T)^{-3/2} e^{-mv^2/2K_B T} \tag{2.2.1}$$

For an atom with velocity $\vec{v}_j$, the motional-induced phase accumulates as $\varphi_j = \Delta\vec{k}\vec{v}_j t$. During the read-out process, the probability η of converting the atomic excitations into the mode-matched optical fields is [67]:

$$\begin{aligned} \eta &\propto |\sum_j f(v_j) e^{i\varphi_j}|^2 \\ &\sim |\int e^{-mv^2/2K_B T} e^{i\Delta k v t} dv|^2 \\ &\sim e^{-t^2/\tau^2}, \end{aligned} \tag{2.2.2}$$

where the motional dephasing time $\tau = \sqrt{m/K_B T}/\Delta k = \Lambda/(2\pi\sqrt{k_B T/M})$.

To prevent the motional dephasing, we confine the atoms in a one dimensional optical lattice along the direction of the spin-wave with a period of 3.2 μm. However, the 1064 nm YAG laser fields for the optical lattice create a differential ac-Stark shift on the ground hyperfine states because of the 6.8 GHz difference in detuning. The dipole trapping potential $U(\mathbf{r})$ is closely related to detuning δ_t of the trapping field:

$$U(\mathbf{r}) \propto I(\mathbf{r})\Gamma/\delta_t, \tag{2.2.3}$$

where Γ is the spontaneous decay rate of the excited state, $I(\mathbf{r})$ is the intensity of trapping field, and $\delta_t = \omega_0 - \omega_t$ is the detuning. Here ω_0 and ω_t are the frequencies of atomic resonance and trapping light. The hyperfine splitting of $5S_{1/2}$ state (δ_{hfs} = 6.8 GHz) leads to different trapping laser detunings for $F = 1$ and $F = 2$ levels, Figure 2.2.1 (a). As a result, atoms in different levels experience spatially dependent differential light shifts, as shown in Figure 2.2.1 (b):

$$\begin{aligned} \Delta U(\mathbf{r}) &= U(\mathbf{r}, \delta_t) - U(\mathbf{r}, \delta_t + \delta_{hfs}) \\ &\sim \frac{\delta_{hfs}}{\delta_t} U(\mathbf{r}) \end{aligned} \tag{2.2.4}$$

This causes a spatial inhomogeneity and decoheres the spin-wave on the time scale of a few milliseconds. A bias magnetic field at the "magic" value can be exploited for the compensation of the differential light shifts. Other effects like the uncompensated field gradient can also cause inhomogeneous broadening and destroy ensemble coherence. We employ the CPMG decoupling sequence to effectively decouple our stored sates from these inhomogeneous broadenings.

2.3 Experimental setup and protocol

The essential elements of the experimental setup are shown in Figure 2.3.1. A cigar-shaped optically dense sample of cold ^{87}Rb atoms is prepared in optical lattice. Atomic population loss is one of the major limits on the lifetime of light storage in optical lattice. In this work, the double chamber system allows us to have efficient loading

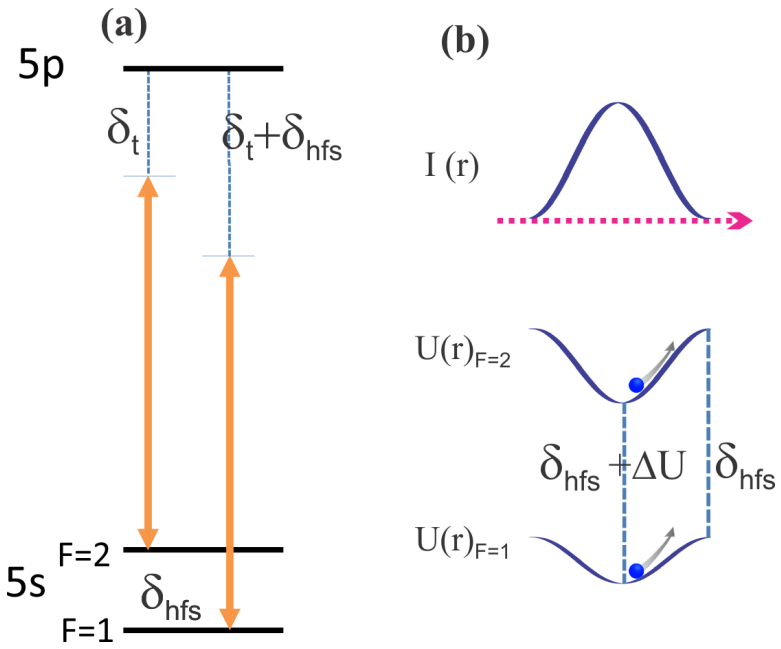

Figure 2.2.1: **Differential AC Stark shifts. (a),** F=1 and F=2 levels have different detunings for the same trapping field. **(b),** Atoms in the two hyperfine levels experience different trapping potentials due to the 6.8 GHz splitting.

and cooling of atoms into lattice while keeping the vacuum pressure at $\sim 10^{-11}$ Torr level, which leads to an ultra-long lifetime for polarized sample in $F = 1$ hyperfine state.

In our 2D$^+$-MOT setup, a quadrupole magnetic field with a gradient of 18 G/cm perpendicular to the axis of the flux is generated by two pairs of race-track-shaped anti-Helmholtz coils around the cell. Two circularly polarized beams with an elliptical cross section are retro-reflected such that the four beams are perpendicular to each other and to the flux axis. The transverse beams and the 2D quadrupole magnetic field work together as two-dimensional magneto-optical cooling, which transversely cools and compresses the atomic beam. The magnetic field in the axial direction is quasi-zero.

A pair of linearly polarized and circular sized laser beams, known as the pushing beam and the retarding beam, are used for the axial optical molasses cooling. The

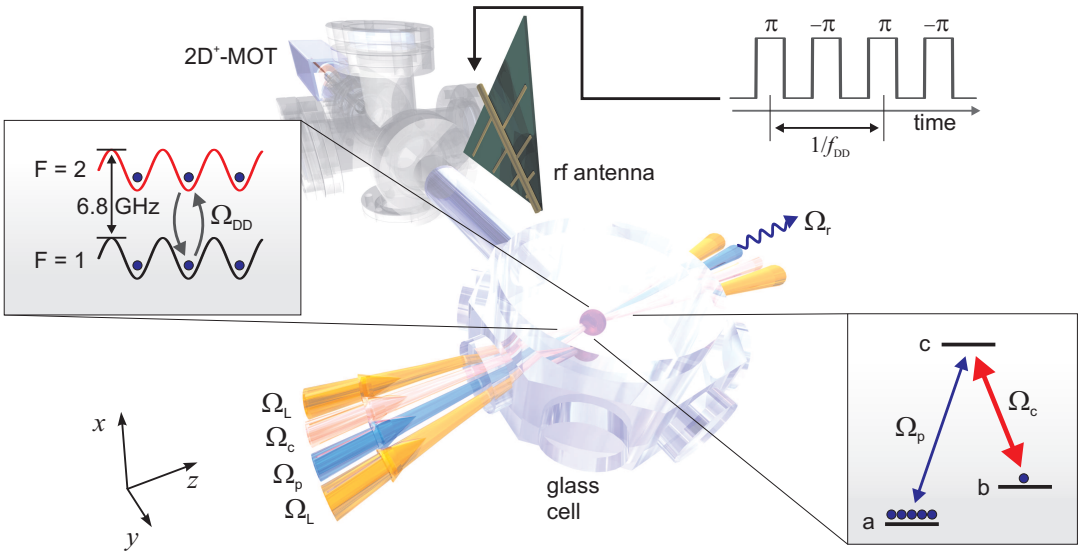

Figure 2.3.1: **Essential elements of the experimental setup.** A 2D$^+$-MOT produces a cold atomic beam to load a 3D-MOT in the differentially-pumped glass cell with anti-reflection-coated windows. The 3D-MOT is used to produce a dense sample of cold ^{87}Rb atoms in a one-dimensional optical lattice formed by two 1064 nm Ω_L fields. Atomic levels used in the experiment are shown in the inset. A probe pulse Ω_p is converted into an atomic spin wave by adiabatically switching off the control field Ω_c. After a storage period T_s, the spin wave is retrieved into a phase-matched direction by turning the probe field back on. The lattice confines the atoms in the field maxima, minimizing spin-wave motional dephasing. The differential ac-Stark shift produced by the lattice is nulled by setting the bias magnetic field to a "magic" value. A dynamical decoupling sequence of the microwave π pulses on the clock transition is used to extend storage time.

axial cooling allows the atomic beam to have a lower mean velocity and velocity distribution width. The angular divergence is also reduced, since atoms spend more time in the transverse cooling beams. This enables efficient loading of atoms into the 3D MOT without any further cooling. The intensity balance between the transverse beams together with separate current control for each coil allows for precise alignment of the atomic beam through the aperture. The trapping beams are red-detuned 20 MHz from the $5s_{1/2}, F = 2 \leftrightarrow 5p_{3/2}, F = 3$ transition in ^{87}Rb, a laser beam with 4 mW power and locked to $5s_{1/2}, F = 1 \leftrightarrow 5p_{3/2}, F = 2$ transition in ^{87}Rb is used as the repumper. The 2D magnetic field gradient, power balance of transverse beams, pushing and retarding

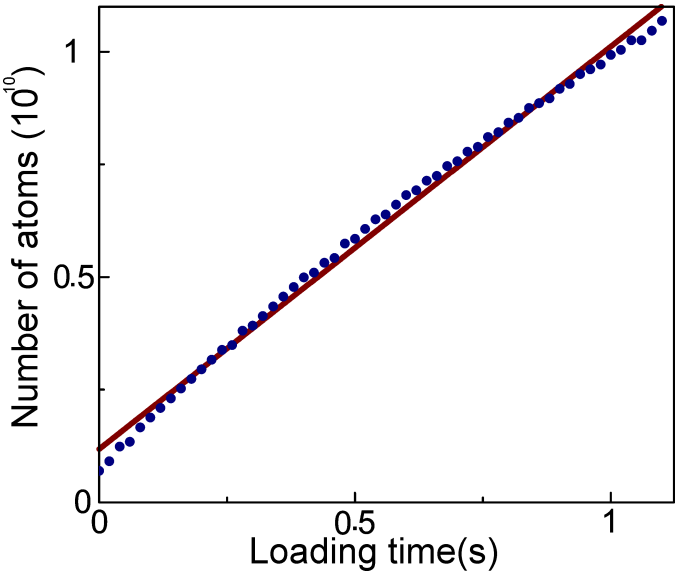

Figure 2.3.2: **Measurement of 3D MOT loading time.** The number of atoms in the 3D MOT is shown as a function of loading time. Fluorescence signal from 3D MOT are recorded for calculating atom number. The linear fit gives a loading rate of 8.9×10^9 atom/s.

beams, and their detuning can be changed to optimize the loading of atoms in to the science cell. The fluorescence of the 3D-MOT is collected by an optical detector for analyzing the loading rate. When the parameters are optimized, the 2D MOT gives a loading rate of 9×10^9 atom/s, a 3D-MOT of more than 10^{10} atoms can be loaded in 1.2 seconds, as shown in Figure 2.3.2.

To prepare the atomic sample, atoms are loaded from the 3D-MOT into an optical lattice. The 3D-MOT is formed by three pairs of circularly polarized beams perpendicular to each other. After the 3D-MOT loading the atoms undergo sub-Doppler cooling and are transferred into a 1-D optical lattice. The lattice is formed by interfering two 1064 nm YAG laser beams at an angle of 18° in the horizontal plane. The two lattice beams have waists of 170 μm and a total power of 12.5 W, resulting in the maximum lattice depth of 78 μK, with the corresponding trap frequencies of $(1.3 \times 10^4, 110, 20)$ Hz in (*x*,*y*,*z*) dimension. For the $\sim$ 22 ms after the 3D MOT loading, the gradient of the 3D MOT is increased to $\sim$ 25 G/cm to compress and load the atoms into the optical

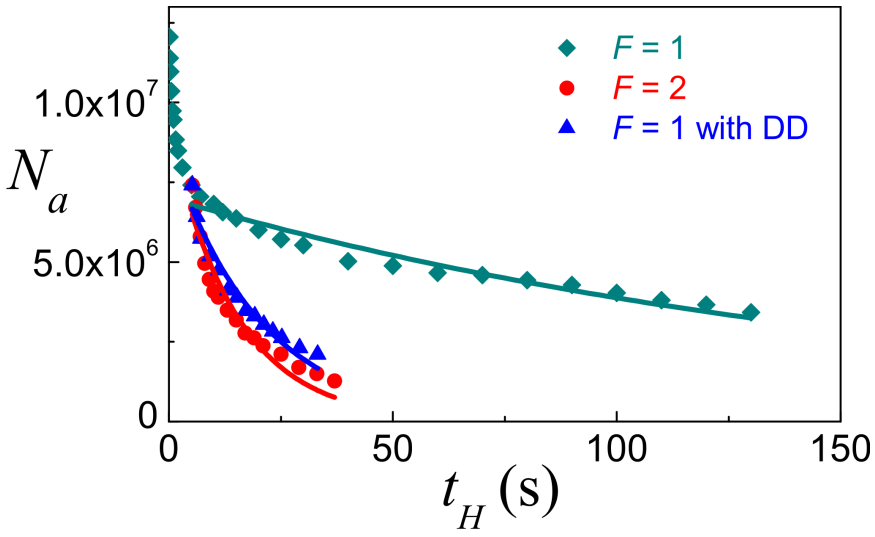

Figure 2.3.3: **Lifetime of atoms in the optical lattice.** Number of lattice-trapped atoms N_a is shown as a function of the holding time t_H. The data are for atoms prepared in $5S_{1/2}, F = 1$ (diamonds), $5S_{1/2}, F = 2$ (circles), and $5S_{1/2}, F = 1$ when the dynamical decoupling sequence is applied (triangles). The data are fit with an exponential function $\propto \exp(-t_H/\tau)$ starting from $t_H = 5$ s, with the best-fit values of $\tau = 169(14), 15(1)$, and $20(1)$ s for atoms in $F = 1$, $F = 2$, and $F = 1$ with the application of the dynamical decoupling sequence (DD), respectively.

trap. Sub-Doppler cooling of the atoms is performed by increasing the cooling light detuning and decreasing the power of repumper light for ~ 12 ms.

After the lattice loading, $\sim 10^7$ atoms are trapped in the lattice. The cloud has longitudinal and transverse waists $(1/e^2)$ of 260 μm and 70 μm, respectively. To avoid collisional losses the atoms are optically pumped into the lower hyperfine state ($F = 1$) right after loading. In the first 5 seconds, the atoms undergo a fast two-body collisional decay. After the fast two-body loss, the atom number decays slowly only due to collisions with the background atoms, giving an ultra-long lifetime of 169 seconds with an exponential fit, as shown in Figure 2.3.3.

The probe Ω_p and control Ω_c laser fields are resonant with the electronic transitions, $|a\rangle \leftrightarrow |c\rangle$ and $|b\rangle \leftrightarrow |c\rangle$ between levels $|a\rangle = |5s_{1/2}, F = 1\rangle$, $|b\rangle = |5s_{1/2}, F = 2\rangle$, and $|c\rangle = |5p_{1/2}, F = 1\rangle$, as shown in the inset to Figure 2.3.1. The two beam waists

are 50 μm and 200 μm, respectively. The group velocity of the probe field is strongly modified by the control field. The dynamics can be described in terms of a coupled light-matter excitation - the dark-state polariton [68]. The coupled excitation is converted into a pure excitation of the long-lived $|a\rangle - |b\rangle$ atomic coherence when the control field is adiabatically switched off. To eliminate decoherence due to inhomogeneous magnetic fields, the $(m_{F=1}, m_{F=2}) = (0,0)$ ground-state atomic hyperfine coherence is used for storage. This so-called clock transition is magnetically insensitive, so that its energy depends only quadratically on external magnetic fields.

The probe field has a full width at half-maximum (FWHM) of 82 ns and peak power of 130 nW. The control field has a FWHM of 1040 ns and peak power of 160 μW. After a storage period T_s, the control field converts the atomic excitation back into retrieved light field. The latter is coupled to a single-mode fiber and directed onto an avalanche photodiode. Figure 2.3.4 shows the measured pulse areas of the probe, transmitted and retrieved light fields with a storage time of T_s = 1 μs. The ratio of the pulse areas of the retrieved and incident probe field pulses determines the storage efficiency as a function of storage period $\eta(T_s)$. From Figure 2.3.4, we extract $\eta(T_s = 1$ μs$) \approx 0.26$.

When Ω_p approaches single-photon level, minimization of scattering from the control field into the probe mode becomes a priority. A common solution is arranging for the probe and control spatial modes to have a non-zero angle. In our experiment, the probe and control beams propagate in the horizontal plane approximately along the magnetic field direction, intersecting at the center of the atomic sample with a small angle of 1.3°. As a result, the stored atomic excitation forms a spin wave $\propto e^{i\Delta\vec{k}\cdot\vec{r}}$ of period $\Lambda = 2\pi/|\Delta\vec{k}| = 35$ μm, where $\Delta\vec{k} = \vec{k_p} - \vec{k_c}$ is the wave-vector mismatch between the probe and control fields. The thermal motion of atoms smears out the spin wave, limiting the storage lifetime. To minimize motional effects, we employ a one-dimensional optical lattice of 3.2 μm period to confine the atomic motion along the

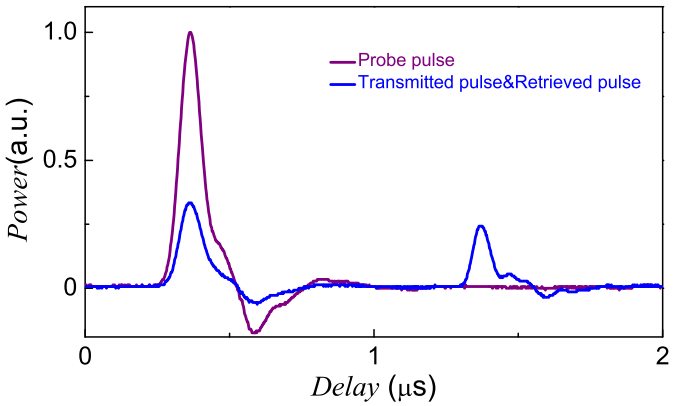

Figure 2.3.4: **Efficiencies.** Temporal profiles of the probe, transmitted, and retrieved pulses.

direction of the spin wave. We attribute a partial decay of retrieval efficiency on the timescale of tens of milliseconds (measured $\eta(T_s = 38\text{ ms}) \approx 0.14$) to spin-wave dephasing from atomic motion along the x- and z- lattice axes, as shown in Figure 2.3.5. The observed 120(5) Hz oscillation frequency should be compared to the calculated trap frequency of 110 Hz in the x- dimension.

2.4 State-insensitive trapping for ground states

2.4.1 Magic magnetic field

To eliminate decoherence due to inhomogeneous magnetic fields, the $(m_{F=1}, m_{F=2}) = (0,0)$ ground-state atomic hyperfine coherence can be used for storage of photons. The so-called clock transition is magnetically insensitive, that is its energy depends only quadratically on external magnetic fields. An unwanted byproduct of optical dipole trapping is that spatially separated atoms will have different transition frequencies due to the spatially varying ac-Stark energy shifts for the two ground levels, as shown in

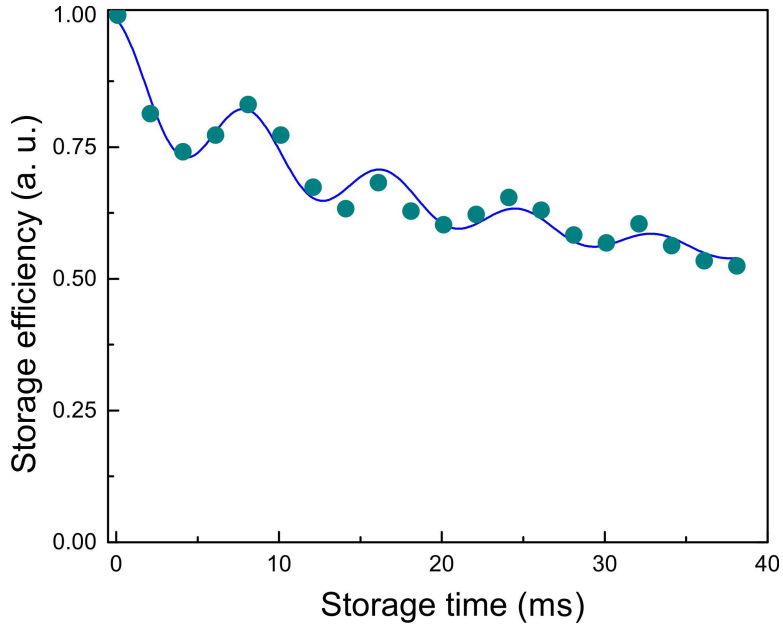

Figure 2.3.5: **Motional dephasing.** Short time temporal dynamics due to motional dephasing and harmonic oscillation in the trap. The fit is a damped oscillation with frequency of 120(5) Hz.

Figure 2.2.1. The differential ac Stark shift results in dephasing of atomic coherences on millisecond timescales [16, 42, 69]. Dephasing that arises from inhomogeneous trapping potentials can be suppressed with two different schemes. In Ref. [41] the light shifts of the clock states were equalized by introducing an additional light field that together with the lattice light was nearly two-photon resonant on a ladder transition. Here, we employ the "magic magnetic field" technique to engineer a state-insensitive optical lattice for the ground states.

For a trapping field with intensity $I(r)$, the scalar part of differential ac-Stark shift can be written as $\frac{1}{2}(\alpha^{(0)}_{F=1} - \alpha^{(0)}_{F=2})I(r)$, where $\alpha^{(0)}_{F=1}$ and $\alpha^{(0)}_{F=2}$ are the scalar polarizabilities of the two ground hyperfine states. If the trapping light is circularly polarized, the vector light shift behaves as an effective magnetic field $B_{eff}(r) = \alpha_{12}I(r)$ pointing along the direction of the trapping light. If we apply a bias magnetic field B along the direction of the B_{eff}, the differential magnetic shifts between the two ground hyperfine states would be $\frac{\mu^2(B+B_{eff}(r)^2)}{\Delta_{hfs}}$. Expanding it we get the term $2\frac{\mu^2 B B_{eff}(r)}{\Delta_{hfs}}$, which

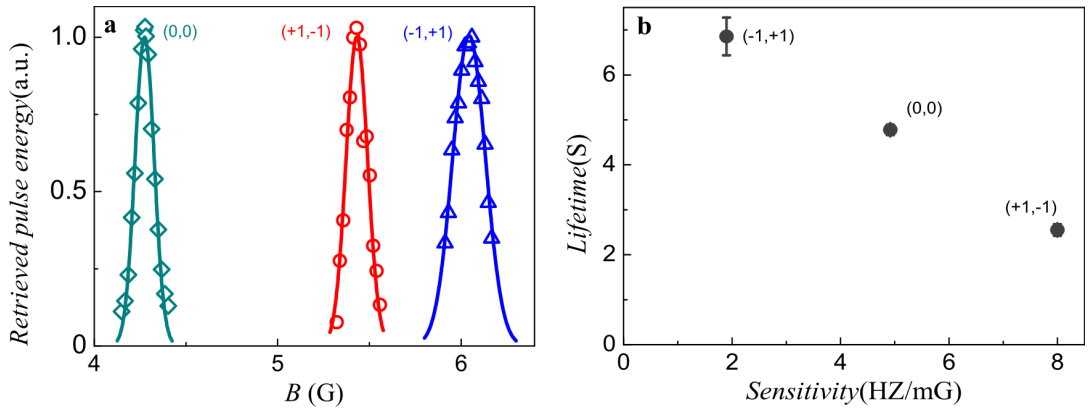

Figure 2.4.1: **Magic magnetic field**. **a,** Retrieved pulse energy E is shown as a function of the magnetic field. The pulse is retrieved after 5, 7, and 2 s for (0,0), (-1,1), and (1,-1) coherences, respectively. The Gaussian fits yield corresponding magic field values $B^{(0)}$ = 4.27, $B^{(-)}$ = 5.43, and $B^{(0)}$ = 6.04 G. **b,** Measured light-storage lifetimes as a function of sensitivity to the magnetic field for three long-lived coherences. Error bars represent uncertainties from the exponential fits.

has the same spatial profile as the scalar light shifts because $B_{eff}(r) = \alpha_1 2I(r)$, while B can be used to tune the amplitude of the vector light shifts for the exact cancellation of the scalar terms. When B is set to the "magic" magnetic field value, the dipole trap is differential ac-stark shifts free, extending the coherence time into the regime of seconds.

2.4.2 Measurement of magic magnetic field values

To determine the "magic" magnetic field value, we measure the retrieved pulse energy as a function of the magnetic field, shown in Figure 2.4.1 (a). We use a Ramsey sequence of two $\pi/2$-pulses to measure the quadratic magnetic shift of the clock transition to calibrate the value of the magnetic field. In addition to the clock coherence, we study storage with two other coherences that are weakly sensitive to magnetic field, $(m_{F=1}, m_{F=2}) = (-1, 1)$ and $(m_{F=1}, m_{F=2}) = (1, -1)$. After loading, a bias magnetic field is applied along the major axis of the trap and atoms are either prepared in the $5S_{1/2}, F = 1, m = 0$ state by means of optical pumping when clock coherence is ad-

dressed, or left unpolarized when $(\pm 1, \mp 1)$ coherences are used. The polarization configurations of the probe and control fields are lin$\perp$lin for clock coherence and $\sigma^{\pm}/\sigma^{\mp}$ for the $(\mp 1, \pm 1)$ coherences.

Gaussian fits of the data in the Figure 2.4.1 give $B^{(0)}$= 4.274(1) G, $B^{(+)}$= 5.431(2) G, and $B^{(-)}$= 6.043(2) G for the three coherences, respectively. After correction by the degree of circular polarization of the two lattice beams $A \equiv \sqrt{1-\varepsilon^2} = 0.990(6)$ [70] and by the geometrical factor $\cos(\theta/2) \approx 0.988$, we obtain the "magic" magnetic field values for the three coherences: $B_0^{(0)}$= 4.18(3) G, $B_0^{(+)}$ = 5.31(3) G, and $B_0^{(+)}$ = 5.91(4) G, respectively. These are in agreement, within the measurement errors, with the values found in Ref. [71]. It should be noted that the latter experiment was performed in a different apparatus, and employed the Larmor precession of the stored spin waves for magnetic field calibration instead of the present microwave clock transition frequency measurement. Both Ref. [71] and the current work are in disagreement with the $B_0^{(0)} \approx$ 4.38 G theoretical prediction from ref. [72] for our 1063.8 nm lattice .

2.4.3 Lifetime and sensitivity of different coherences

The retrieved signal as a function of storage time taken at the "magic field" values for the three coherences is shown in Figure 2.4.2. The observed decay can be ascribed to the spin-wave dephasing caused by the residual magnetic field combined with a weak first-order sensitivity of the used coherences to the magnetic field $\mu' \equiv d\mathscr{E}/dB$. Here $\mathscr{E}$ is the energy of the corresponding hyperfine transition. The geometry of the vacuum set-up was designed to minimize magnetic field gradients across the atomic cloud and was supplemented by magnetic field shielding. The longer 6.9 s lifetime is observed for the (-1,+1) coherence which has the lowest effective magnetic moment μ', whereas the lifetime of 2.5 s is measured for the (+1,-1) coherence with the largest μ', as shown in Figure 2.4.1 (b).

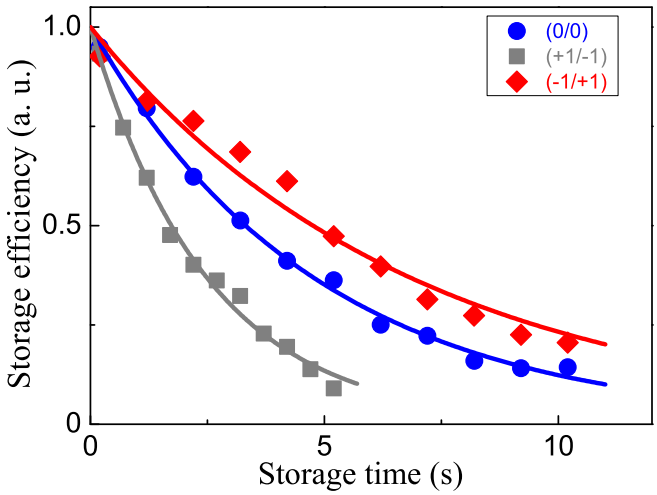

Figure 2.4.2: **Lifetime for three coherences**. Retrieved pulse energy E as a function of storage time, normalized to its value at 38 ms, for the "magic" magnetic field values for the three long-lived coherences, (0,0) (circles), (-1,+1) (diamonds), and (+1,-1) (squares). The storage efficiencies at 38 ms are 0.14, 0.06, and 0.05, respectively, for the three coherences. The solid lines are exponential fits to the data. The extracted $1/e$ lifetimes are 4.8(1), 6.9(4), and 2.5(1) s for the clock, (-1,+1) and (+1,-1) transitions, respectively.

2.5 Dynamical decoupling

2.5.1 Introduction

In an ensemble with inhomogeneous broadening, each atom evolves with its own frequency, accumulating phases at different rates and eventually leading to spin-wave dephasing. However, this type of dephasing process can be reversed by applying the so called refocusing pulses to the ensemble. The simplest refocusing technique is the well know Hahn spin-echo [73], which employs two population inverting π pulses to cancel out the differential phases.

Dynamical decoupling (DD) pulse sequences have been studied in great detail in the context of reducing the decoherence induced by external perturbations on the two

level system [74–80]. Complex pulse schemes like the Carr-Purcell-Meiboom-Gill (CPMG) and Uhrig dynamical decoupling (UDD) sequences have been employed in various systems [78–80] to retrieve the initial quantum state long after the phases coherence would have been destroyed by inhomogeneous broadening. More recently, Sagi. *et al.* [76] have reported that by utilizing more than 200 π-pulses for dynamical decoupling, the coherence time of Rb atoms in a dipole trap can be increased by a factor of 20.

In our system, the spatial inhomogeneity caused by differential ac-Stark shifts is well compensated by setting the magnetic field at the "magic value". However, the peaks for magic conditions shown in Figure 2.4.1 are broadened out by the non-zero magnetic field gradient from the background, limiting the coherence time to be a few seconds. To overcome this decoherence caused by inhomogeneous Zeeman shifts, we apply the Carr-Purcell-Meiboom-Gill decoupling sequence [81] consisting of a train of resonant population-inverting microwave π-pulses on the clock transition. This work represents the first application of DD to light storage in cold atoms system.

2.5.2 Setup for generating Carr-Purcell-Meiboom-Gill sequence

To realize an effective CPMG sequence, it's critical to have precise control over the timing, phase, and amplitude of the pulses. The 6.8 GHz field for DD is generated by frequency mixing a 6.7 GHz output of a signal generator with a 100 MHz output of a field-programmable gate array (FPGA) board-based direct digital synthesizer (DDS), which allows for fast and precise digital control of microwave field phase. The DD pulse frequency is set to be on resonant with the clock states transition by seeding the clock input (CLK) of the DDS with 22-MHz signal from a rf generator. The phase of the 6.8 GHz field can be changed by modulating the phase of the 100 MHz signal from the DDS, which is in turn digitally controlled by a spincore pulse generator. In

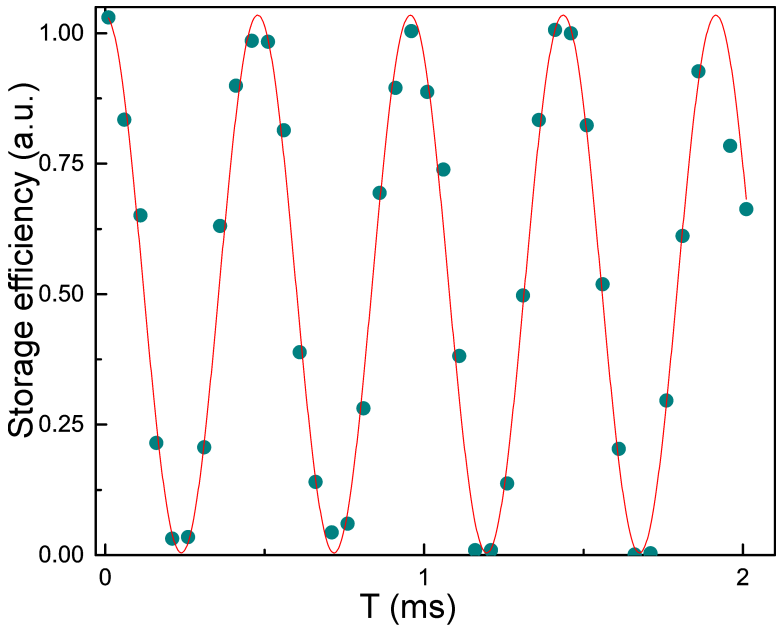

Figure 2.5.1: **Rabi oscillation between clock states.** 6.8-GHz microwave field resonant with the clock transition is applied to ensemble after light storage. Normalized light storage efficiency is shown as a function of duration T of the microwave field. The solid curve is a sinusoidal fit.

the experiment, the phases between the adjacent microwave fields are alternated by 180° to reduce the influence of pulse imperfections. The 6.8-GHz signal is chopped by an rf switch, amplified by a rf amplifier and sent to the rf antenna. To obtain the desired CPMG pulse sequence, TTL pulse signals with programmable pulse duration and separation from the spincore pulse generator are sent to the rf switch.

To monitor the frequency of the 6.8-GHz singal, a directional coupler is inserted before the rf switch and its -16 db output is sent to a microwave frequency counter for precise frequency monitoring. Frequencies of all the rf generators are locked to a Rb atomic frequency standard.

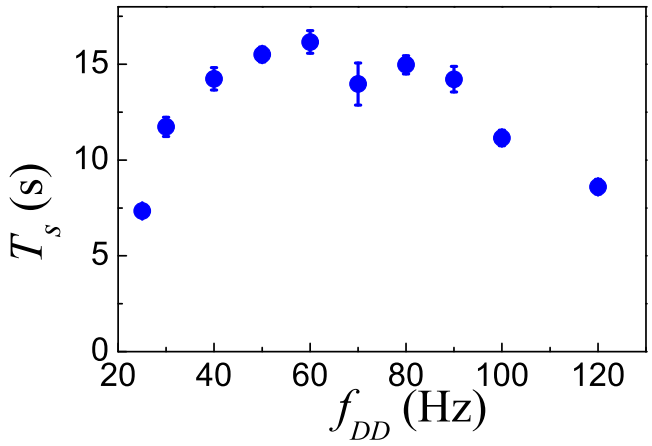

Figure 2.5.2: **Lifetime as a function of the applied DD sequence frequency.** The longest lifetime of 16 s is observed for f_{DD} = 60 Hz. Higher f_{DD} results in lower lifetimes attributed to the accumulation of rotation errors.

2.5.3 Memory lifetimes with dynamical decoupling sequence

The 6834693113 Hz frequency microwave field is calibrated to be resonant with the clock transition by a Ramsey sequence of two $\pi/2$-pulses. The same protocol is used for magnetic field calibration by measurements of the quadratic magnetic field shift of the clock transition frequency. π-pulses for DD are sent to the sample 2.5 ms after the storage of photons to prevent the spin-wave from dephasing. The DD pulses have a duration of 240 μs and are evenly spaced with a programmable frequency $1/f_{DD}$. To calibrate the duration of the π-pulse, we use the microwave field to drive a rabi oscillation between the clock states, see Figure 2.5.1. From Figure 2.5.1, we extract a π-pulse duration of 240 μs.

The DD sequence suppresses decoherence that is slow compared to the decoupling frequency $f_{DD} = 1/T_{DD}$, where $T_{DD}/2$ is the time interval between two consecutive pulses. For perfect 180° rotations, the lifetime is generally expected to increase with f_{DD} [75,76]. The measured values of extended lifetimes are shown in Figure 2.5.2. The

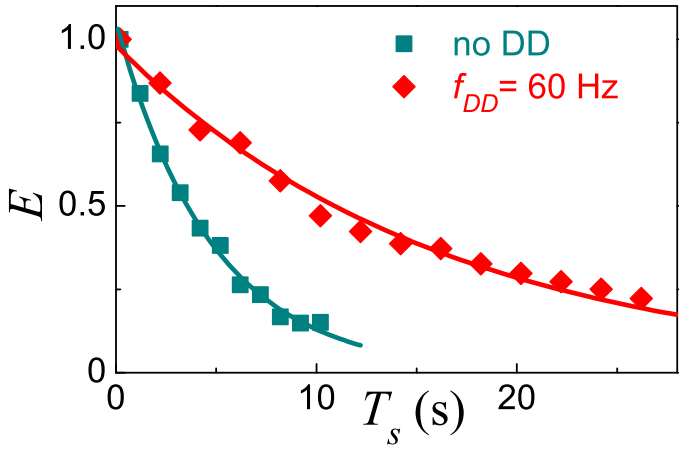

Figure 2.5.3: **Lifetime with and without DD sequence.** Retrieved pulse energy E as a function of storage time, normalized its value at 38 ms, with (diamonds) and without (squares) DD sequence applied. The solid curves are exponential fits.

maximum $1/e$ lifetime of 16 s is measured for f_{DD} = 60 Hz, as shown Figure 2.5.3. Retrieval efficiency $\eta(T_s = 38\text{ ms}) \approx 0.14$ is not affected by the DD pulse sequence for the used range of f_{DD}, but shorter lifetimes are observed for a higher f_{DD}, as shown in Figure 2.5.2. This is attributed to the accumulation of rotation errors with an increased number of pulses. Atom loss also limits the maximum observed lifetime: with a DD sequence applied the atoms effectively spend half of the time in the relatively short-lived $|5s_{1/2}, F = 2, m_F = 0\rangle$ state. The measured lifetime of the atoms in the trap when the DD sequence is applied of 20 s, Figure 2.3.3, provides an upper limit on storage lifetime.

In conclusion, by using atoms confined in a one-dimensional optical lattice with an ultra-long trap lifetime and "magic" magnetic field to compensate the differential stark shift and employing dynamical decoupling sequence, we achieved storage of coherent states of light with lifetime of 16 seconds.

CHAPTER III

Many-body Rabi oscillations with Rydberg blockade

This chapter is based on Ref. [17].

3.1 Introduction

A two-level quantum system coherently driven by a resonant electromagnetic field oscillates sinusoidally between the two levels at frequency Ω [82, 83]. In dilute gases, the inhomogeneous distributions of both the coupling strength to the field and the interactions between individual atoms reduce the visibility of these so-called Rabi oscillations and may even suppress them completely. However, in the limit where only a single excitation is present, a collective, many-body Rabi oscillation at a frequency $\sqrt{N}\Omega$ arises that involves all $N \gg 1$ atoms, even in inhomogeneous systems [84, 85]. When one of the two levels is a strongly interacting Rydberg level, many-body Rabi oscillations emerge as a consequence of a phenomenon known as Rydberg excitation blockade [50]. Here we report initial observations of coherent many-body Rabi oscillations between the ground level and a Rydberg level using several hundred cold rubidium atoms, with a 0.67(10) preparation efficiency of the singly-excited many-body state. The strongly pronounced oscillations indicate a nearly complete excitation blockade of the entire mesoscopic ensemble by a single excited atom. The results pave the way towards quantum computation and simulation using ensembles of atoms.

3.1.1 Strongly interacting Rydberg atoms

Rydberg atoms are atoms with their valence electron (electrons) occupying very high principal quantum number n. For alkali atoms, for example Rubidium used for our experiments, the Rydberg atom has a highly excited outer electron that is far away from the nucleus and thus behaves much like the electron of a hydrogen atom. The size of Rydberg atoms scales as n^2. For atom in $n \geq 100$, its size is ≥ 1 μm. The binding energy for Rydberg state $|n,l,j\rangle$ is

$$E = -R/n^{*2} \tag{3.1.1}$$

where R is the Rydberg constant and the effective principle quantum number $n^* = n - \delta(n,l,j)$. The quantum defect $\delta(n,l,j)$ can be calculated using the Rydberg-Ritz expansion:

$$\delta(n,l,j) = \delta_0(l,j) + \frac{\delta_2(l,j)}{(n-\delta_0(l,j))^2} + \frac{\delta_4(l,j)}{(n-\delta_0(l,j))^4} + \ldots \tag{3.1.2}$$

The values for $\delta_0(l,j), \delta_2(l,j), \ldots$ can be found in Ref. [86–88].

Because of their large and loosely bound outer electron, Rydberg atoms have many exaggerated properties, such as long radiative decay lifetimes, closely spaced levels, giant electric dipole moment, and, as a result, the extreme sensitivity to electric field and strong interactions between two nearby atoms coupled to high-lying Rydberg levels. Table 3.1 gives the scaling of some important properties as the principal quantum number n [51].

The large dipole moments ($\sim n^2$) and small energy difference ($\sim n^{-3}$) between high-lying Rydberg states lead to strong inter-atomic interactions. The interaction energy for two dipoles ($\boldsymbol{\mu}_1$ and $\boldsymbol{\mu}_2$) separated by $\mathbf{R}$ is:

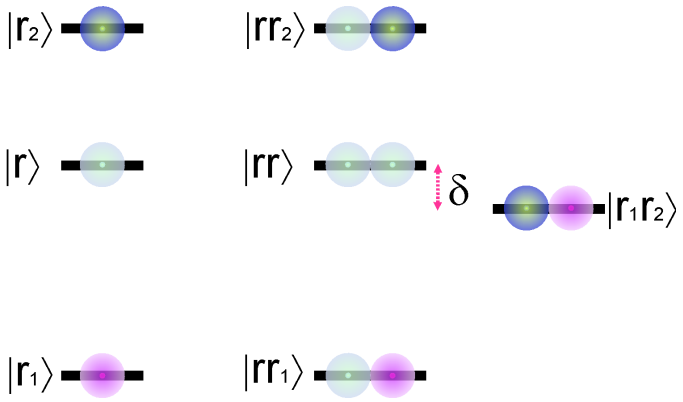

Figure 3.1.1: **Energy levels of single and pairs of Rydberg atoms.** The small energy difference between high-lying Rydberg states leads to the coupling of atomic pair states by the dipole interactions.

$$V_{dd}(\mathbf{R}) = \frac{\boldsymbol{\mu}_1 \cdot \boldsymbol{\mu}_2 - 3\boldsymbol{\mu}_1 \cdot \hat{\mathbf{R}}\hat{\mathbf{R}} \cdot \boldsymbol{\mu}_2}{R^3}. \tag{3.1.3}$$

When two atoms are promoted to Rydberg level $|r\rangle$, $V_{dd}(\mathbf{R})$ couples the pair state $|rr\rangle$ to state $|r_1 r_2\rangle$ with an energy defect of $\delta = E_{r_1} + E_{r_2} - 2E_r$, see Figure 3.1.1. To derive the dipole-dipole interaction induced energy shift on pair state $|rr\rangle$, we write the Hamiltonian for V_{dd} in the basis of $|rr\rangle$, $|r_1 r_2\rangle$:

$$H = \begin{pmatrix} 0 & V_{dd} \\ V_{dd} & \delta \end{pmatrix}.$$

The energy shifts for $|rr\rangle$ is the eigenvalue:

$$\Delta = \delta/2 - sgn(\delta)\sqrt{(\delta/2)^2 + {V_{dd}}^2}. \tag{3.1.4}$$

We can define a critical distance R_c at which $\delta = V_{dd}$. For atoms separated by small distance $R \ll R_c$, we have $V_{dd} \gg \delta$. In this regime, the dipole-dipole interaction is dominant: $\Delta \sim V_{dd} = -sgn(\delta)C_3/R^3$, where the coefficient for dipole-dipole interaction $C_3 \propto \mu_r^{r_1}\mu_r^{r_2}$. The dipole moments $\mu_r^{r_1}, \mu_r^{r_2} \propto n^2$, as a result the dipole-dipole

Table 3.1: Scaling properties of the Rydberg states

Property	n dependence
Radius	n^2
Binding energy	n^{-2}
Energy between adjacent n	n^{-3}
Hyperfine splitting	n^{-3}
Dipole moment $\langle 5p\|r\|ns\rangle$	$n^{-3/2}$
Polarisability	n^7
Radiative lifetime	n^3
Dipole-dipole interaction strength	n^4
Van der Waals interaction strength	n^{11}

interaction strength scales as n^4.

For atom pairs separated by large distance $R \gg R_c, V_{dd} \ll \delta$. As a result, the energy shift is in the van der Waals form: $\Delta \sim |V_{dd}|^2/\delta = C_6/R^6$. Since the energy defect δ scales as n^{-3} and $C_3 \propto n^4$, the van der Waals interaction strength $C_6 = {C_3}^2/\delta \propto n^{11}$. The sign of Rydberg-Rydberg interaction is decided by the sign of the energy defect δ. $\delta > 0$ and $\delta < 0$ result in attractive and repulsive interactions, respectively.

3.1.2 Rydberg blockade and many-body Rabi oscillations

A two-level quantum system coherently driven by a quasi-resonant electromagnetic field is one of the centerpieces of modern quantum physics. Notably, Rabi oscillations in isolated single atoms or dilute gases form the basis for metrological applications such as atomic clocks and precision measurements of physical constants [89]. A wide array of two-level systems have been realized, with atoms, molecules, nuclei, and Josephson junctions being some of the prominent settings. More than half a century ago Dicke recognized that an atomic ensemble coupled to an electromagnetic field cannot always be treated as a collection of independent atoms [84]. His ground-breaking work gave rise to a rich field of collective atom-field interaction physics [90].

A key prediction of Dicke's theory is that under certain conditions atom-field coupling is enhanced by a factor $\sim \sqrt{N}$ when compared to one atom. Collectively-enhanced atom-field coupling has since been observed in a variety of settings involving either the emission or absorption of radiation. A coherent multi-atom Rabi oscillation at a frequency $\sqrt{N}\Omega$ is a particularly dramatic manifestation of quantum mechanics at work on mesoscopic scales, where an entire ensemble exhibits the dynamical behavior of a single two-level system. In 2001, Lukin *et al.* proposed to realize many-body Rabi oscillations in ensembles of atoms driven by a laser tuned to a Rydberg level, and outlined designs for scalable quantum gates for quantum computation and simulation and generation of entangled collective states for metrology beyond the standard quantum limit [50].

When an atom is promoted into a Rydberg level with principal quantum number n, the valence electron is in an orbit that is $\sim n^2$ larger than that of the ground-level atom. The atomic dipole moment is correspondingly larger, so that the interaction of two atoms is increased by $\sim n^4$ in the dipole-dipole regime and by $\sim n^{11}$ in the van der Waals regime [51]. For $n \simeq 100$ the interactions are sufficiently strong that for two atoms separated by a distance $\sim 10\ \mu$m the associated energy shift may prevent the second atom from being excited. This excitation blockade mechanism gives rise to an oscillation between the collective ground state $|G\rangle \equiv \prod_{i=1}^{N} |g\rangle_i$ and the state $|R\rangle \equiv 1/\sqrt{N}\sum_{i=1}^{N} |g\rangle_1 ... |r\rangle_i ... |g\rangle_N$ in which one of the N atoms is in the Rydberg level $|r\rangle$, with frequency $\sqrt{N}\Omega$ [49, 50, 90–92]. The average number $\langle N\rangle_r$ of atoms in level $|r\rangle$ is given by:

$$\langle N\rangle_r = \sin^2(\sqrt{N}\Omega t/2). \tag{3.1.5}$$

This result holds for an inhomogeneous distribution of atom-light coupling Ω_i with the modification $\sqrt{N}\Omega \to \sqrt{\sum_{i=1}^{N} \Omega_i^2}$ and $|R\rangle \to (1/\sqrt{\sum_{i=1}^{N} \Omega_i^2}) \sum_{i=1}^{N} \Omega_i |g\rangle_1 ... |r\rangle_i ... |g\rangle_N$. For two atoms, Rydberg blockade [52] and the accompanying $\sqrt{2}$ enhancement of the

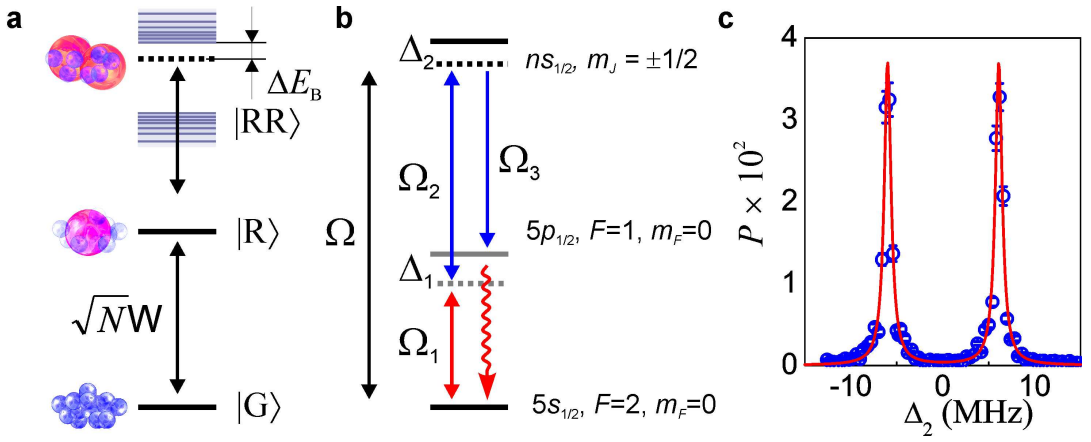

Figure 3.2.1: **Illustration of the excitation blockade of more than one Rydberg atom in the ensemble.** Driving by coherent laser light fields couples the collective ground state $|G\rangle$ to the state with one Rydberg atom $|R\rangle$ with Rabi frequency $\sqrt{N}\Omega$. The doubly excited states $|RR\rangle$ are shifted in energy out of laser resonance by strong atomic interactions. **b,** Single-atom energy levels for ^{87}Rb. Electronic, hyperfine, and Zeeman quantum numbers are shown. The detuning from the intermediate $|5p_{1/2}\rangle$ level is $\Delta_1 = -40$ MHz. **c,** Probability P of photoelectric detection event per trial as a function of two-photon detuning Δ_2 for level $|102s_{1/2}\rangle$. The two $m_j = \pm 1/2$ Zeeman components are split by the bias magnetic field. The solid curve is a sum of two Lorentzian functions. The 0.9 MHz widths (FWHM) of the peaks are determined by the 1 μs excitation duration.

Rabi oscillation frequency [53] have been observed. Over the past decade significant progress has been made in studying many-atom Rydberg blockade [49, 93–100], however, neither blockade by a single atom nor the many-body Rabi oscillations have been achieved.

3.2 Experimental setup and protocol

3.2.1 Sample preparation

To achieve Rydberg blockade over the entire ensemble, it is critical to have a small atomic sample with size $\sim R_0$, where R_0 is the blockade radius. Since we are detecting the Rydberg atoms by converting the Rydberg spin wave into collectively emitted pho-

tons, it's also important to have an optically dense sample to obtain high atom-light conversion efficiency. To fulfill these requirements, we prepare a gas of ^{87}Rb atoms of temperature $T \simeq 10\ \mu$K and of peak density $\rho_0 \simeq 10^{12}$ cm^{-3} in a one-dimensional optical lattice, as shown in Figure 3.2.2.

Sample preparation starts with the 70 ms-long loading of a magneto-optical trap of ^{87}Rb from background vapor. During the following 25 ms, the detuning of cooling light is increased, the repumper intensity is decreased, and the optical lattice is turned on. The lattice is composed of a single 782 nm retro-reflected linearly polarized Gaussian beam. Untrapped atoms are allowed to fall away from the experimental region during the next 15 ms period, and a $B_0 = 4.3$ G bias magnetic field is turned on. The trapped atoms are optically pumped to the $|5s_{1/2}, F = 2, m_F = 0\rangle$ state. The optical lattice is switched off by an acousto-optical modulator (AOM), and a 3 μs long sequence of two-photon Rabi driving and retrieval is repeated for 50 μs, with a 1 μs optical pumping period included every five cycles. The overall repetition rate of the experiment is ≈ 8 Hz. To measure the many-body rabi oscillations with different number of atoms, the peak density ρ_0 was controlled by varying the time period between lattice loading and the two-photon excitation sequence between 15 and 90 ms.

3.2.2 Narrow linewidth lasers for Rydberg excitation

To enter the regime of Rydberg excitation blockade and observe many-body Rabi oscillations, the blockade shift ΔE_B between a pair of atoms at the ends of the ensemble must be greater than the spectral width $\delta\omega$ of the exciting laser field. For this work, we have built new 795 nm and 948 nm lasers and lock them to a high finesse Fabry-Perot cavity, obtaining linewidth of ~ 60 KHz.

A home-made extended cavity diode laser (ECDL) is used to generate light at 948 nm. Part of the 948 nm light is sent to the cavity for narrow linewidth laser

Table 3.2: **Frequencies of the 474 nm light for the $|5p_{1/2}, F = 2\rangle \leftrightarrow |r\rangle$ transition**.

Rydberg level $\|r\rangle$	frequency of 474 nm light	frequency of 948 nm light
81 $s_{1/2}$	632374.22 GHz	316187.1 GHz
90 $s_{1/2}$	632480.82 GHz	316240.4 GHz
100 $d_{3/2}$	632578.74 GHz	316289.4 GHz
102 $s_{1/2}$	632580.22 GHz	316290.1 GHz

locking. A tapered amplifier is seeded by the 948 nm light and outputs $\sim$ 1.2 W of light. The output of the TA is then frequency doubled by an optical frequency doubler (Spectra-Physics WaveTrain), with a total output power of $\sim$ 120 mW at 474 nm. The frequencies of the 474 nm coupling $|5p_{1/2}, F = 1\rangle$ state to Rydberg s or d states are calculated using quantum defect values of Ref. [86]. Initial coarse tuning of the laser is done by monitoring the 948 nm laser frequency with a wave-meter. Table 3.2 summarizes the 474 nm laser frequencies for the $|5p_{1/2}, F = 2\rangle \leftrightarrow |r\rangle$ transitions used in this Chapter and the frequencies of 948 nm light for wave-meter.

The 795 nm field is produced by an ECDL. Light at 474 nm is generated by frequency-doubling the output of a tapered amplifier driven by a 950 nm ECDL laser. Both lasers are frequency-locked to a thermally stabilized ultra-low expansion glass cavity. The transition is located by scanning the laser frequency across a resonance and measuring the photoelectric detection probability for the retrieved field. The 795 nm and 474 nm excitation fields are tuned to the two-photon resonance between the ground-level component $|5s_{1/2}, F = 2, m_F = 0\rangle$ and a Zeeman component of the Rydberg level $|ns_{1/2}, m_j = -1/2\rangle$.

3.2.3 Excitation and detection protocol

In Ref. [37], the atoms were excited with laser fields of two-photon linewidth $\delta\omega \approx 5$ MHz (comparable to ΔE_B) while relying on the dephasing of multiply-excited spin waves [101–103] to generate high-quality single photons. To realize the excitation

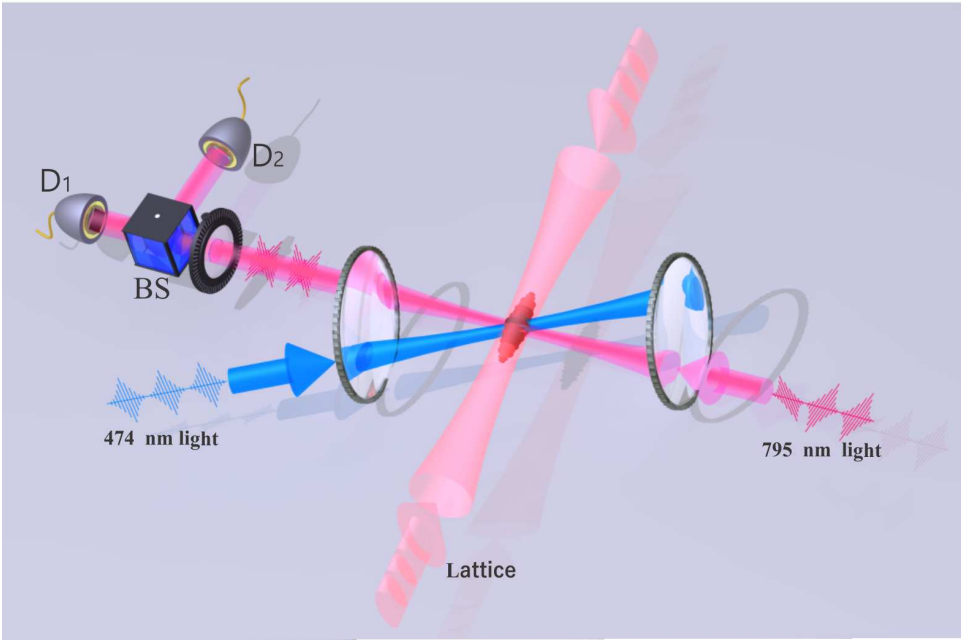

Figure 3.2.2: **Overview of the experiment.** A small and dense sample of cold ^{87}Rb is prepared in a 1D lattice formed by retro-reflection of a single 782 nm laser field. The Rydberg excitation is performed by the 795 nm and 474 nm light fields. The Rydberg spin-wave is converted into a propagating photon field by a 474 nm read-out field. The retrieved light field is split at a BS and detected by single photon detectors D_1 and D_2 for the measurement of second-order intensity correlations.

blockade regime, we lowered the laser linewidths to < 100 kHz and employed a longer (1 μs instead of 0.2 μs) excitation pulse. We reduced the impact of decreasing atomic density due to ballistic expansion of the cloud, and the concomitant smearing of the oscillations, by using a shorter, 50 μs instead of 200 μs, sequence of trials for each lattice loading.

For Rydberg excitation, the lattice is shut off and the atoms are driven in resonance between the ground $|g\rangle = |5s_{1/2}\rangle$ and a Rydberg $|r\rangle$ level with the two-photon Rabi frequency $\Omega(\mathbf{r}) = \Omega_1(\mathbf{r})\Omega_2(\mathbf{r})/(2\Delta_1)$ for a duration $\tau = 1$ μs, with the corresponding single-atom excitation pulse area $\theta \equiv \Omega(0)\tau$, as shown in Figure 3.2.1 (a) and (b). The transverse size (Gaussian waists $w_x \approx w_y \simeq 6$ μm) of the Rydberg excitation region is determined by the overlap of the nearly counter-propagating two-photon excitation

laser fields Ω_1 at 795 nm and Ω_2 at 474 nm, as shown in Figure 3.2.2. The longitudinal extent of the ensemble is determined by the sample size of waist $w_z \approx 11$ μm along z. Both Ω_1 (at 795 nm) and Ω_2 (at 474 nm) fields are linearly polarized along the same axis.

The single-photon Rabi frequency on the blue transition is

$$\Omega_2 = -e\mathscr{E}\langle 5p_{1/2}, F = 1, m_F = 0|r|ns_{1/2}, m_j\rangle, \tag{3.2.1}$$

where $\mathscr{E}$ is electric field amplitude. The radial matrix element is reduced using the Wigner-Eckart theorem. The angular part is calculated following Ref. [104], while the reduced matrix element is approximated by $\langle r\rangle = 0.14 \times (50/n)^{3/2} a_0$ [49]. Since Ω_2 and Ω_3 fields are propagating in the same spatial mode, the retrieved field is phase matched into the mode of the Ω_1 field and coupled into a single mode 50/50 fiber beam-splitter followed by a pair of single-photon detectors D_1 and D_2. A gating AOM at the fiber beam-splitter input port is employed to avoid damaging the single photon detectors by the Ω_1 field.

For every experimental trial, photoelectric events on detectors D_1 and D_2 are recorded within a time interval determined by the length of the retrieved pulse ($\sim$ 500 ns). Photoelectric detection probabilities for both detectors are calculated as $p_{1,2} = N_{1,2}/N_0$, where $N_{1,2}$ are numbers of recorded events, and N_0 is the number of received triggers. For the storage and retrieval protocol $p_{1,2} \sim \eta_s \eta_r \eta_{t\&d} n$, where n is the number of photons in the incident Ω_1 field. We can therefore extract the retrieval efficiency of state $|R\rangle$ into a single photon η_r from $\eta_s\eta_r$ via the retrieved signal measurements, and the storage efficiency η_s via the measurements of the transmitted fraction of Ω_1. Using $|r\rangle = |81s_{1/2}\rangle$, we obtain $\eta_s = 0.0098(14)$ and $\eta_s\eta_r = 0.00222(7)$, resulting in $\eta_r = 0.23(3)$. A higher value of the Rabi frequency $\Omega_2(0) = 5.7$ MHz is employed in these measurements. Transmission through the glass vacuum chamber is 0.92, the

gating AOM diffraction efficiency is 0.7, the fiber coupling efficiency is 0.73, and the quantum efficiency of the single-photon counters is 0.55, for a combined light transmission and detection efficiency $\eta_{td} = 0.26$. The photoelectric detection probability for double coincidences is calculated as N_{12}/N, where N_{12} is a total number of simultaneous clicks on both detectors for a given experimental trial. The second order intensity correlation function at zero delay is given by $g^2(0) = p_{12}/(p_1 p_2)$.

3.3 Observation of coherent many-body Rabi oscillations

Here we report observations of many-body Rabi oscillations for a mesoscopic ($a \simeq 15$ μm) ensemble of rubidium atoms in the regime of Rydberg excitation blockade by just one atom. To achieve this, the interaction strength $\Delta E_B \equiv \Delta_{ij}(a)$ between a pair of atoms at a distance equal to the ensemble size a must be greater than the spectral width $\delta\omega$ of the exciting laser field. For the purpose of single photon generation, interaction induced dephasing of multiply-excited spin waves [101–103] can be employed. In Ref. [37], single photons were generated with the Rydberg excitation using laser fields of two-photon linewidth $\delta\omega \approx 5$ MHz. To realize the excitation blockade regime, we narrow the laser linewidths to < 100 kHz and employ a longer (1 μs instead of 0.2 μs) excitation pulse. The duration of coherent atom-light interaction is limited by the finite coherence time of the ground-Rydberg transition caused by atomic motion [37]. We also reduce the impact of decreasing atomic density due to ballistic expansion of the cloud, and the concomitant smearing of the oscillations, by using a shorter, 50 μs instead of 200 μs, sequence of trials for each lattice loading.

3.3.1 Many-body Rabi oscillations and $\sqrt{N}$ dependence

We measure the population of state $|r\rangle$ by quantum state transfer onto a retrieved light field using a 1 μs long read-out field Ω_3 at 474 nm, in resonance with the $|102s_{1/2}\rangle \leftrightarrow |5p_{1/2}\rangle$ transition [35, 38]. The retrieved field is coupled into a single-mode fiber followed by a beam splitter and a pair of single-photon detectors D_1 and D_2. Figure 3.3.1 (a) shows the sum of the photoelectric detection event probabilities at the two detectors $P \equiv p_1 + p_2$ as a function of the single-atom Rabi angle θ, varied by changing $\Omega_1(0)$ between 0 and 5.5 MHz for a fixed $\Omega_2(0) = 3.3$ MHz. The data are fit with the sinusoidal oscillation of Eq. 3.1.5 modified by two Gaussians, as described in the section 3.3.2. The choice of the fit function is motivated by a physical picture in which the visibility of the oscillation is smeared by fluctuations of the atom number and the intensities of the laser fields Ω_1 and Ω_2. The overall decay of the retrieved signal is due to an inhomogeneous distribution of light shifts for atoms in state $|R\rangle$, $\sim N_e\Omega(0)^2/\Delta E_B$ which couple the state $|R\rangle$ to other collective singly-excited states $|R'\rangle$, and due to population of doubly-excited states $|RR\rangle$ which are retrieved with substantially suppressed efficiency due to spin-wave dephasing [37, 101, 102]. The effective number of atoms N_e is defined as $N_e \equiv \sum_{i=1}^{N} \Omega_i^2/\Omega^2(0)$.

For our experimental geometry, $\Omega_i^2 = \Omega^2(0)\exp(-2x^2/w_x^2 - 2y^2/w_y^2)$, and the atom density $\rho = \rho_0 \exp(-2z^2/w_z^2)$. Therefore, $N_e = (\pi/2)^{3/2} w_x w_y w_z \rho_0$. The efficiency η_p to prepare state $|R\rangle$ is obtained by normalizing the probability of a photoelectric detection event per trial $P(\theta \approx \pi/\sqrt{N_e}) \simeq 0.04$ by the retrieval efficiency of state $|R\rangle$ into a single photon $\eta_r = 0.23(3)$ and the transmission and detection efficiency $\eta_{td} = 0.26$. At the first oscillation maximum ($\theta = \pi/\sqrt{N_e}$), we obtain $\eta_p = 0.67(10)$. The uncertainty is largely due to the value of η_r measured with the $|81s_{1/2}\rangle$ Rydberg level. η_r maybe be somewhat lower for the $|102s_{1/2}\rangle$ level due to longer retrieved fields and correspondingly larger motional dephasing [37]. Our Monte-Carlo simulations of the

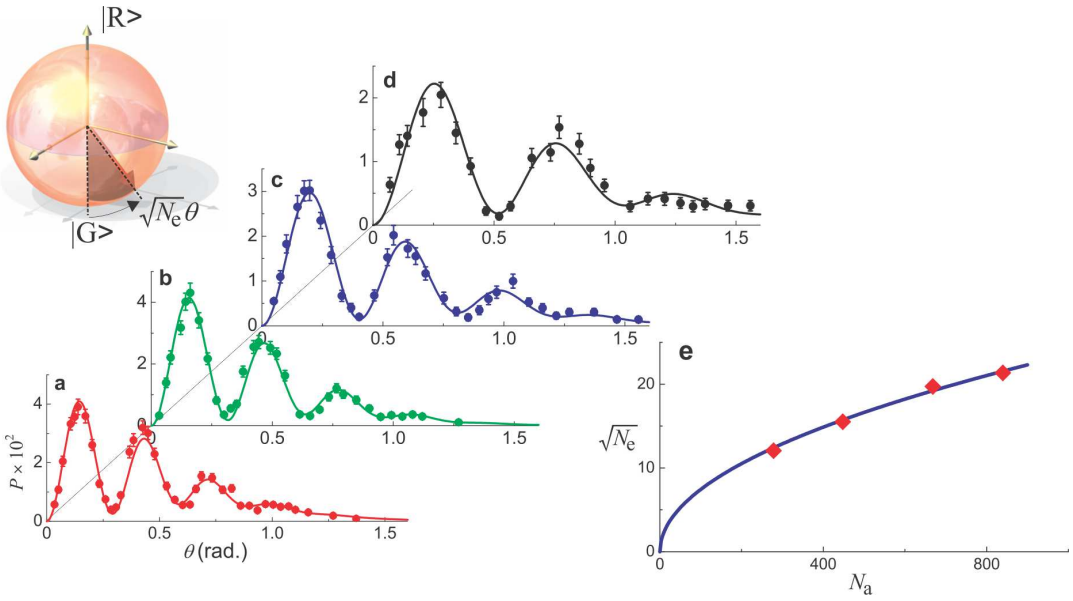

Figure 3.3.1: **Many-body Rabi oscillations and $\sqrt{N}$ dependence.** In panels (a)-(d), probability of photoelectric detection P as a function of the single-atom Rabi angle θ is shown; upper level is $\left|102s_{1/2}\right\rangle$, excitation duration is $\tau = 1$ μs. Solid curves are fits of the form $P = \frac{1}{2}Ae^{-\alpha\theta^2}(1 - e^{-\beta\theta^2}\cos(\sqrt{N_e}\theta))$, see section 3.3.2. The fit parameters (A, α, β, N_e) are: $(4.3, 1.43, 1.70, 456)$ for **a**, $(4.44, 1.43, 1.77, 397)$ for **b**, $(3.24, 1.14, 0.72, 243)$ for **c** and $(2.56, 0.79, 0.86, 148)$ for **d**. (e) $\sqrt{N_e}$ as a function of number of atoms N_a determined from fluorescence measurements. The data are fit with a function $C\sqrt{N_a}$, with the best-fit value $C = 0.74$. The inset shows a collective Bloch vector tipped by the angle $\sqrt{N_e}\theta$ on the unit sphere corresponding to the many-atom states $|G\rangle$ and $|R\rangle$. The error bars represent $\pm$ one standard deviation ($\sqrt{M}$) for M photoelectric counting events.

excitation process that include atomic interactions and motional spin-wave dephasing predict $\eta_p \simeq 0.75$ for $\theta = \pi/\sqrt{N_e}$. We expect measured values of η_p to be closer to unity when Rydberg excitation blockade is stronger, which can be achieved by reducing the size of the ensemble or increasing the lifetime of the ground-Rydberg optical coherence.

To explore the collective character of the observed Rabi oscillations, we measure P as a function of θ while varying the peak density of the sample ρ_0, see Figure 3.3.1 (b-d). Figure 3.3.1 (e) shows the normalized frequency of the Rabi oscillation $\sqrt{N_e}$ extracted from the data in Figure 3.3.1 (a-d) as a function of the number of atoms in the

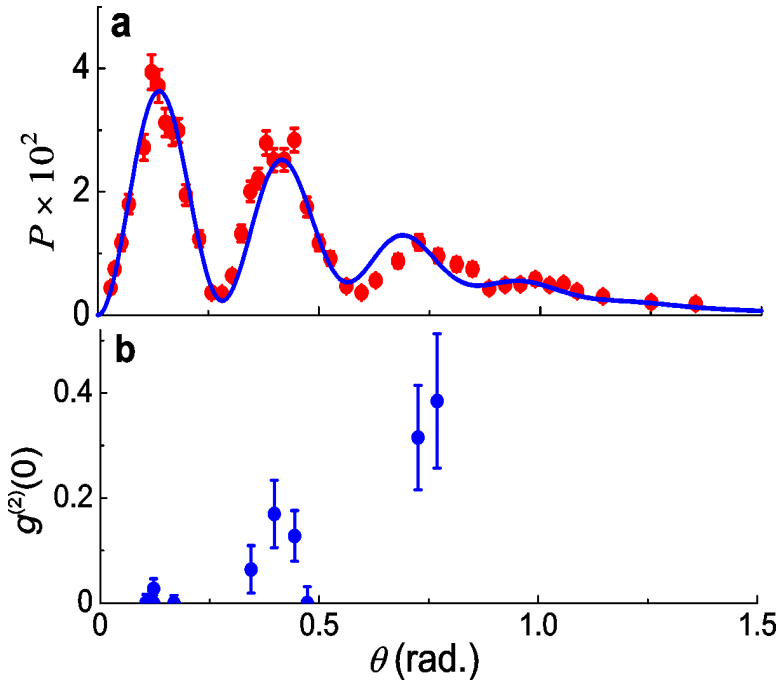

Figure 3.3.2: **Deterministic single photon source based on Rydberg blockade.** Probability of photoelectric detection P and second-order intensity correlation function at zero delay $g^{(2)}(0)$ as a function of the single-atom Rabi angle θ. Excitation duration is $\tau = 1$ μs and upper level is $\left|102s_{1/2}\right\rangle$. In panel **a** the solid curve is a fit as in Figure 3.3.1 (**a-d**). The fit parameters (A, α, β, N_e) are $(3.80, 1.48, 1.86, 492)$. The error bars represent $\pm$ one standard deviation ($\sqrt{M}$) for M photoelectric counting events.

ensemble N_a. The latter is calculated using peak density ρ_0 measured by the hyperfine state-selective fluorescence imaging of the atomic sample with magneto-optical trap cooling beams used without a repumping field to exclude contribution of $|5s_{1/2}, F = 1\rangle$ atoms. The absence of additional peaks in Figure 3.2.1 (c) supports a near-unity value for the fraction of atoms f in the $m = 0$ Zeeman sub-level. Ideally, we expect the effective atom number N_e extracted from the Rabi oscillation period to equal the atom number N_a determined by fluorescence imaging of the sample. The parameter C in the fit in Figure 3.3.1 (e) would equal unity, whereas we extract $C = 0.74$. In addition to the factor $\sqrt{f}$, likely causes for $C < 1$ are alignment imperfections, uncertainties in the determined waists of the two-photon excitation laser beams, and uncertainties in the fluorescence measurements of ρ_0.

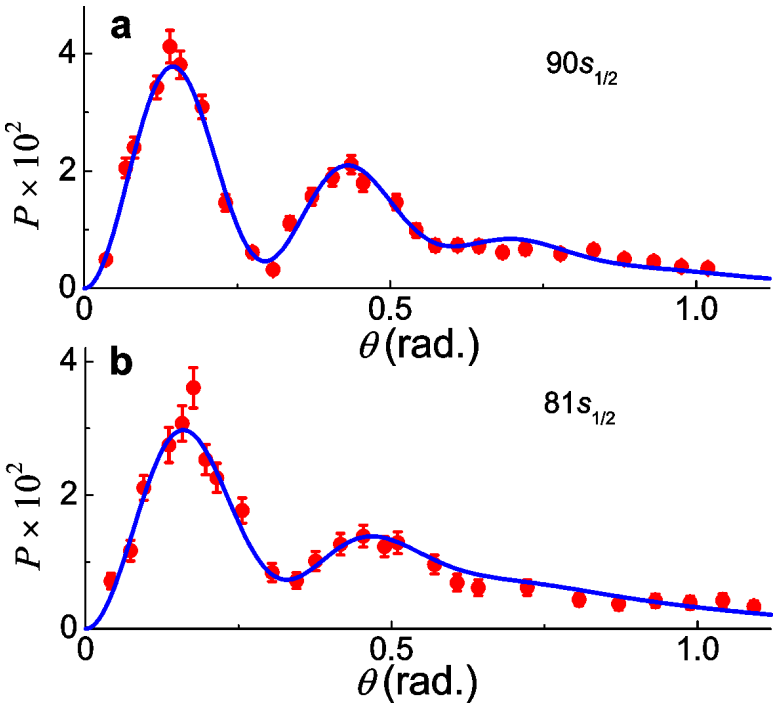

Figure 3.3.3: **Many-body Rabi oscillations for $n = 90$ and $n = 81$.** Excitation duration is $\tau = 1\ \mu$s. The solid curves are fits as in Figure 3.3.1 (**a-d**), where the fit parameters (A, α, β, N_e) are $(4.10, 2.00, 3.52, 441)$ for n=90 in **a** and $(3.42, 1.62, 6.70, 335)$ for n=81 in **b**, respectively. The error bars represent $\pm$ one standard deviation $(\sqrt{M})$ for M photoelectric counting events.

We further confirm that the dynamics seen in Figure 3.3.1 correspond to the oscillation of Eq. 3.1.5 by measurements of the second-order intensity correlation function at zero delay $g^{(2)}(0)$ as a function of θ, shown in Figure 3.3.2. Measured values of $g^{(2)}(0)$ well below unity, together with substantial visibility of the oscillations, indicate that only one Rydberg excitation is present in the entire ensemble of several hundred atoms. The substantial observed values of $g^{(2)}(0) \approx 0.3$ for $\sqrt{N_e}\theta \geq 5\pi$ in Figure 3.3.2 (b) suggest that population of doubly-excited states contributes noticeably to the extracted values of α. Combining all the data points for $\sqrt{N_e}\theta \approx \pi$ in Figure 3.3.2 (b), we obtain $g^{(2)}(0) = 0.006(6)$, which, to our knowledge, is the lowest value for this quantity for any previously reported light source. It is consistent with a lower bound of $g^{(2)}_{bg}(0) = 0.012(2)$ due to background counts, of which about half are due to

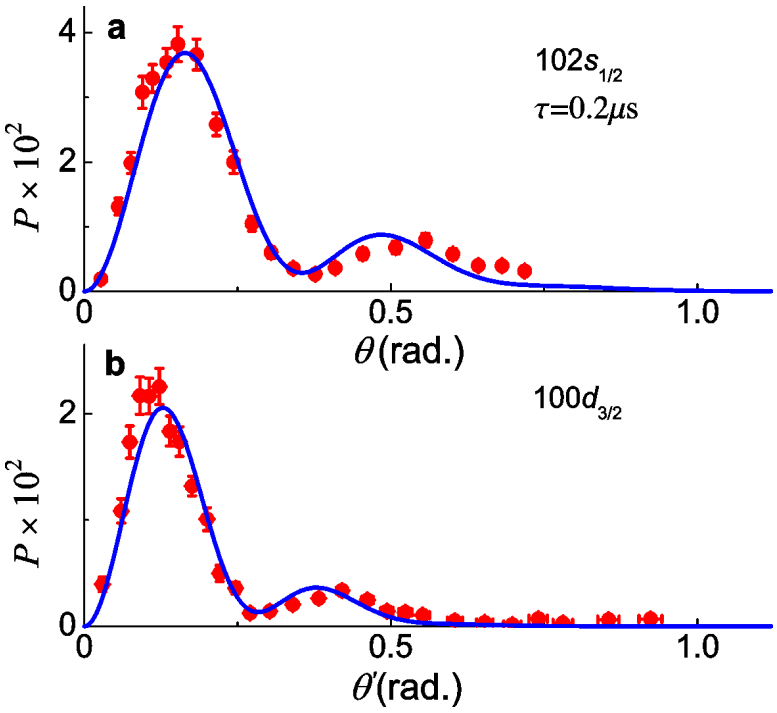

Figure 3.3.4: **Many-body Rabi oscillations with shorter excitation and d state.** Level $|102s_{1/2}\rangle$ is excited for $\tau = 0.2$ μs in **a**, and level $|100d_{3/2}\rangle$ is excited for $\tau = 1$ μs in **b**. The solid curves are fits as in Figure 3.3.1 **(a-d)**, the fit parameters (A, α, β, N_e) are $(4.56, 5.27, 3.86, 340)$ in **a**. For the data in **b**, the laser is tuned to the strongest spectral component, with the scale θ' determined by using the value of $N_e = 492$ from the preceding measurements with the $|102s_{1/2}\rangle$ level, with a fit providing the value of peak single-atom Rabi frequency Ω_0 and the fit parameters (A, α, β) are $(2.58, 10.7, 3.49)$. The vertical error bars represent $\pm$ one standard deviation $(\sqrt{M})$ for M photoelectric counting events. The horizontal error bars in **b** reflect the uncertainty in determination of the x-axis scale θ'.

detector dark counts. Our Monte-Carlo simulations suggest that both excitation blockade [50] and spin-wave dephasing [101] mechanisms contribute to the suppression of two-photon events. In contrast, in our previous study using shorter and wider-linewidth excitation, numerical simulations employing spin-wave dephasing, without excitation blockade, accurately described observed spatial spin-wave correlations [37].

The importance of achieving excitation blockade, $\Delta E_B \gg \delta\omega$, to observe many-body Rabi oscillations is checked by reducing ΔE_B in measurements with $n = 90$ and $n = 81$, as shown in Figure 3.3.3. Figure 3.3.4 (a) shows data with increased $\delta\omega$

by using a shorter $\tau = 0.2$ μs excitation. The oscillation is less pronounced both for smaller ΔE_B, as shown in Figure 3.3.3, and larger $\delta\omega$, see Figure 3.3.4 (a).

Figure 3.3.4 (b) shows a similarly suppressed oscillation in measurements with the $|100d_{3/2}\rangle$ level with a $\tau = 1$ μs excitation. This may be attributed to a blockade breakdown due to a strong angular dependence of the atomic interaction strengths for $|nd\rangle$-levels [49]. The excitation spectrum for $|100d_{3/2}\rangle$ shows a complex structure, likely due to an interplay of an ambient electric field with the bias magnetic field. It should also be noted that for a Gaussian distribution of atom-field couplings, single-atom Rabi oscillations are almost completely washed out [105], which makes the observation of many-atom oscillations under these conditions even more remarkable.

3.3.2 Oscillation visibility and decoherence model

We employ the following Hamiltonian to describe our system:

$$\hat{H} = \sum_{\mu} \hbar(\omega_g \hat{\sigma}_{\mu}^{gg} + \omega_r \hat{\sigma}_{\mu}^{rr}) + \frac{1}{2}\sum_{\mu} \hbar(\Omega_{\mu} e^{-i\omega_L t}\hat{\sigma}_{\mu}^{rg} + h.c.) + \sum_{\mu>\nu} \hbar\Delta_{\mu\nu}\hat{\sigma}_{\mu}^{rr} \otimes \hat{\sigma}_{\nu}^{rr}. \tag{3.3.1}$$

The atomic operators for the atom μ are defined as $\hat{\sigma}_{\mu}^{ab} = |a\rangle_{\mu}\langle b|$, where $a, b \in [g, r]$ with $|g\rangle_{\mu}$ being the atomic ground state and $|r\rangle_{\mu}$ being the addressed Rydberg level. The two-photon excitation is modeled using the effective Rabi frequency $\Omega = \Omega_1\Omega_2/(2\Delta)$. The interaction between Rydberg levels is described with a single-channel model. For $\Delta_{\mu\nu} \gg \Omega_{\mu}, \Omega_{\nu}\ \forall(\mu,\nu)$, the excitation blockade is operational. Adiabatic elimination of double and higher-order excitations from the equations of motion results in an effective Hamiltonian for the singly-excited part of the spectrum:

$$\hat{H}_{eff} = \sum_{j} \hbar\Delta_j |j\rangle\langle j| + \sum_{i>j} \hbar C_{ij}(|i\rangle\langle j| + |j\rangle\langle i|) + \frac{1}{2}\sum_{j} \hbar\Omega_j(|j\rangle\langle G| + |G\rangle\langle j|). \tag{3.3.2}$$

Here $\Delta_j = -\sum_{i\neq j}\Omega_i^2/(4\Delta_{ij})$, $C_{ij} = -\Omega_i\Omega_j/(4\Delta_{ij})$, where $|j\rangle$ is the many-body state with the j-th atom in the Rydberg level. The first two terms of the effective Hamiltonian are due to the light shifts induced by the (detuned) doubly-excited states onto the single excitations.

When the interaction-induced inhomogeneous light shifts are omitted, the Hamiltonian results in an ideal Rabi oscillation between the ground state $|G\rangle$ and the single spin wave $|R\rangle = (1/\sqrt{\sum_j \Omega_j^2})\sum_j \Omega_j|j\rangle$. If at time $t = 0$ the system is in state $|G\rangle$, the state at future times is given by $|\psi(t)\rangle = \cos(\Omega t/2)|G\rangle - i\sin(\Omega t/2)|R\rangle$. When the light shift terms are included, the state $|R\rangle$ is coupled to a broad distribution of singly-excited states and therefore leaks into this quasi-continuum, leading to $P \sim |\langle R|\psi(t)\rangle|^2$ decaying with a rate $\sim N_e\Omega_0^2/\Delta E_B$. The doubly-excited states are expected to be populated at a rate $\sim N_e\Omega_0^2$. Trial-to-trial fluctuations $\Delta\Omega$ and ΔN_e in N_e and Ω_0, respectively, lead to a decay of the oscillation visibility. The probability of photoelectric detection per trial P as a function of θ in Figures 3.3.1-3.3.4 is, therefore, fit by a function:

$$P(\theta) = \frac{1}{2}Ae^{-\alpha\theta^2}(1 - e^{-\beta\theta^2}\cos(\sqrt{N_e}\theta)), \tag{3.3.3}$$

where dimensionless fit parameters $\alpha \sim N_e$ and $\beta \sim (\Delta N_e/2N_e)^2 + (\Delta\Omega/\Omega_0)^2$ describe the roles of the light shifts and population of doubly-excited states, and atom number and intensity fluctuations, respectively, while an amplitude A represents the overall measured retrieval and detection efficiency.

We have demonstrated coherent many-body Rabi oscillations in an ensemble of several hundred cold rubidium atoms. The oscillations provide compelling evidence for the achievement of a collective Rydberg excitation blockade by a single excited atom. Our results pave the way towards quantum computation and simulation using ensembles of atoms [50, 106].

CHAPTER IV

State-insensitive Rydberg trapping

This chapter is based on Ref. [18].

4.1 Introduction

In most of quantum optics experiments involving Rydberg atoms, atomic samples were initially prepared in conservative potentials $U_g(\mathbf{r})$ formed by far-off-resonance optical fields. However, while such potentials are attractive for ground atoms, $U_g(\mathbf{r}) < 0$, they are generally repulsive for Rydberg atoms, $U_r(\mathbf{r}) > 0$ [107], see Figure 4.1.1 (a). Therefore, they have to be switched off in order to maintain coherent character of the Rydberg excitation process, resulting in fast atom loss and a limited degree of quantum state control.

Here we report realization of a state-insensitive optical lattice, with the differential energy shift $\delta U \equiv U_r(\mathbf{r}) - U_g(\mathbf{r})$ between ground and Rydberg states eliminated by tuning the lattice to one of the "magic" wavelengths at 1004 nm or 1012 nm [108]. The matched trapping potentials preserve the ground-Rydberg quantum optical coherence, and allow Rydberg excitation protocols to be repeated tens of thousands of times without significant atom losses. As illustrated in Figure 4.1.1 (b), an ensemble of atoms is confined by a retro-reflected 1-D optical lattice at the magic wavelengths of 1004 nm, which is still a far-off-resonance trap for the ground states. To create the same

Table 4.3: **Magic trapping frequencies.**

transition $\|r\rangle \leftrightarrow \|a\rangle$	trapping light frequency
$\|81s_{1/2}\rangle \leftrightarrow \|6p_{3/2}\rangle$	296198.6 GHz
$\|90s_{1/2}\rangle \leftrightarrow \|6p_{1/2}\rangle$	298628.5 GHz
$\|90s_{1/2}\rangle \leftrightarrow \|6p_{3/2}\rangle$	296305.6 GHz

trapping potentials for Rydberg state $|r\rangle$ and ground state $|g\rangle = |5s_{1/2}\rangle$, the frequency of the lattice laser is tuned to the blue side of the $|r\rangle \leftrightarrow |a\rangle$ transition, where $|r\rangle$ is the Rydberg level and $|a\rangle$ is the $|6p_{1/2}\rangle$ level.

4.2 Experimental methods

The state-insensitive trap used here is an optical lattice formed by a retro-reflected linearly polarized laser field at 1004 nm. Figure 4.2.1 shows the laser system for generating the magic trapping light and the experimental setup. The laser field for the trap is the output of a tapered amplifier (TA) driven by an ECDL, as shown in Figure 4.2.1 (a). Part of the light from the ECDL is sent through an electro-optic modulator (EOM) and then coupled to a reference cavity for laser frequency stabilization. Using the Pound-Drever-Hall (PDH) technique, the ECDL is frequency-locked to the sideband generated by the EOM. The frequency of 1004 nm light in the experiment can be changed by shifting the driving frequency of the EOM. The light from the ECDL is also partially split and sent to a wavemeter for frequency monitoring. The frequencies of the 1004 (1012) nm, coupling $|6p_{1/2,3/2}\rangle$ state to Rydberg s states, are calculated using quantum defect values of Ref. [86]. Initial coarse tuning of the laser is done with the wave-meter. Table 4.3 gives the magic trapping frequencies for different Rydberg and $6p$ levels.

About 1.4 W of light at 1004 nm is generated by the TA. A 80 MHz AOM is placed after the TA for the switching of the dipole trap and the +1 order is coupled into the fiber. An optical isolator is used after the fiber at the experimental setup to

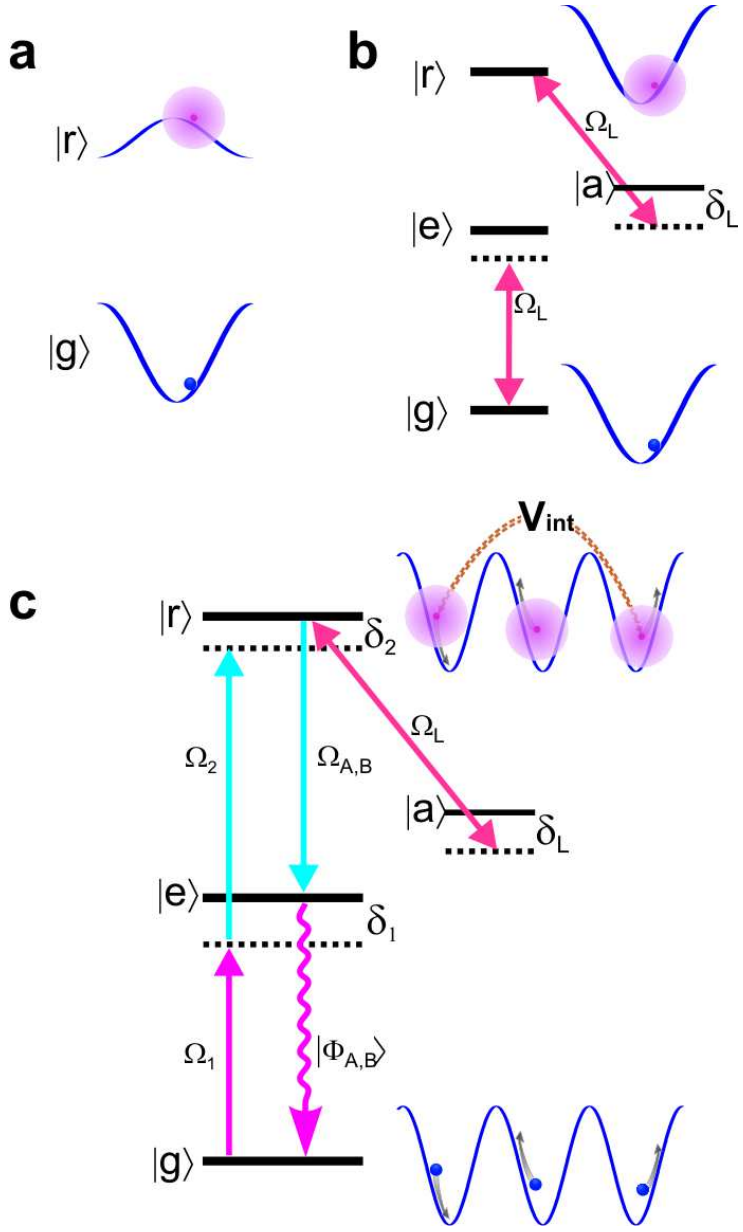

Figure 4.1.1: **State-insensitive trapping for Rydberg state. a**, The far-off-resonance optical dipole traps that are attractive for ground states are usually repulsive for high-lying Rydberg states. **b**, The 1004 nm lattice field is tuned to the blue side of the $|r\rangle = |90s_{1/2}\rangle \leftrightarrow |a\rangle = |6p_{1/2}\rangle$ transition to equalize the trapping potentials of the ground $|g\rangle = |5s_{1/2}\rangle$ and $|r\rangle$ levels. (A state-insensitive lattice field at 1012 nm can be realized using the $|r\rangle \leftrightarrow |6p_{3/2}\rangle$ transition.) **c**, Laser fields Ω_1 at 795 nm and Ω_2 at 474 nm are detuned by δ_2 from the two-photon atomic resonance $|g\rangle \leftrightarrow |r\rangle$, and by $\delta_1/2\pi = -40$ MHz from the intermediate level $|e = 5p_{1/2}, F = 1\rangle$. Laser fields $\Omega_{A,B}$ are resonant on the $|r\rangle \leftrightarrow |e\rangle$ transition.

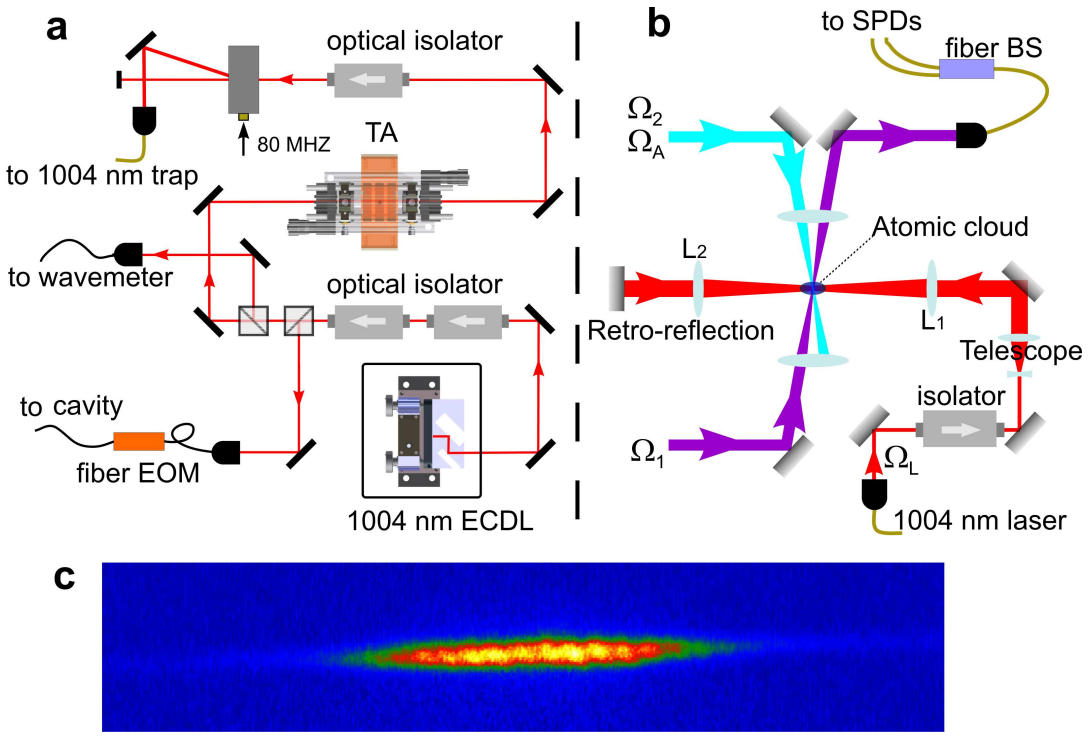

Figure 4.2.1: **1004 nm trapping setup. a,** The 1004 nm laser system for generating trapping light. **b,** Essential elements of the experimental setup. **c,** Fluorescence imaging of the atoms trapped in the 1004 nm optical lattice.

protect the fiber tip from the retro-reflected trapping light. With all the transmission (AOM and two isolators) and fiber coupling losses, the trapping beam has about 0.3 W of power at the atoms, see Figure 4.2.1 (b). With two telescopes and a final lens (L1, 30 cm focus length), the trapping beam is tightly focused with Gaussian waists of $w_y = 18$ μm and $w_z = 50$ μm along the transverse dimensions. The lens (L2) for the retro-reflected beam has a short focus length (20 cm) to compensate for the losses of power at the glass cell. The size of the trapped atomic cloud is ~ 10 μm and 40 μm in the y- and z- directions, respectively, as shown in Figure 4.2.1 (c). The 795 nm laser field (Ω_1) and 474 nm laser fields ($\Omega_{2,A}$) for Rydberg excitation and retrieval are aligned perpendicular to the trapping light with 9 μm wasits at the atoms. The retrieved light field, which shares the same spatial mode as the Ω_1 field, is coupled into a fiber beam-splitter (BS) and detected by two single photon detectors (SPD).

4.3 Magic condition: cancellation of differential a.c. Stark shifts

In order to study state-insensitive trapping, we drive the ensemble into the collective state $|R\rangle$ by two-photon excitation with 795 nm field Ω_1 and a 474 nm field Ω_2 for a period $T_e = 1$ μs, as shown in Figure 4.1.1 (c). After a storage period $T_s \simeq 0.2$ μs, the atoms are coherently driven on the $|r\rangle \leftrightarrow |e\rangle$ transition by a retrieval field Ω_A. The ensuing cooperative emission on the $|e\rangle \leftrightarrow |g\rangle$ transition leads to atom-light mapping $|R\rangle \rightarrow |\Phi\rangle_A$ [66].

We compare the excitation spectra for untrapped atoms with those taken at different values of lattice detuning δ_L, see Figure 4.3.1(a). The data are fit by a pair of Lorentzian profiles. The two peaks correspond to the Zeeman component of Rydberg level $|r\rangle$. The differential trap potential δU averaged over the atomic distribution gives the spectral line shift $\delta_2^s = \overline{\delta U}/h$, whereas the root-mean-square deviation of the differential trap potential $(\overline{\delta U^2} - \overline{\delta U}^2)^{1/2}$ increases the spectral linewidth Γ. The fit for $\delta_L^m/2\pi \approx 51$ MHz (green curve) is nearly indistinguishable from the fit for untrapped atoms (black curve), with zero spectral shift ($\delta_2^s/2\pi = 0.01(2)$ MHz) and no line broadening (measured widths $\Gamma/2\pi = 0.71(1)$ MHz and $0.74(2)$ MHz for trapped and untrapped atoms, respectively). In contrast, when the lattice is detuned from the magic condition, the transition frequency is shifted ($\delta_2^s/2\pi = 2.75(2)$ MHz and $1.58(2)$ MHz) and $\Gamma/2\pi$ is increased to $0.95(1)$ and $0.86(1)$ MHz, for the red and blue lattice detuning, respectively. Lattice-induced off-resonant population $p_a \simeq 0.02$ of level $|a\rangle$ causes a decay of Rydberg level $|r\rangle$ with lifetime $\tau_s \simeq 6$ μs.

In Figure 4.3.1(b) we display spectral shift as a function of lattice detuning. Each data point and the associated error bar are extracted from a spectrum of the type shown in Figure 4.3.1(a). Positions of the $|6p_{1/2}\rangle$ hyperfine resonances are extracted from a theoretical fit (solid curve). Using this fit and the measured atom temperature $T \simeq$

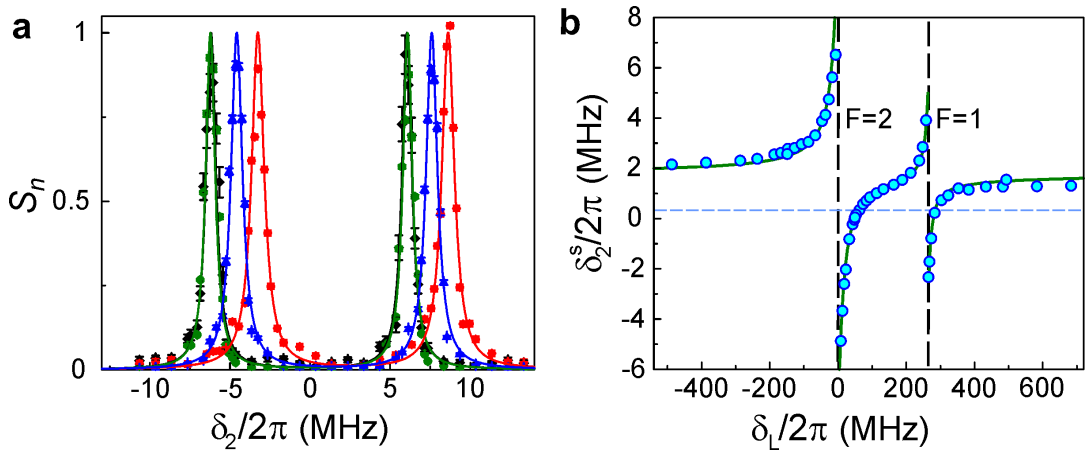

Figure 4.3.1: **State-insensitive optical trapping. a,** Normalized Rydberg excitation spectra $S_n(\delta_2)$, for untrapped (diamonds) and trapped in a lattice with detuning $\delta_L/2\pi \simeq (51, -100, 495)$ MHz (circles, squares, triangles). **b,** Spectral shift $\delta_2^s/2\pi$ as a function of lattice-detuning δ_L. The data are fitted (solid curve) to the expected form, with the dashed vertical lines corresponding to the inferred positions of level $|a\rangle$ hyperfine components. The error bars represent ± 1 standard deviations $(\sqrt{M})$ for M photoelectric counting events.

25 μK, we obtain the maximum trap depth for the ground atoms $U_g/k_B \simeq 100$ μK. The dashed horizontal line indicates the spectral shift $\delta_2^s/2\pi = 0.33$ MHz for which the lifetime of the ground-Rydberg coherence is maximized. We estimate that the root-mean-square deviation of the differential trap potential averaged over the atom spatial positions and energies reaches its minimum value $(\overline{\delta U^2} - \overline{\delta U}^2)^{1/2}/h|_{min} \simeq 0.03$ MHz at a detuning $\delta_L/2\pi = 58$ MHz. This is a result of the ponderomotive part of the Rydberg trapping potential being only partially sensitive to the lattice intensity modulation, as the Rydberg atom size ~ 1 μm is greater than the 0.5 μm lattice period.

4.4 Atom confinement and coherence times

In contrast to our near-resonant blue-detuned trap, typical far-off-resonance optical trapping potentials are repulsive for Rydberg levels, leading to fast dephasing of the ground-Rydberg optical coherence. Therefore, an uncompensated lattice has to be

turned off to avoid such dephasing, greatly reducing experimental rates [17, 37, 57, 62, 109]. In Figure 4.4.1 (a), P with the lattice shut off for the Rydberg excitation sequence is shown as diamonds. An exponential fit yields the decay constant $\tau_u = 0.76(1)$ ms, with the resulting rate of single photon detections $S_u \simeq 10$ Hz.

To investigate the temporal dynamics of atom confinement, we perform the Rydberg excitation-retrieval sequence with the lattice at a magic detuning $\delta_L^m/2\pi \simeq 58$ MHz. As shown in Figure 4.4.1 (a), we measure the probability of a photoelectric detection per experimental trial P as a function of atom holding time in the lattice T_h (solid circles). The data are fitted with an exponential function $\sim e^{-\frac{t}{\tau}}$. The fit gives a $1/e$ lifetime of $\tau_t = 74(3)$ ms. The decay is likely associated with atom loss due to light-induced collisions by way of the optical pumping fields, as the value of the lifetime is strongly sensitive to the intensity of the latter. We are exploring polarization-gradient cooling within the Rydberg excitation sequence, aiming to extend the trap lifetime towards and beyond the atomic lattice lifetime $\tau_b = 0.3$ s set by background collisions with thermal Rb vapor.

The inset of Figure 4.4.1 (a) shows P as a function of single-atom Rabi angle $\theta \equiv \Omega_1\Omega_2/(2\delta_1)$ for lattice-confined atoms. A 50 μs data acquisition period per lattice loading is employed for this measurement to limit the effect of atom number variation. The solid curve is a damped oscillation fit. The observed oscillation between the collective states $|G\rangle$ and $|R\rangle$ further confirms that our lattice preserves the quantum coherence between the ground and the Rydberg atom levels.

To further study the ground-Rydberg coherence, we store the optical atomic excitation for a time period T_s prior to the retrieval, with and without the lattice, as shown in Figure 4.4.1 (b). For the untrapped atoms the retrieved signal (diamonds) is fit with a Gaussian function $Ae^{-\frac{(T_s+T_d)^2}{\tau_m^2}}$, where $T_d \simeq 1$ μs is the delay between the centers-of-mass of the excitation and retrieved fields for $T_s = 0$ μs. The fit suggests a $1/e$ lifetime $\tau_m = 3.23(7)$ μs. The retrieved signal for lattice-confined atoms (circles) is fit by the

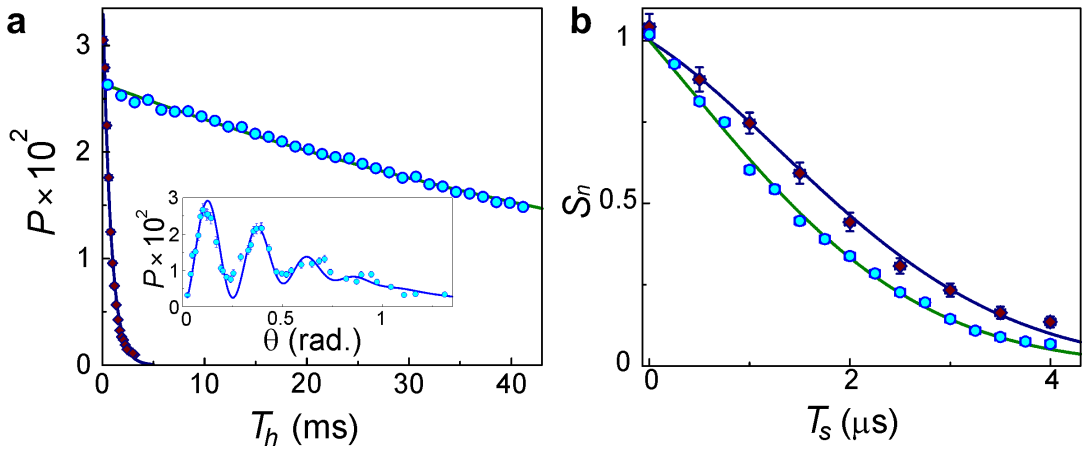

Figure 4.4.1: **Atom confinement and coherence times. a,** Probability of photoelectric detection P as a function of lattice holding time T_h. The inset shows a many-body rabi oscillation between states $|G\rangle$ and $|R\rangle$. **b,** Temporal dynamics of retrievable atomic excitation. Normalized photoelectric detection rate S_n for the retrieved signal is shown as a function of the storage time T_s. Diamonds/circles are for untrapped/trapped atoms. The error bars represent ± 1 standard deviations ($\sqrt{M}$) for M photoelectric counting events. The horizontal error bars represent the length of the retrieved light pulse.

product of the Gaussian function and an exponential decay $Ae^{-\frac{(T_s+T_d)^2}{\tau_m^2}}e^{-\frac{T_s}{\tau_s}}$, with inferred $\tau_s = 6.1(8)$ μs consistent with the expected lifetime of Rydberg level $|r\rangle$ as a result of off-resonant driving by the lattice field to level $|6p\rangle$:

$$\tau_s^e \simeq \tau_{6p} \times [4(\overline{\Omega_L^2} + \delta_L^2)/\overline{\Omega_L^2}] = 6.3\mu s. \tag{4.4.1}$$

Here $\overline{\Omega_L^2} \simeq 0.7\Omega_L^2$, and $\Omega_L/2\pi \simeq 20$ MHz is the Rabi frequency for the $|r\rangle \leftrightarrow |6p_{1/2}, F=2\rangle$ transition. The dephasing of the ground-Rydberg atomic coherence by the residual differential trapping potential is expected on a timescale of $\simeq 20$ μs.

Cooling the atoms to lower temperatures, e.g., by using Raman sideband techniques, and lowering the lattice depths could increase τ_s^e up to tens of microseconds, as the undesirable population of the $|6p_{1/2}\rangle$ level is approximately linear in the lattice field intensity. Motional decoherence leading to finite value of τ_m can be suppressed

by employing a lattice geometry with an additional periodicity of the trapping potential along the direction of the spin wave (y-axis). Longer coherence lifetimes for the Rydberg coherence will allow higher fidelities of entanglement and quantum gate operations.

4.5 Analysis of differential trapping potential

To equalize the trapping potentials for the ground $|g\rangle = |5s_{1/2}\rangle$ and a Rydberg level $|r\rangle$, the lattice field is tuned to near-resonance between the $|90s_{1/2}\rangle$ Rydberg level and either $|6p_{1/2}\rangle$ level at 1004 nm, or the $|6p_{3/2}\rangle$ level at 1012 nm. The trapping potential for the ground atoms is

$$U_g(\mathbf{r}) \simeq U_g^m \cos^2(k_L x) \exp(-z^2/w_z^2 - y^2/w_y^2). \tag{4.5.1}$$

with maximum trap depth $U_g^m = -\alpha_0 \mathscr{E}_0^2/4$. Here $\mathscr{E}_0$ is the amplitude of the lattice field, α_0 is the scalar atomic polarizability, $k_L = 2\pi/\lambda_L$. The trapping potential $U_r(\mathbf{r})$ for atomic level $|r\rangle$ is given by a sum of the ponderomotive potential:

$$U_{pm}(\mathbf{r}) \simeq (U_{pm}^1 + U_{pm}^2 \cos^2(k_L x)) \exp(-z^2/w_z^2 - y^2/w_y^2) \tag{4.5.2}$$

and of the near-resonant contribution:

$$U_n(\mathbf{r}) \simeq U_n^m \cos^2(k_L x) \exp(-z^2/w_z^2 - y^2/w_y^2). \tag{4.5.3}$$

The maximum value of $U_n(\mathbf{r})$ has a dispersive form:

$$U_n^m = -\frac{\hbar}{2} \sum [\mathrm{sgn}(\delta_L - \delta\omega_i) \sqrt{(\delta_L - \delta\omega_i)^2 + \Omega_i^2} - (\delta_L - \delta\omega_i)], \tag{4.5.4}$$

with the sum over the hyperfine components of level $|a\rangle$ separated by $\hbar\omega_i$ from the hyperfine sub-level with the lowest value of hyperfine number F.

At certain (magic) values of lattice detuning δ_L^m, trap depths for levels $|g\rangle$ and $|r\rangle$ are equal, $\delta U^m = U_g^m - U_r^m = 0$. In this case the motional degrees of freedom are approximately decoupled from the internal levels $|g\rangle$ and $|r\rangle$, and the dephasing of the optical atomic coherence is suppressed. The suppression is not complete because, while the near-resonant trapping potential $U_n(\mathbf{r})$ of Rydberg level has exactly the same spatial dependence as ground-level potential $U_g(\mathbf{r})$, the ponderomotive term $U_{pm}(\mathbf{r})$ has the U_{pm}^1 term without the $\cos^2(k_L x)$-dependence. The partial mis-match in the spatial profiles of the trapping potentials for levels $|g\rangle$ and $|r\rangle$ may lead to an additional spin-wave dephasing.

Using a Gaussian spatial distribution of atoms in the trap $P(x,y,z)$, we obtain by numerical integration the average differential potential $\overline{\delta U}$:

$$\begin{aligned}\overline{\delta U} &= \int \delta U(x,y,z) P(x,y,z) dxdydz \\ &\simeq 0.7(U_n - U_g + U_{pm}^2) + 0.9U_{pm}^1. \end{aligned} \tag{4.5.5}$$

Similarly, we can evaluate the mean-square-root deviation of the differential potential $(\overline{\delta U^2} - \overline{\delta U}^2)^{1/2}$. Its minimum value is $\sqrt{\overline{\delta U^2} - \overline{\delta U}^2}|_{min}/h \simeq 0.015 U_g/h = 31$ kHz, using $U_g/h \simeq 2$ MHz. The average differential potential is $\overline{\delta U}/h \simeq 0.09 U_g \simeq 0.2$ MHz, which should be compared with the measured value $0.33(7)$ MHz. The fits to the data in Figure 4.6.1 are based on this model. From this fit, we extract ground atom trap depth of 100 μK, which should be compared with calculated maximum value of 137 μK.

When $\delta_L \neq \delta_L^m$, the dephasing due to the differential potential decreases the re-

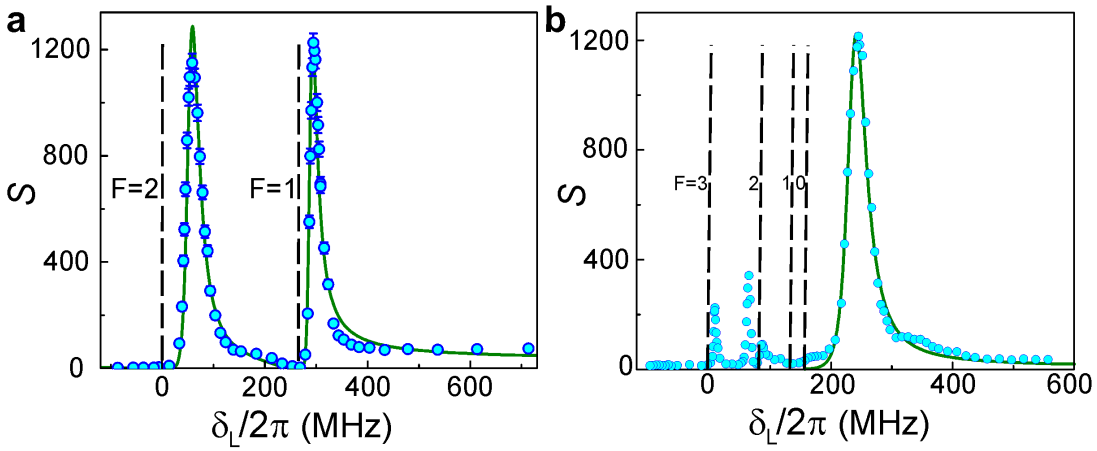

Figure 4.6.1: **Single photon source based on state-insensitive trapping using the $|90s_{1/2}\rangle \leftrightarrow |6p_{1/2,3/2}\rangle$ lattice-field atomic resonance. a,** The photoelectric detection rate S by detectors D_1 and D_2. The solid curve is a theoretical fit. **b,** The photoelectric detection rate S is maximized at lattice field detuning δ_L when the light shift on Rydberg level equals that of the ground level. The center-of-mass position of the $|6p_{3/2}\rangle$ hyperfine manifold $F = 0,1,2,3$ is inferred from the theoretical fit (solid curve) based on our model.

trieved signal by a factor $[1+0.25[\tau_r k T_a \overline{\delta U}/(U_g^m \hbar)]^2]^{-\frac{3}{2}}$; here $\tau_r \simeq 1$ μs is the protocol duration, T_a is atom temperature [69]. In addition, the lattice field populates the $|6p_{1/2(3/2)}\rangle$ level, resulting in spontaneous emission on the $|6p_{1/2(3/2)}\rangle \rightarrow |5s_{1/2}\rangle$ transition, and reduction of the retrieved signal by factor:

$$\prod_i \exp(-(\tau_r/\tau_{6p}) \times 0.25[\overline{\Omega_i^2}/(\Delta_i^2 + \overline{\Omega_i^2})]), \tag{4.5.6}$$

where Ω_{Li} is the Rabi frequency for the $|r\rangle \leftrightarrow |a, F = i\rangle$ transition, averaging $\overline{\Omega_{Li}^2} \simeq 0.7\Omega_{Li}^2$ accounts for distribution of atom positions in the lattice, $\Omega_{L1}/2\pi \simeq 12$ MHz, $\Omega_{L2}/2\pi \simeq 20$ MHz, and $\tau_{6p} = 0.12$ μs is the atomic lifetime of the $|6p\rangle$ level. The fits in Figure 4.6.1 incorporate these features.

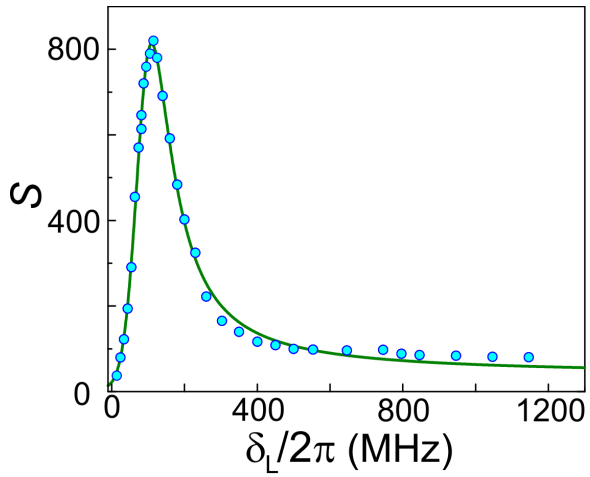

Figure 4.6.2: **Magic trap for $81s_{1/2}$, state.** The photoelectric detection rate S by detectors D_1 and D_2 is maximized at lattice field detuning $\delta_L \sim 150$ MHz when the light shift on Rydberg level equals that of the ground level. The solid curve is a theoretical fit with the same model used in Figure 4.6.1.

4.6 Single photon source with magic trapping

The Rydberg excitation blockade demonstrated in Chapter III allows the preparation of high quality single photons ($g^{(2)}(0) = 0.006(6)$) [17]. The single photon generation rate was ~ 10 Hz, limited by the fact that we have to turn off the optical trapping field before Rydberg excitation. With the state-insensitive trapping technique developed here, we are now able to keep the optical lattice during the Rydberg excitation. With every loading of the lattice, the experimental protocol can be repeated for 80,000 times, resulting in a large enhancement in photon generation rate.

Figure 4.6.1 (a) displays the rate of photoelectric detection S as a function of δ_L. The two peaks correspond to the $|6p_{1/2}, F = 1\rangle$ and $|6p_{1/2}, F = 2\rangle$ hyperfine components. The peak value $S_p \approx 1200$ Hz for magic-valued detuning $\delta_L^m/2\pi \simeq 58$ MHz and 294 MHz is more than two orders of magnitude higher compared to using untrapped atoms [17, 37, 109]. Taking into account the photon transmission and detection efficiency η_{LD}, we get the single photon generation rate ~ 5 KHz.

We also employed the $|a\rangle = |6p_{3/2}\rangle$ level, with the magic lattice wavelength $\lambda_L =$ 1012 nm, to enhance the single photon generation rate, Figure 4.6.1 (b). The peak count rate $S_p \approx 1200$ Hz is similar to that using the $|a\rangle = |6p_{1/2}\rangle$ level. Only the large peak in Figure 4.6.1(b) is fitted with a theoretical curve based on the same model. The smaller peaks are close to the respective atomic hyperfine resonances, and therefore must be treated without adiabatic elimination of level $|a\rangle$. More detailed analysis should also include effects of atom heating by the repeated Rydberg excitation cycles. The magic trapping technique developed here can be in principle applied to all the Rydberg *s* and *d* levels. We also demonstrated the state-insensitive trapping for $|r\rangle = |81s_{1/2}\rangle$ state, shown in Figure 4.6.2. The peak is fitted with same theoretical curve used in Figure 4.6.1, with a detuning $\delta_L \sim 150$ MHz.

CHAPTER V

Deterministic atom-photon entanglement

This chapter is based on Ref. [18].

5.1 Introduction

The generation, distribution, and control of entanglement across quantum networks is one of the major goals of quantum information science [15, 49]. In previous studies microwave or radio-frequency coherences between the ground hyperfine atomic levels have been entangled with spontaneously emitted light [38, 40, 110, 111]. The intrinsically probabilistic character of the spontaneous emission process leads to *a posteriori* atom-light entanglement and concomitantly long entanglement generation times, limiting realized network implementations to just two nodes [112–115]. By confining single atomic emitters in high-finesse optical cavities, deterministic atom-photon entanglement protocols become possible [116, 117]. Alternatively, quantum networks of superior scaling can be based on entanglement between light fields and collective excitations created in an ultra-cold atomic gas by deterministic Rydberg-level interactions [49, 50, 66]. Based on the achieved separation of the external and internal atomic degrees of freedom with state-insensitive Rydberg trapping, we demonstrate the entanglement between an optical atomic coherence and a light wavepacket, *a priori*. Our results pave the way for functional, many-node quantum networks capable of deter-

ministic quantum logic operations between long-lived atomic memories.

Ensembles of ultra-cold atoms confined in conservative optical potentials are promising candidates for the realization of networks capable of quantum logic operations and long-term storage of quantum states [49]. Such networks should enable intrinsically secure modes of communication [15] and distributed quantum computation [110], and allow investigations of quantum phase transitions and entanglement percolation [118]. Atoms store quantum information that is transmitted by light, with atom-light entanglement being the key ingredient that underpins the networking protocols [38, 40, 110, 111, 116].

While weak interactions between ground-level atoms make them ideal memories, implementations of deterministic quantum logic gates and entanglement demand strong atom-atom interactions. For Rydberg atoms of principal quantum number n effective electric dipoles are larger by a factor $\sim n^2$ compared to ground-level atoms. The strength of interaction between two atoms $V \sim n^{11}$ in the van der Waals regime [49,51]. For $n \gtrsim 70$ and atom separations of $\lesssim 10\ \mu$m, $V \gtrsim 1$ MHz, allowing entanglement operations in less than one μs [52, 53]. Broad efforts have been underway to achieve quantum entanglement in mesoscopic ensembles with Rydberg interactions [20, 21, 50, 66]. Enhanced optical nonlinearity under conditions of electromagnetically-induced transparency for Rydberg excitation has been realized [119] as has a Rydberg single-photon source relying on the dephasing of multiply-excited spin-waves [37]. Many-body Rabi oscillations [17], interaction-induced spatial correlations of Rydberg atoms [109, 120], and anti-bunching of light transmitted through the atomic gas [57, 62] have been reported also.

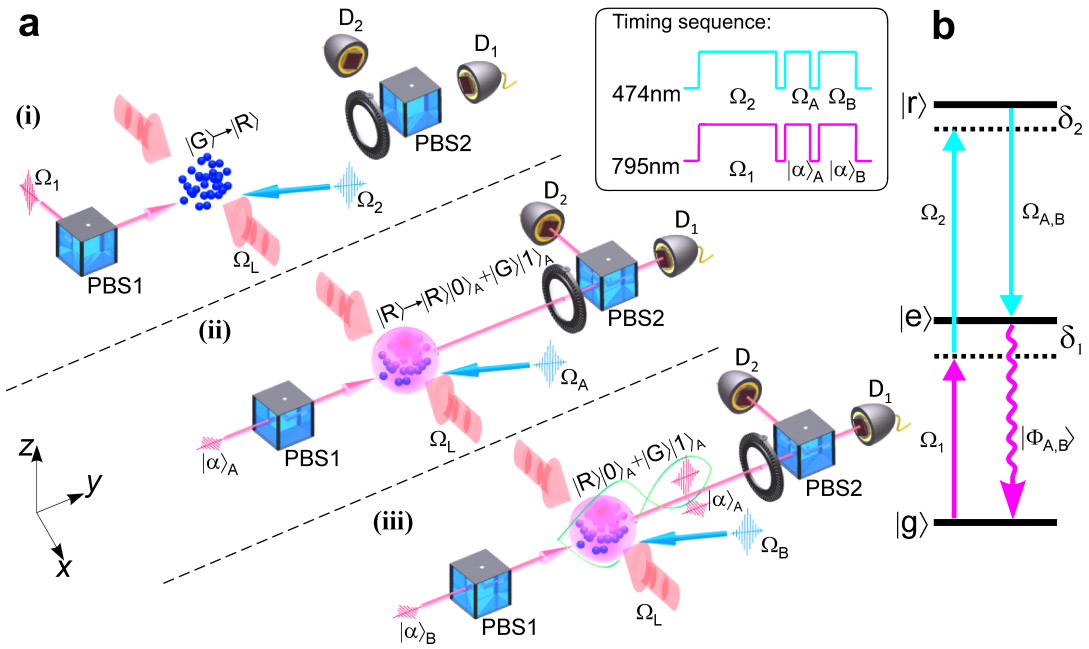

Figure 5.1.1: **Overview of the entanglement protocol. a,** An ultra-cold gas is confined in a one-dimensional optical lattice at 1004 nm. Three main steps of the entanglement protocol are illustrated. (i) The atomic ensemble is driven from the collective ground state $|G\rangle$ into the singly-excited state $|R\rangle$. (ii) By applying a laser field Ω_A, an entangled state $|R\rangle|0\rangle_A + |G\rangle|1\rangle_A$ is generated. The retrieved field $|\Phi\rangle_A$ is mixed with coherent field $|\alpha\rangle_A$ using polarizing beam splitters PBS1 and PBS2, followed by measurement at single-photon detectors D_1 and D_2. (iii) The remaining spin wave is mapped into field $|\Phi\rangle_B$ by the laser field Ω_B, mixed with $|\alpha\rangle_B$, and measured at D_1 and D_2. A half waveplate before PBS2 rotates polarizations of $|\Phi\rangle_{A,B}$ and $|\alpha\rangle_{A,B}$ by 45°. The inset shows the timing sequence for the 474 nm and 795 nm fields. **b,** Atomic levels of ^{87}Rb used in the experiment. The 1004 nm lattice field is tuned to the blue side of the $|r\rangle = |90s_{1/2}\rangle \leftrightarrow |a\rangle = |6p_{1/2}\rangle$ transition to equalize the trapping potentials of the ground $|g\rangle = |5s_{1/2}\rangle$ and $|r\rangle$ levels (A state-insensitive lattice field at 1012 nm can be created by tuning to the $|r\rangle \leftrightarrow |6p_{3/2}\rangle$ transition). Laser fields Ω_1 at 795 nm and Ω_2 at 474 nm are detuned by δ_2 from the two-photon atomic resonance $|g\rangle \leftrightarrow |r\rangle$, and by $\delta_1/2\pi = -40$ MHz from the intermediate level $|e = 5p_{1/2}, F = 1\rangle$. Laser fields $\Omega_{A,B}$ are resonant on the $|r\rangle \leftrightarrow |e\rangle$ transition.

5.1.1 Entanglement protocol

The matched trapping potentials described in Chapter IV preserve the ground-Rydberg quantum optical coherence, enabling the initial generation of *a priori* entanglement of an optical ground-Rydberg coherence and a light field. As illustrated in Figure 5.1.1, an ensemble of atoms is driven in resonance between the ground atomic level $|g\rangle = |5s_{1/2}\rangle$ and a Rydberg level $|r\rangle = |90s_{1/2}\rangle$. As a result of the Rydberg excitation blockade [50], the ensemble undergoes a many-body Rabi oscillation between the collective ground state $|G\rangle \equiv \prod_{i=1}^{N} |g\rangle_i$ and the singly-excited state $|R\rangle \equiv 1/\sqrt{N}\sum_{i=1}^{N} |g\rangle_1 ... |r\rangle_i ... |g\rangle_N$ [17]. By stopping the oscillation at half-period, we prepare the ensemble, in the ideal case, in state $|R\rangle$. This state is coherently mapped into an entangled atom-light state by illuminating the atoms with a retrieval field Ω_A, chosen such that a read-out of about a half of the Rydberg spin-wave into a retrieved field $|\Phi\rangle_A$ occurs: $|R\rangle \rightarrow |R\rangle|0\rangle_A + |G\rangle|1\rangle_A$.

A phase dependent measurement of field $|\Phi\rangle_A$ is realized by mixing it with an orthogonally polarized coherent field $|\alpha\rangle_A = |\alpha| \exp(i\phi_A)$ using a beam splitter, with the outgoing (50:50 splitting) fields directed to a pair of single-photon detectors. After a storage period, the remaining atomic spin wave is mapped onto the second retrieved field $|\Phi\rangle_B$, and a phase-dependent measurement is done by mixing it with a coherent field $|\alpha\rangle_B = |\alpha| \exp(i\phi_B)$ and photoelectric detection of the resulting fields by the same single-photon detector pair. Atom-light entanglement is confirmed by analyzing the correlations of photoelectric detection events in the two measurements as a function of varying the phases ϕ_A and ϕ_B, and observing the violation of the Bell inequality [121].

5.2 Experimental methods

A magneto-optical trap of ^{87}Rb is loaded from background vapor for 90 ms. During the following 30 ms period, detuning of cooling light fields is increased, repumper intensity is decreased, and the atoms at peak density $\rho_0 \simeq 10^{12}$ cm^{-3} are loaded into an optical lattice formed by a retro-reflected, linearly (y-) polarized 0.22 W laser field at 1004 nm, with Gaussian waists of $w_y = 15$ μm and $w_z = 50$ μm along the y- and z-dimensions, respectively. The lattice field is the output of a tapered amplifier driven by an ECDL, frequency-locked to a reference cavity. The length of the reference cavity is actively stabilized with a 780 nm ECDL light which is locked to a rubidium saturation absorption spectral line. The extent of the atomic ensemble in the *y*-dimension is determined by the $\simeq 11$ μm waist of the lattice-confined atomic gas. The ensemble size in the *x*- and *z*- dimensions is $\simeq 9$ μm, determined by the waists of two-photon excitation fields Ω_1 and Ω_2. The number of atoms N involved in the excitation is $\simeq 10^3$. Untrapped atoms are allowed to fall away from the experimental region during a 15 ms period, in which a bias magnetic field of 4.3 G is turned on, and the atoms are optically pumped to the $|5s_{1/2}, F = 2, m_F = 0\rangle$ state. Afterwards, the 3 μs long experimental sequence for entanglement is repeated for 40 ms, with a 1 μs optical pumping period inserted every five cycles. The lattice-loading cycle is repeated every 180 ms.

Two-photon Rydberg level excitation is performed by a 795 nm laser field Ω_1 of 0.11 nW power and a 474 nm laser field Ω_2 of 10 mW power; both Ω_1 and Ω_2 are linearly polarized along the *z*-axis. The 795 nm light is derived from an ECDL. Light at 474 nm is produced by frequency-doubling of power-amplified 948 nm ECDL output. Both of the ECDLs are frequency-locked to a thermally stabilized ultra-low expansion glass cavity. The Ω_1 and Ω_2 fields are locked in two-photon resonance between the ground-level component $|5s_{1/2}, F = 2, m_F = 0\rangle$ and the $|90s_{1/2}, m = 1/2\rangle$ Rydberg

state.

The coherent fields $|\alpha\rangle_{A,B}$ used for entanglement verification are mixed with the excitation field Ω_1 at a PBS1 before entering the vacuum cell. The phases $\phi_{A,B}$ are controlled by the amplified output of an FPGA board-based direct digital synthesizer (DDS) driving acousto-optical modulators inserted into the laser field path. Since Ω_2 and $\Omega_{A,B}$ fields are propagating in the same spatial mode, the retrieved fields $|\Phi\rangle_{A,B}$ are phase-matched into the spatial mode of field Ω_1. For the entanglement protocol, field Ω_A has power 5 mW, while field Ω_B has power 25 mW. The fields $|\Phi\rangle_{A,B}$ are split by PBS2, with each of the two outputs coupled into a single mode fiber followed by a single-photon detector $D_{1,2}$. To avoid damaging the detectors by the Ω_1 field, gating AOMs are placed at the outputs of PBS2.

Every experimental trial data acquisition is triggered, and photoelectric events on detectors D_1 and D_2 are recorded within gated time intervals. The electronic time periods T_A and T_B are set to 100 ns. The coincidences between detector D_i in the interval A and detector $D_j (i \neq j)$ in interval B are used to determine the two-photon correlation function $E(\phi_A, \phi_B)$.

5.3 Hong-Ou-Mandel interference between single-photon and coherent fields

5.3.1 Results

Our method to verify atom-light entanglement relies on the indistinguishability of the light fields $|\Phi\rangle_{A,B}$ mapped from the atomic coherence and of the coherent laser fields $|\alpha\rangle_{A,B}$. To characterize the mode-matching of these fields, we perform a two-photon quantum interference measurement between $|\Phi\rangle_A$ and $|\alpha\rangle_A$. The two fields are com-

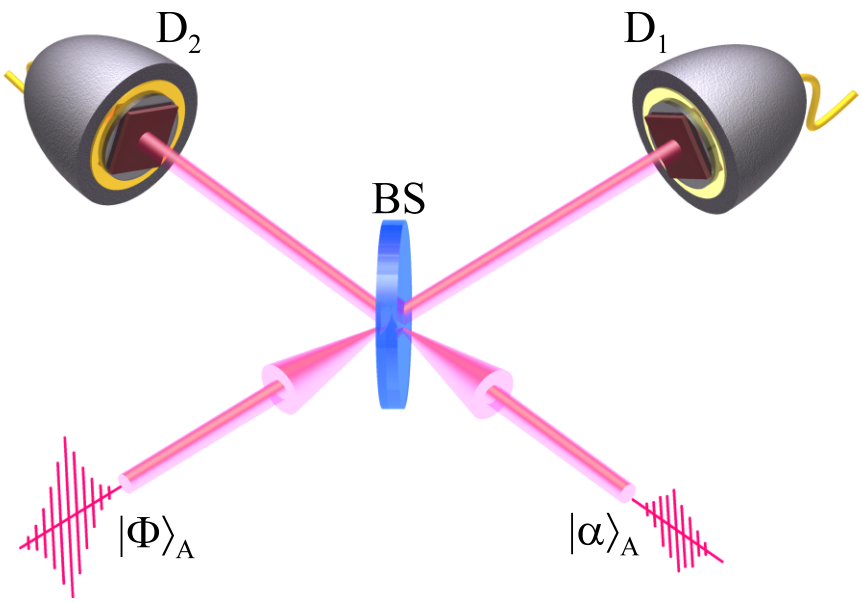

Figure 5.3.1: **Illustration of the Hong-Ou-Mandel interference measurement for fields $|\Phi\rangle_A$ and $|\alpha\rangle_A$.** The two fields are mixed on a 50:50 beam-splitter BS, whose outputs are measured by single-photon detectors D_1 and D_2.

bined on the polarization beam splitter PBS2, with the half wave plate rotated to equal the intensities of the two outputs. First, we determine probabilities of photoelectric detection at D_1 or D_2, p_1 and $|\bar{\alpha}|^2/2$, respectively, with either field $|\Phi\rangle_A$ or field $|\alpha\rangle_A$ input to the beam splitter only. Next, we analyze the rate of joint photoelectric detection events between the detectors D_1 and D_2 within the $T_A = 100$ ns electronic detection window, when one coherent field $|\alpha\rangle$ and the single photon $|1\rangle$ are mixed on the PBS2, see Figure 5.3.1. We observe a non-classical (Hong-Ou-Mandel) suppression in this rate as a result of quantum two-photon interference, as shown in Figure 5.3.2.

The degree of suppression allows us to infer the overlap of the two incoming light fields η, with $\eta = 1$ for fields that are indistinguishable within the detection window and $\eta = 0$ for completely distinguishable fields. We define the visibility of the interference $V = 1 - p_{21}/w_{21}$. Here w_{21} is the expected level of two-photon coincidences if the retrieved and the laser fields are completely distinguishable. We determine w_{21} using one- and two-photon photoelectric detection probabilities for separate measurements

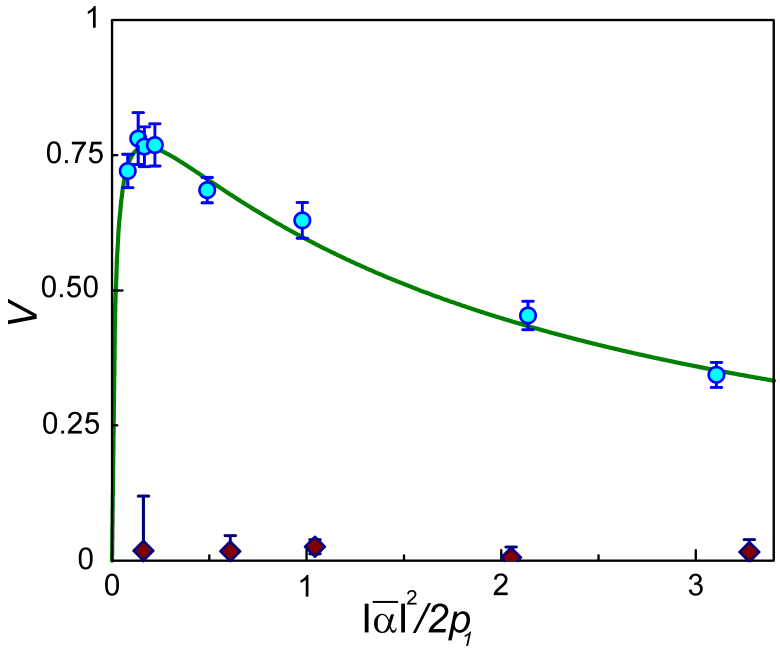

Figure 5.3.2: **Hong-Ou-Mandel interference between single-photon and coherent fields.** Visibility V of two-photon interference between the retrieved field $|\Phi\rangle_A$ and the coherent field $|\alpha\rangle_A$ as a function of $|\bar{\alpha}|^2/(2p_1)$; circles are for $|\alpha\rangle_A$ in resonance ($\delta \approx 0$) and diamonds off-resonance ($\delta/2\pi \approx -40$ MHz) with the field $|\Phi\rangle_A$. From the theoretical fit of our model (solid curve) we infer the overlap of the two fields $\eta = 0.90(2)$. The error bars represent ± 1 standard deviations ($\sqrt{M}$) for M photoelectric counting events.

using either of the two fields. When the frequency of the coherent field is matched to that of the retrieved light ($\delta \approx 0$ MHz), high visibility interference is observed. The data are fit to a model that accounts for imperfect field matching and a finite value of $g^{(2)}(0)$ for the retrieved field, with the best-fit value of the field overlap $\eta = 0.90(2)$. We approximate the case of distinguishable fields by introducing a frequency off-set $\delta/2\pi = -40$ MHz for the coherent field (diamonds), and in this case find negligible overlap $\eta_d = 0.03(2)$.

5.3.2 Analysis of interference visibility

We consider a single-photon source with a photoelectric detection probability $2p_1$ per trial, and $p_1^2 g^{(2)}(0)$ probability of a two-photon detection event. We assume $g^{(2)}(0) \ll 1$ and neglect the terms which correspond to more than two photons. The single-photon field is combined with a weak coherent field $|\alpha\rangle$ on a 50:50 beam splitter, see Figure 5.3.1. The probability of photoelectric detection due to the coherent field $|\bar{\alpha}|^2$ is reduced from the ideal $|\alpha|^2$ value by the field transmission and detection losses. Quantum interference of the one-photon components will result in the suppression of the coincidence detection probability between detectors D_1 and D_2 at the beam splitter outputs [122]. Here we derive an expression for the visibility of two-photon interference V, which we define as $1 - \frac{p_{12}}{w_{12}}$, where p_{12} is the observed coincidence probability, while w_{12} is the same probability expected for completely distinguishable single-photon and coherent light sources and for given one-photon and coincidence probabilities determined separately for the two fields.

The probability of detecting one photon in each of the two outputs of the beam-splitter for field overlap η for $|\bar{\alpha}|^2 \ll p_1$ is

$$p_{12} = p_1^2 g^{(2)}(0) + \frac{1}{4}|\bar{\alpha}|^4 + (1-\eta)p_1|\bar{\alpha}|^2, \tag{5.3.1}$$

where the first term describes the contribution of the two-photon component of the single-photon source, the second term corresponds to the two-photon component of the coherent field $|\alpha\rangle$, and the third term corresponds to mis-matched one-photon input components from the two fields. The third term vanishes when the single-photon and coherent fields have perfect spatial and temporal/frequency overlap ($\eta = 1$). For completely distinguishable fields ($\eta = 0$), we obtain

$$w_{12} = p_1^2 g^{(2)}(0) + \frac{1}{4}|\bar{\alpha}|^4 + p_1|\bar{\alpha}|^2, \tag{5.3.2}$$

so that the visibility

$$V = \frac{\eta p_1 |\bar{\alpha}|^2}{p_1^2 g^{(2)}(0) + \frac{1}{4}|\bar{\alpha}|^4 + p_1 |\bar{\alpha}|^2}. \tag{5.3.3}$$

In the limit of a perfect single-photon source and weak coherent light, $g^{(2)}(0) \to 0, |\alpha|^2 \to 0$, the visibility $V \to \eta$, limited only by the finite field overlap η.

An imbalance (0.52/0.48) of the field mixing at PBS2 is responsible for a portion of the observed overlap imperfection. The main reduction is likely due to frequency instability (linewidths $\leq$ 100 kHz) of the 795 nm laser providing the coherent light fields $|\alpha\rangle_{A,B}$, and the 948 nm laser whose frequency-doubled output at 474 nm is used as retrieval fields $\Omega_{A,B}$.

5.4 Entanglement between light and an optical atomic excitation

5.4.1 Entanglement creation and verification

To generate atom-light entanglement, we coherently split part of the collective atomic excitation into a retrieved light field: $|R\rangle \to |R\rangle|0\rangle_A + |G\rangle|1\rangle_A$. The atom-light splitting is achieved by applying field Ω_A at about a factor five lower intensity compared to full retrieval. The entanglement is verified by phase-sensitive measurement of both components of the quantum state, as shown in Figure 5.1.1 [121]. First, the retrieved field $|\Phi\rangle_A$ is interfered with a coherent field $|\alpha\rangle_A$ on a beam splitter, and the beam splitter outputs are measured by single-photon detectors D_1 and D_2 over a period A. To realize a phase-sensitive measurement of the atomic component, it is mapped, after a 0.1 μs delay, into a light field $|\Phi\rangle_B$ by application of the retrieval field Ω_B. This retrieved field $|\Phi\rangle_B$ is interfered with a coherent field $|\alpha\rangle_B$, and measured by detectors

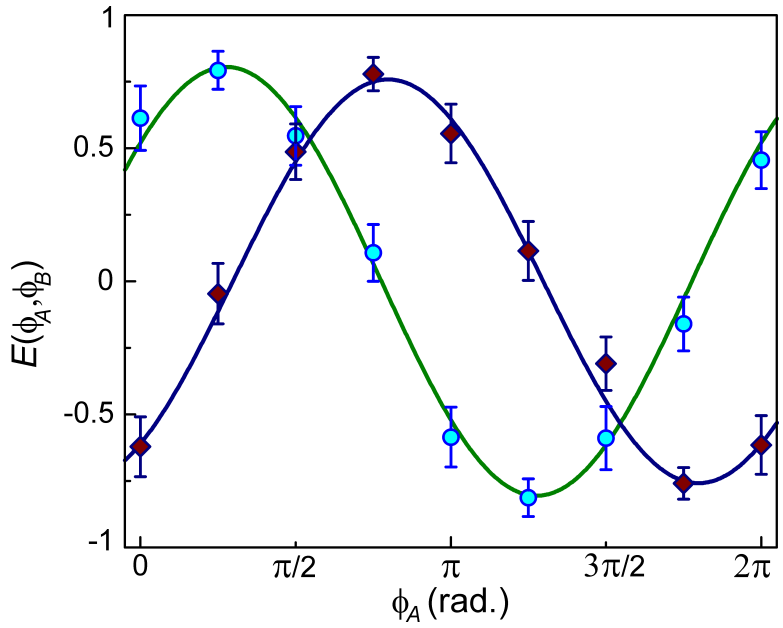

Figure 5.4.1: **Atom-light entanglement.** Correlation function $E(\phi_A,\phi_B)$ is displayed as a function of ϕ_A; circles are for $\phi_B=\pi/4$, diamonds are for $\phi_B=3\pi/4$. The curves are sinusoidal fits with inferred visibility $v_{\pi/4}=0.80(4)$, $v_{3\pi/4}=0.76(4)$. The error bars represent ±1 standard deviations $(\sqrt{M})$ for M photoelectric counting events.

D_1 and D_2 over a period B. We evaluate the correlation function $E(\phi_A,\phi_B)$ defined as

$$\frac{C_{12}(\phi_A,\phi_B^{\perp})+C_{21}(\phi_A,\phi_B^{\perp})-C_{12}(\phi_A,\phi_B)-C_{21}(\phi_A,\phi_B)}{C_{12}(\phi_A,\phi_B^{\perp})+C_{21}(\phi_A,\phi_B^{\perp})+C_{12}(\phi_A,\phi_B)+C_{21}(\phi_A,\phi_B)}, \tag{5.4.1}$$

where $C_{ij}(\phi_A,\phi_B)$ is the coincidence rate between detector D_i in detection period A and D_j in the detection period B; $\phi_B^{\perp}=\phi_B+\pi$. In Figure 5.4.1 the correlation function E is displayed as a function of ϕ_A, when ϕ_B is fixed at $\pi/4$ and $3\pi/4$, together with sinusoidal fits of adjustable visibility v. For our measured $g^{(2)}(0)\simeq 0.02$ and $\alpha^2/(4p_1)\simeq 0.08$, we expect $v\simeq 0.79$ based on our model (Section 5.4.2), in good agreement with the values $v_{\pi/4}=0.80(4)$ and $v_{3\pi/4}=0.76(4)$ extracted from the fits.

From measurements of $E(\phi_A,\phi_B)$, we determine the Bell parameter

$$S=E(\phi_A,\phi_B)+E(\phi_A',\phi_B)+E(\phi_A,\phi_B')-E(\phi_A',\phi_B'). \tag{5.4.2}$$

Table 5.4: **Entanglement verification by way of Bell's inequality**. Correlation function $E(\phi_A, \phi_B)$ and S based on 4254 events.

ϕ_A	θ_B	$E(\phi_A, \phi_B)$
0	$\pi/4$	0.57 ± 0.03
0	$3\pi/4$	-0.61 ± 0.04
$\pi/2$	$\pi/4$	0.57 ± 0.03
$\pi/2$	$3\pi/4$	0.53 ± 0.04
		$S = 2.27 \pm 0.07$

We use canonical settings $\phi_A = \pi/2$, $\phi'_A = 0$, $\phi_B = \pi/4$, $\phi'_B = 3\pi/4$, which in the ideal case results in $S = 2\sqrt{2}$, maximally violating the Bell inequality $|S| \leq 2$. The measured values of $E(\phi_A, \phi_B)$ are displayed in Table 5.4. The value $S = 2.27(7) \not\leq 2$ is in a clear violation of the Bell inequality and is consistent with the visibility of the fringes shown in Figure 5.4.1. We therefore verify unambiguously entanglement of an optical atomic coherence and a light field.

5.4.2 Analysis of non-ideal entangled state

The ideal entangled quantum state of $|1\rangle_A|G\rangle + |0\rangle_A|R\rangle$ is affected by several sources of imperfections. Allowing for imbalance λ in the matter-light mapping amplitudes for the two retrieval periods, the effective (unnormalized) quantum state becomes

$$\begin{aligned} |R\rangle &\longrightarrow (\sqrt{(1+\lambda)}|1\rangle_A|G\rangle + \sqrt{1-\lambda}|0\rangle_A|R\rangle) \\ &\longrightarrow (\sqrt{1+\lambda}|1\rangle_A|0\rangle_B + \sqrt{1-\lambda}|0\rangle_A|1\rangle_B). \end{aligned} \tag{5.4.3}$$

Including the coherent light fields employed in the measurement, the effective quantum state after PBS1 may be written as:

$$|\Psi\rangle \sim |\alpha\rangle_A|\alpha\rangle_B(\sqrt{1+\lambda}|1\rangle_A|0\rangle_B + \sqrt{1-\lambda}|0\rangle_A|1\rangle_B). \tag{5.4.4}$$

Using this effective quantum state together with beam splitter transformation rela-

tions describing the combined action of the half-wave plate and PBS2, we can derive the coincidence probabilities p_{ij} $(i,j=1,2)$ between detectors D_1 and D_2, where index i refers to measurement period A, and index j to period B. Including finite efficiencies of initial Rydberg excitation γ, matter-light mapping ς, and the linear optical transmission and detection losses ζ, we obtain:

$$p_{12} = p_{21} = \frac{1}{4}\{|\bar{\alpha}|^4 + 4p_1|\bar{\alpha}|^2[1-\sqrt{1-\lambda^2}\cos(\phi_A-\phi_B)]\},$$
$$p_{11} = p_{22} = \frac{1}{4}\{|\bar{\alpha}|^4 + 4p_1|\bar{\alpha}|^2[1+\sqrt{1-\lambda^2}\cos(\phi_A-\phi_B)]\},$$

where $p_1 = (\gamma\varsigma\zeta)/4$ and $|\bar{\alpha}|^2 = (\gamma\varsigma\zeta)|\alpha|^2$. In practice we need to add $\approx g^{(2)}(0)p_1^2$ to all p_{ij} due to the non-zero probability of having two photons in the nominally single-photon field. Additionally including a finite overlap of the single-photon and coherent fields η, we obtain

$$p_{12} = p_{21} = |\bar{\alpha}|^4/4 + g^{(2)}(0)p_1^2 + p_1|\bar{\alpha}|^2 -$$
$$p_1\eta|\bar{\alpha}|^2\sqrt{1-\lambda^2}\cos(\phi_A-\phi_B). \tag{5.4.5}$$

The measured rates $C_{11}(\phi_A,\phi_B)$ and $C_{22}(\phi_A,\phi_B)$ corresponding to p_{11} and p_{22} are affected by the spurious after-pulsing of the single photon detectors. To construct the function $E(\phi_A,\phi_B)$, we instead use the rates $C_{12}(\phi_A,\phi_B+\pi) = C_{11}(\phi_A,\phi_B)$ and $C_{21}(\phi_A,\phi_B+\pi) = C_{22}(\phi_A,\phi_B)$. We obtain $E(\phi_A,\phi_B) = v\cos(\phi_A-\phi_B)$, where fringe visibility

$$v = \frac{\eta\sqrt{1-\lambda^2}}{|\bar{\alpha}|^2/(4p_1) + 1 + (g^{(2)}(0)p_1)/|\bar{\alpha}|^2}. \tag{5.4.6}$$

The non-zero value of λ leads to a reduction of the visibility of the interference

fringes. Using measurements with coherent light fields blocked, we estimate $|\lambda| \leq 0.1$, so that the atom-light mapping imbalance produces visibility $\approx \sqrt{1-\lambda^2} \geq 0.995$. The imperfection of the single-photon source described by $g^{(2)}(0) = 0.020(2)$ and the finite degree of the fields overlap $\eta = 0.90(2)$ lead to a greater reduction. For $\alpha^2/(4p_1) \simeq 0.081(3)$ chosen to maximize visibility v inferred from Eq. 5.4.6, we find $v = 0.79(2)$. This value agrees with those extracted from the sinusoidal fits to the data in Figure 5.4.1, $v_{\pi/4} = 0.80(4)$, $v_{3\pi/4} = 0.76(4)$, and with the measured value of the Bell parameter $S = 2.27(7)$.

5.5 Violation of Bell's inequality with one photon

In 1991, Tan *et al*. proposed an experiment to demonstrate the non-locality of single particle by violating Bell's inequality with single photon instead of entangled photon pairs [121]. An illustration of their proposed experiment is shown in Figure 5.5.1 (a). A single photon field $|1\rangle$ is split at a beam-splitter into two beam path (a and b), creating a mode-entangled state $|1\rangle_a|0\rangle_b + |0\rangle_a|1\rangle_b$. The photons in path a and b are mixed with weak coherent light $|\alpha\rangle_a$ and $|\alpha\rangle_b$, respectively. The events at the single photon detectors are correlated. The coincidences are recorded with the phases difference $\phi_a - \phi_b$ of coherent light $|\alpha\rangle_a$ and $|\alpha\rangle_b$ changed over 2π. The resulting coincidence probabilities are:

$$p_{a_1b_2} = p_{a_2b_1} = \frac{1}{4}\{|\alpha|^4 + 4p_1|\alpha|^2[1+\sin(\phi_a-\phi_b)]\},$$
$$p_{a_1b_1} = p_{a_2b_2} = \frac{1}{4}\{|\alpha|^4 + 4p_1|\alpha|^2[1-\sin(\phi_a-\phi_b)]\}.$$

The coincidence rates oscillate sinusoidally as a function of phase difference $\phi_a - \phi_b$, with a visibility of $V = 1/(1+|\alpha|^2)$. Correlation function E and Bell parameter S can be constructed with measured values of coincidence rates at different phases ϕ_a

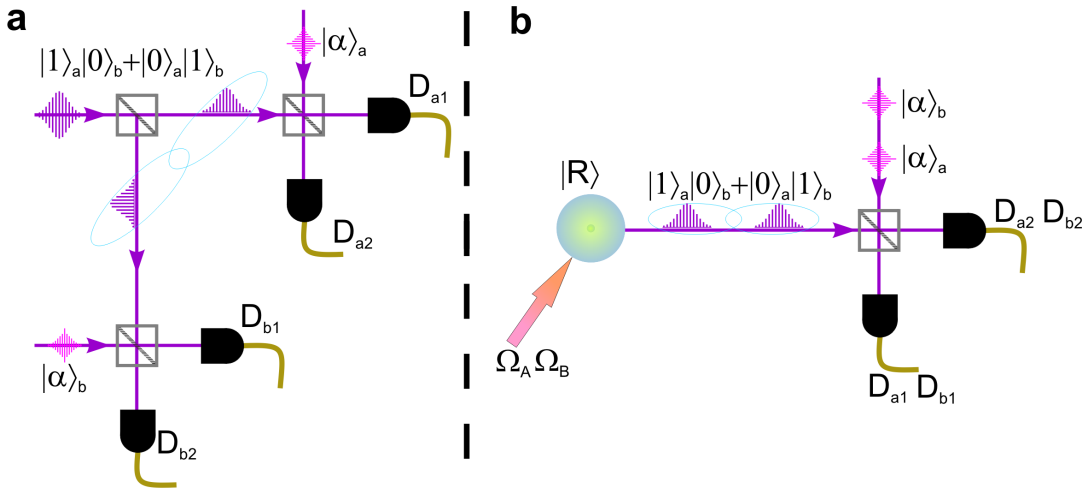

Figure 5.5.1: **Violation of Bell's inequality with one photon. a**, Illustration of the original propoal for single photon Bell's inequality violation. The single photon is split into two spatial modes and mixed with two weak coherent light fields. **b**, In our experiment, the single excitation is retrieved into two temporal modes and mixed with two coherent light fields.

and ϕ_b. The violation of Bell's inequality requires the visibility $V > 1/\sqrt{2} \sim 71\%$, which has not been achieved in previous experiments [123].

Our result on verifying the atom-light entanglement represents the first demonstration of the proposed experiment. As shown in Figure 5.5.1 (b), by controlling the power and duration of the two read-out fields $\Omega_{A,B}$, the Rydberg super-atom state $|R\rangle$ can be mapped into the mode-entangled (temporal) single photon state $|1\rangle_a|0\rangle_b + |0\rangle_a|1\rangle_b$. The phase sensitive measurements are performed by homodyning detection with weak coherent light $|\alpha\rangle_a$ and $|\alpha\rangle_b$. The only difference with the original proposal is that the single photon is split in two temporal modes instead of spatial modes. The observed visibilities of correlation functions $V \sim 0.8$ and the Bell parameter $S = 2.27(7)$ in our experiment support the prediction of Tan *et al*. [121].

5.6 Conclusion

By normalizing the value of the initial photoelectric detection probability $P_t \approx 0.028$ (reduced by the $|6p_{1/2}\rangle$ level decay compared to the corresponding value $P_u \approx 0.032$ for untrapped atoms), with the linear transmission and detection efficiency $\zeta = 0.25$ we estimate efficiency $\xi = 0.11(3)$ with which the entangled atom-light state is prepared, with the average value $\bar{\xi} = 0.08(2)$. Although photoelectric detection probabilities in our initial implementation are decreased from their ideal values by various preparation, transmission and detection inefficiencies, our entanglement generation and verification protocol is inherently deterministic.

To achieve long-term storage of atomic states, entanglement generation can be followed by mapping the ground-Rydberg coherences into the ground "clock" coherences. The differential ac Stark shift for the clock levels can be eliminated by directing the bias magnetic field $B = 4.3$ G along the lattice (x-) axis and choosing field ellipticity $\beta \approx 0.93$ [14]. Matter-light mapping efficiency can be increased by enclosing the atomic ensemble into a low- to medium-finesse optical cavity, with values of $\xi = 0.8$ having already been demonstrated [40].

In conclusion, we report the first realization of entanglement between an optical atomic coherence and a light field. Our demonstration relies critically on the achievement of state-insensitive optical confinement of atoms in their ground and Rydberg states. In contrast to prior probabilistic approaches where scalability is compromised by the need for multiple "repeat-until-success" entanglement generation attempts [15, 38, 40, 111], our protocol is intrinsically deterministic. Combined with minute-scale memory already demonstrated for the atomic clock coherences [14], our work leads to functional quantum networking architectures of superior scaling.

CHAPTER VI

Quantum memory with strong and controllable interaction

This chapter is based on Ref. [19].

6.1 Introduction

Realization of distributed quantum systems requires fast generation and long-term storage of quantum states [49]. Ground atomic states enable memories with storage times in the range of a minute [14], however, their relatively weak interactions do not allow fast creation of non-classical collective states. Rydberg atomic systems feature fast preparation of singly-excited collective states and their efficient mapping into single-photon [37, 57, 58] and entangled light fields [18]. But storage times in these approaches have not yet exceeded a few microseconds. Here, we realize a system that combines fast quantum state generation and long-term storage. An initially prepared coherent state of an atomic memory is transformed into a non-classical collective atomic state by Rydberg-level interactions in less than a microsecond. By sheltering the quantum state in the ground atomic levels, the storage time is increased by almost two orders of magnitude. This advance opens a door to a number of quantum protocols for scalable generation and distribution of entanglement [20–23].

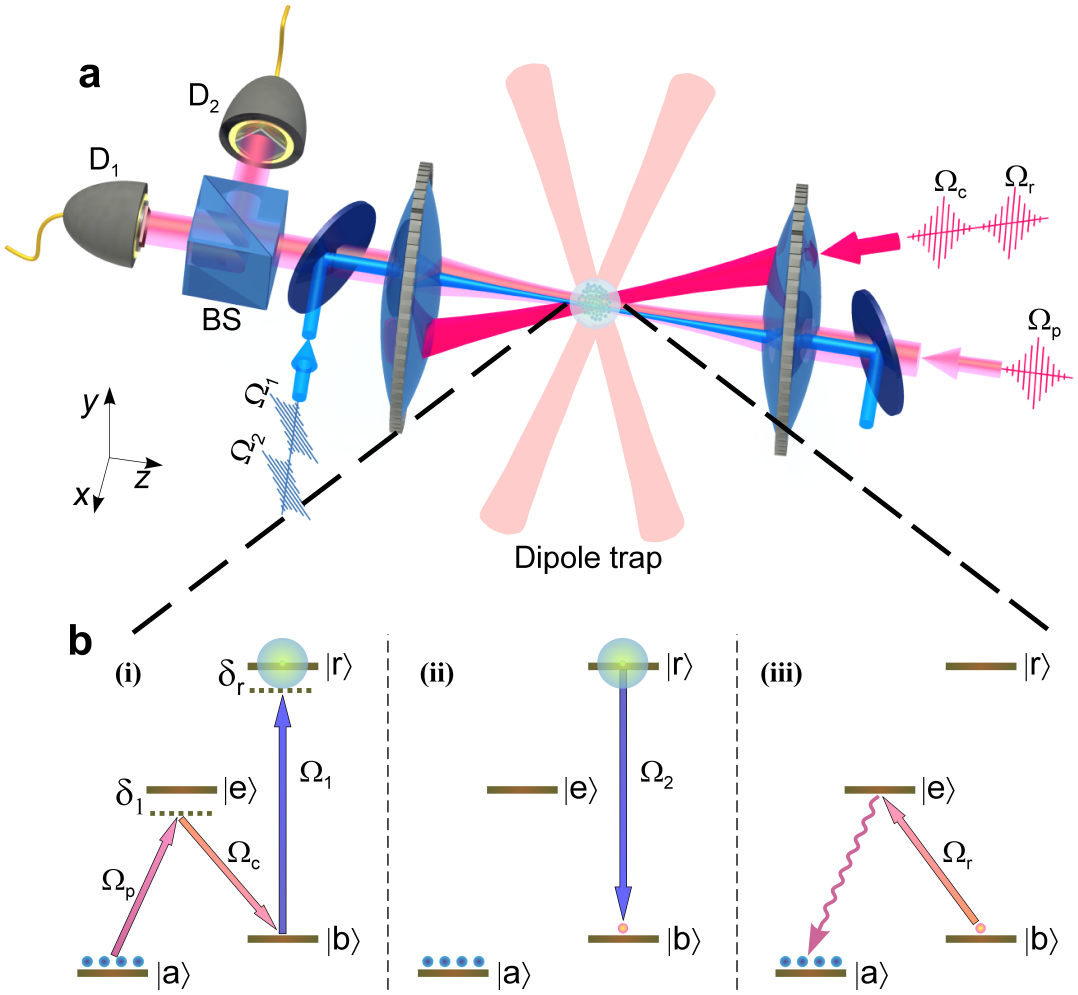

Figure 6.1.1: **Overview of the experiment. a,** Essential elements of the experimental setup. An ultra-cold ^{87}Rb gas is confined in a crossed dipole trap formed by two 1064 nm fields. Two 795 nm beams (probe and control) and a 297 nm beam are focused on the atomic sample with waists $(\omega_p, \omega_c, \omega_{1,2}) = (5, 25, 18)$ μm, respectively. The probe and control beam are aligned with an angle 3°, while the 297 beam counter-propagates with the probe beam. **b,** Level diagram and experimental protocol. (i) Atoms are initially prepared in state $|a\rangle$ by means of optical pumping. The atomic ensemble is driven from $|a\rangle$ to $|b\rangle$ by the probe field Ω_p and control field Ω_c. Next, the 297 nm field Ω_1 couples $|b\rangle$ directly to the Rydberg state $|r\rangle$, creating a singly-excited Rydberg state. (ii) By applying the 297 nm field Ω_2, the short-lived Rydberg excitation is mapped into the ground state $|b\rangle$ for storage. (iii) The ground-state excitation is retrieved by the read field Ω_r and measured at D_1 and D_2. The atomic levels involved are $|a\rangle = |5s_{1/2}, F = 1, m_F = 0\rangle$, $|b\rangle = |5s_{1/2}, F = 2, m_F = -2\rangle$, $|e\rangle = |5p_{1/2}, F = 1, m_F = -1\rangle$ and $|r\rangle = |np_{3/2}, m_J = -3/2\rangle$.

Atomic systems involving highly excited Rydberg states have recently become a leading player in the continuing quest to realize large-scale quantum networks [124]. An ultra-cold atomic ensemble in a quantum superposition of a ground and Rydberg state features both rapid and deterministic preparation of quantum states and their efficient transfer into single-photon light fields [50, 66]. Notable achievements include the demonstration of deterministic Rydberg single-photon sources [37, 57], atom-photon entanglement [18], many-body Rabi oscillations [17, 59–61], photon anti-bunching and interaction-induced phase shifts [62, 63], and single-photon switches [58, 64, 65]. In parallel to these efforts, significant advances have been made in employing Rydberg interactions for entanglement of pairs of neutral atoms [52–54] and many-body interferometry [56].

All these experimental demonstrations relied critically on the strong interactions between Rydberg atoms. The interactions prevent more than one atom from being excited into a Rydberg state within a volume called the blockade sphere if excitation into the Rydberg state is *slow* [50]. In the opposite limit of *fast* excitation to the Rydberg state, the interactions between the atoms act by dephasing the collective multi-atom states, thereby removing quantum state components with more than one excited atom from the observed Hilbert sub-space [101]. Both Rydberg blockade and dephasing mechanisms contribute to the sub-Poissonian statistics of the output light fields in experiments of Refs. [17, 37, 57, 62].

However, the large values of the electric dipole transition elements between Rydberg states also translate into a magnified sensitivity of Rydberg states to black-body radiation and ambient electric fields, leading to their relatively short lifetimes [49, 51]. Spontaneous emission, atomic motion, and collisions further limit storage times for the ground-Rydberg atomic coherence [37, 58]. In contrast, ground atomic states are ideal for preserving quantum coherence, but implementation of fast and deterministic quantum operations is challenging due to their weak interactions. For example,

deterministic single photons can be produced using measurement and feedback of Raman-scattered light fields [16], but the generation times are ~ 1 ms - three orders of magnitude longer than in Rydberg approaches. An attractive approach featuring the simultaneous achievement of fast quantum operations and long coherence times can be realized by employing Rydberg levels for interactions and ground atomic levels for storage [50].

Here we demonstrate a quantum memory where a non-classical polariton state created by Rydberg interactions is sheltered in the ground hyperfine sub-levels for long-term storage, as shown in Figure 6.1.1. Two 795 nm Raman fields (Ω_p and Ω_c) are applied to create a spin-wave within the ground hyperfine manifold states $|a\rangle$ and $|b\rangle$ in an approximately coherent state. Next, a 297 nm laser pulse Ω_1 couples state $|b\rangle$ directly to state $|r\rangle$ ($np_{3/2}$), creating a Rydberg polariton state. Subsequently, another 297 nm laser pulse Ω_2 transfers the excitation from the Rydberg state into state $|b\rangle$ for storage. After a storage period T_g in the ground states memory, the read-out field Ω_r converts the atomic excitation into the retrieved light field. The latter is directed onto a beam-splitter (BS) and is, subsequently, detected by single-photon detectors D_1 and D_2.

6.2 Experimental methods

6.2.1 Timing sequence

Before execution of the quantum memory protocol, optical pumping techniques are employed to prepare atoms in ground state $|a\rangle = |5s_{1/2}, F = 1, m_F = 0\rangle$ and to empty the $F = 2$ states. The success of our protocol relies critically on the optical pumping process, as the accumulation of unwanted atoms in $F = 2$ are detrimental to the Rydberg excitation process. To clean atoms in $F = 2$, we employ two laser fields: a π

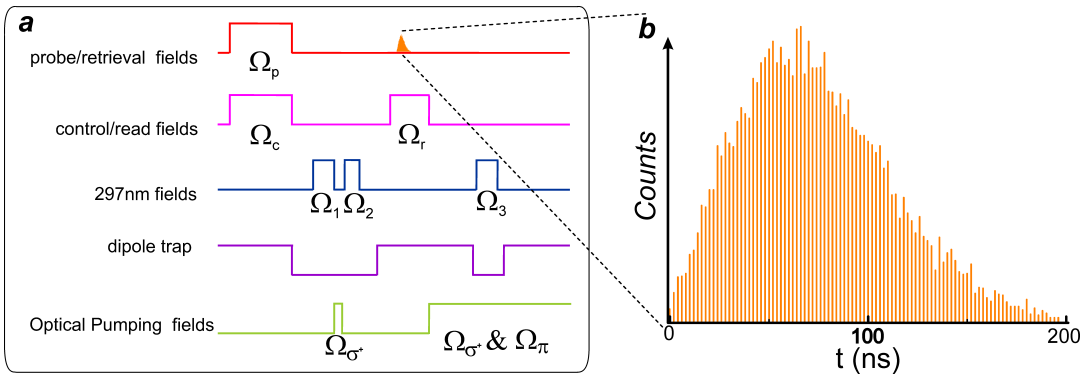

Figure 6.2.1: **Experimental sequence.** **a.** The timing sequence of the laser fields used in the quantum memory protocol. **b.** Temporal profile of the retrieved photon field.

polarized field Ω_π and a σ^+ polarized field Ω_{σ^+}. Both cleaning fields are resonant with the $|5s_{1/2}, F = 2\rangle \leftrightarrow |5p_{1/2}, F = 2\rangle$ transition. The Ω_π propagates along the x axis, while the Ω_{σ^+} field is mixed into the beam path of the control field Ω_c. The combination of Ω_π and Ω_{σ^+} fields ensures all of the Zeeman sublevels in $F = 2$ are addressed and thus no dark states are present. To prepare atoms into $F = 1, m_F = 0$, a π polarized optical pumping field Ω_{op} resonant with the $|5s_{1/2}, F = 1\rangle \leftrightarrow |5p_{1/2}, F = 1\rangle$ transition is used. After atoms are loaded and cooled in the dipole trap, the alternating pulses of the Ω_{op} field and the $\Omega_\pi + \Omega_{\sigma^+}$ fields are applied for 200 μs for optical pumping.

The 20-μs-long quantum memory protocol is repeated 8000 times after the sample preparation. The overall duration of one experimental cycle is 780 ms. Figure 6.2.1 (a) shows the detailed timing sequence within each experimental protocol. To avoid Rydberg-ground dephasing caused by the trapping potential, the dipole trap is turned off after the 2 μs Raman excitation with Ω_c and Ω_p fields. 700 ns after the trap is turned off, Rydberg excitation and transfer fields Ω_1 and Ω_2 are applied. The dipole trap is turned back on, and the read-out field Ω_2 converts the stored excitations into photons with a temporal width of 200 ns (Figure 6.2.1 (b)).

The repetition of quantum memory protocol could gradually populate the initially empty $|5s_{1/2}, F = 2\rangle$ levels and interfere with the Rydberg excitation process. To overcome this effect, we employ cleaning fields Ω_π and Ω_{σ^+} within the experimental protocol. To clean out the residual population in $|b\rangle$ after Rydberg excitation, an optical intensity modulator is used to generate a 200-ns-long Ω_{σ^+} field between Rydberg fields Ω_1 and Ω_2. After the excitations are retrieved, both Ω_π and Ω_{σ^+} fields are turned on for μs for further cleaning. Any excitations remaining in the Rydberg state could have detrimental effects on experiments like preventing further Rydberg excitation and fast atom loss. After the read-out, we turn off the dipole trap for 1 μs and recycle the residual Rydberg populations with a 700-ns-long 297 nm field Ω_3 resonant with the $|b\rangle \leftrightarrow |r\rangle$ transition. To keep our atomic sample polarized throughout the experiment, a 1 μs optical pumping period by the Ω_{op} field is repeated after every ten cycles.

6.2.2 Sample preparation

To quickly create a dense sample of ^{87}Rb in a low background pressure environment, a $2D^+$ magneto-optical trap (MOT) is first loaded from the background gas. The 3D MOT is then loaded from the cold atomic beam generated by the $2D^+$ MOT and directed through a differential pumping opening for 300 ms. For the following 22 ms, the gradient of the 3D MOT is increased to 25 G/cm to compress and load the atoms into an optical dipole trap formed by two orthogonally polarized YAG laser beams, intersecting at an angle of 22°. Sub-Doppler cooling of the atoms is performed by increasing the cooling light detuning and decreasing the power of repumper light for 12 ms.

The dipole trap beams have a total power of 5 W and transverse waists of 17 μm and 34 μm, resulting in a maximum trap depth of $\simeq$ 560 μK. The depth of the dipole trap is adiabatically lowered to $\simeq$ 30 μK during the 200 ms after the sub-Doppler

Table 6.5: **Frequencies of the UV light for the $|5s_{1/2}, F = 2\rangle \leftrightarrow |np_J\rangle$ transition**.

Rydberg level	frequency of UV light	wavelength of SHG light
19 $p_{3/2}$	997726.84 GHz	600.95104 nm
29 $p_{3/2}$	1005287.20 GHz	596.43152 nm
62 $p_{3/2}$	1009088.83 GHz	594.18453 nm
70 $p_{3/2}$	1009297.45 GHz	594.06172 nm

cooling stage to further cool the atoms. Eventually, the cloud has temperature $\sim 7\ \mu$K measured from thermal expansion measurement of the cloud. The peak atomic density is $\rho \sim 2 \times 10^{11} cm^{-3}$. The atomic ensemble has $\sim 10\ \mu$m size in the longitudinal ($z-$) dimension, while the $\sim 5\ \mu$m waist of the tightly focused probe beam determines transverse ($x-$ and $y-$) dimensions of the ensemble. A bias magnetic field of 3.5 G is switched on and atoms are optically pumped to the $5s_{1/2}, F = 1, m_F = 0$ state. Probe Ω_p and control Ω_c laser fields are orthogonally circularly polarized. To avoid the dephasing of Rydberg state induced by inhomogeneous light shifts, the dipole trap is turned off before the Rydberg excitation field Ω_1 and switched back on after the Rydberg transfer field Ω_2.

6.2.3 Rydberg excitation and read-out

The 795 nm fields used for the two-photon Raman transition are derived from two home-made ECDLs locked to a low-expansion ultra stable reference cavity, see Figure 6.2.2. To reduce spontaneous emission from the intermediate state $|e\rangle = |5p_{1/2}, F = 1, m_F = -1\rangle$, two Raman beams are tuned off-resonance by a frequency offset $\delta_1/2\pi = -90$ MHz. The two Raman fields, probe and control, have peak powers of 60 pW and 130 nW, respectively. The 297 nm UV light is from the Fourth-harmonic generation (FHG) of power amplified 1188 nm ECDL light. The 1188 nm laser is also frequency-locked to the ultra-stable reference cavity, see Figure 6.2.2. The maximum power of 297 nm light on the atoms is about 20 mW. The reference cavity is temperature

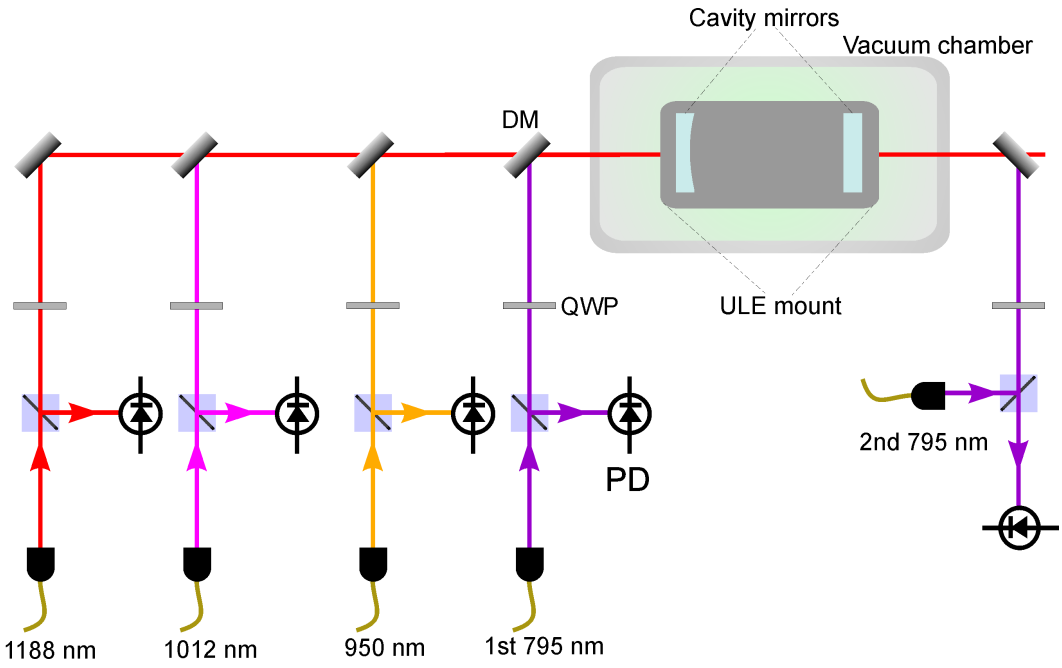

Figure 6.2.2: **Setup for frequency locking of multiple ECDLs to the reference cavity.** Laser fields at 1188 nm, 1012 nm, 950 nm, and 795 nm are mixed through Dichroic mirrors (DM) and sent to the reference cavity. The reflected beams are guided to photo-detectors (PD) for the PDH locking. Lights from the two 795 nm lasers are injected from opposite sides and are orthogonally and circularly polarized.

stabilized at the zero-crossing temperature to minimize the long-term drifts of laser frequencies. Part of the Second-harmonic generation (SHG) from the 1188 nm laser system is coupled into a wave-meter for measuring the frequency.

The frequencies of the 297 nm transitions to Rydberg p states are calculated using quantum defect values of Ref. [86]. Initial coarse tuning of the 297 nm laser frequency is done with a wave-meter. To find the $|5s_{1/2}, F = 2, m_F = -2\rangle \leftrightarrow |r = np_{3/2}, m_J = -3/2\rangle$ transition within a few MHz, the Rydberg single-photon depletion spectrum is measured. After the initial preparation of coherent excitations in state $|b\rangle$, we apply a 297 nm field Ω_1 to transfer atoms into the Rydberg state $|r\rangle$ and measure the residual populations in $|b\rangle$ state as a function of 297 nm laser frequency. Figure 6.2.3 shows a typical depletion spectrum measurement performed on the $|5s_{1/2}, F = 2, m_F = -2\rangle \leftrightarrow |29p_{3/2}, m_J = -3/2\rangle$ transition. The data are fit with

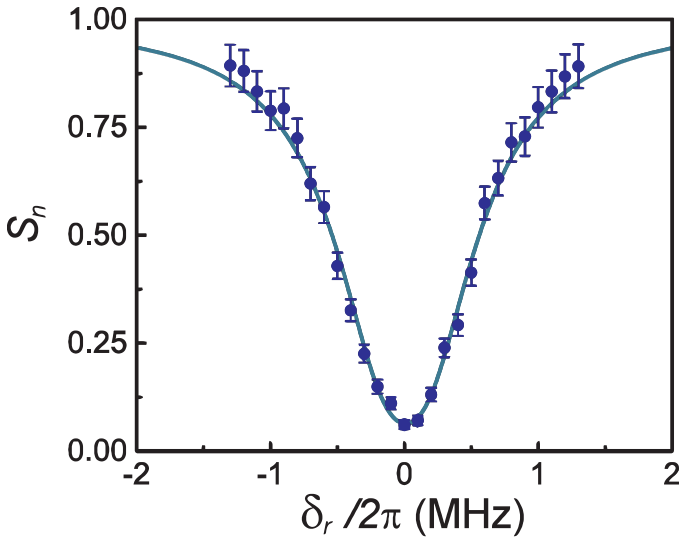

Figure 6.2.3: **Depletion spectrum for $|29p_{3/2}, m_J = -3/2\rangle$ state.** The normalized photoelectric detection rate S_n of retrieved field is shown as a function of detuning δ_r of UV field Ω_1.

an Exponential-Lorentzian profile $\exp(-\alpha/((2\delta_r/\gamma)^2+1))$, where $\alpha = 2.7(2)$ and $\gamma = 0.64(2)$ MHz are adjustable parameters.

In our experimental geometry, the Rydberg transfer field Ω_2 and read-out field Ω_r have the same wave vector $\mathbf{k}$ as the Rydberg excitation field Ω_1 and the control field Ω_c, respectively. As a result, the retrieved field is phase matched with the spatial mode of the probe field Ω_p, which is coupled into a single mode fiber and split by a 50/50 fiber beam-splitter for $g^{(2)}(\tau)$ measurement. To avoid damage to the single photon detectors from the probe field, an acousto-optic modulator (AOM) is used before the fiber coupler. The gating AOM is only turned on during the read-out process. A narrow band-pass filter centered at 795 nm is also used at fiber beamsplitter input port to block strong scattering from the MOT and dipole trap light. To minimize the background counting signal from single photon detectors, we use home-made switching electronics for fast gating of the photoelectric events.

In each experimental trial, photoelectric events from detectors D_1 and D_2 are recorded within a time interval of 200 ns, determined by the length of the retrieved pulse (Fig-

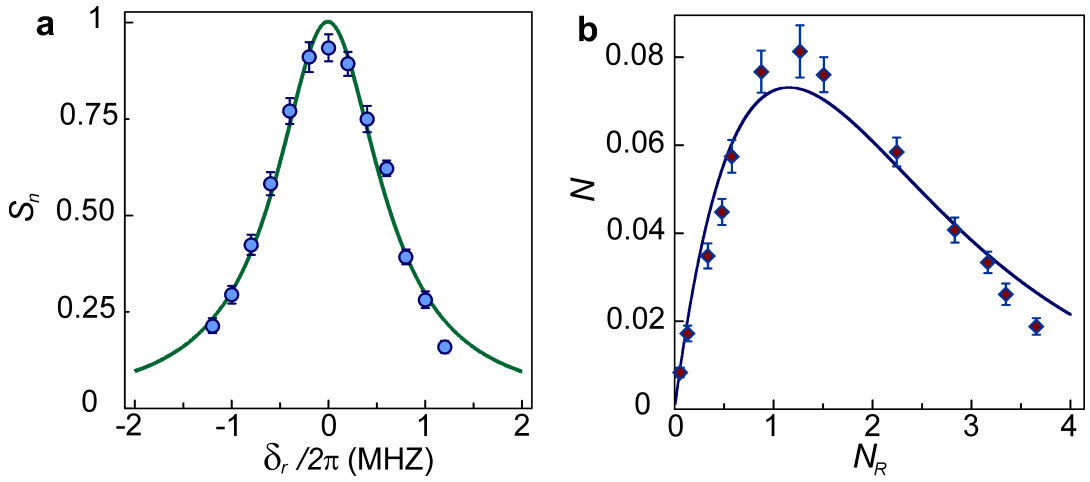

Figure 6.3.1: **Single-photon excitation to Rydberg p state.** **a**, Single-photon spectroscopy of $|b\rangle \leftrightarrow |r\rangle = |62p_{3/2}, m_J = -3/2\rangle$ transition. The normalized photoelectric detection rate S_n of the retrieved field is shown as a function of detuning (δ_r). The data are fit with a Lorentzian profile. **b**, N, the population of prepared single excitation (with Ω_1 and Ω_2 fields) is shown as a function of Raman excitation population N_R. Error bars, ± 1 standard deviations.

ure 6.2.1(b)). The photoelectric detection probability for both detectors is given by $P = P_1 + P_2 = N_1/N_0 + N_2/N_0$, where $N_{1,2}$ are the events recorded by D_1 and D_2, and N_0 is the number of experimental trails. The probability for detecting double coincidences is given by $P_{12}(\tau) = N_{12}(\tau)/N_0$, where $N_{12}(\tau)$ is the number of coincidences from the two detectors with time delay τ. The second order intensity correlation function is calculated as $g^{(2)}(\tau) = P_{12}(\tau)/(P_1 P_2)$.

6.3 Single-photon excitation to Rydberg p-state

Single-photon excitation from the ground state $|b\rangle$ to the Rydberg state $|r\rangle$ $(62p_{3/2})$ is studied in Figure 6.3.1. The normalized sum S_n of the D_1 and D_2 detection rates is shown in Figure 6.3.1 (a) as a function of single-photon detuning δ_r from the $|b\rangle \leftrightarrow |r\rangle$ resonance. The measured width (FWHM) of the spectrum $\gamma/2\pi = 1.3$ MHz is largely determined by the 0.7 μs duration of the excitation pulse Ω_1. The population of single

excitation prepared in $|b\rangle$, N (at $\delta_r = 0$) is shown in Figure 6.3.1 (b) as a function of Raman excitation population N_R in $|b\rangle$ (no coupling to the Rydberg state). N and N_R are obtained by normalizing the corresponding probabilities of photoelectric detection by the retrieval, transmission, and detection efficiencies. The data are fit with a function of

$$N = \zeta\chi N_R \exp(-\chi N_R), \tag{6.3.1}$$

where $\zeta = 0.20(1)$ and $\chi = 0.87(4)$ are adjustable parameters. The fit is suggested by the dephasing model of multi-particle Rydberg excitations from Ref. [101]. When the interactions are not sufficiently strong for the blockade to be operational over the entire ensemble, more than one Rydberg atom can be excited. Van der Waals interactions lead to the accumulation of phase shifts between different atomic pairs, decoupling them from the phase-matched collective emission mode of the read-out stage. Within the model, ζ corresponds to the population transfer efficiency of the $|b\rangle \rightarrow |r\rangle \rightarrow |b\rangle$ process in the absence of loss due to multi-particle dephasing, whereas the maximum single excitation preparation efficiency (including multi-particle dephasing loss) in state $|b\rangle$ is $\xi_m = \zeta/e$.

6.4 Coherence times and efficiencies

6.4.1 Coherence properties

The coherence properties of the ground-Rydberg transition are investigated in Figure 6.4.1 (a) by measuring the retrieved signal as a function of storage time T_r in state $|62p_{3/2}\rangle$. The data are fit with a Gaussian function $\exp(-(T_r + T_d)^2/{\tau_r}^2)$, while $T_d = 1$ μs is the delay between two 297 nm fields Ω_1 and Ω_2 for $T_r = 0$. The fast signal decay (with $1/e$ lifetime $\tau_r = 1.58(5)$ μs) is a result of the atomic motional dephasing. During the Rydberg excitation, a spin-wave with phase $e^{i\vec{k}_1\cdot\vec{r}}$ is imprinted

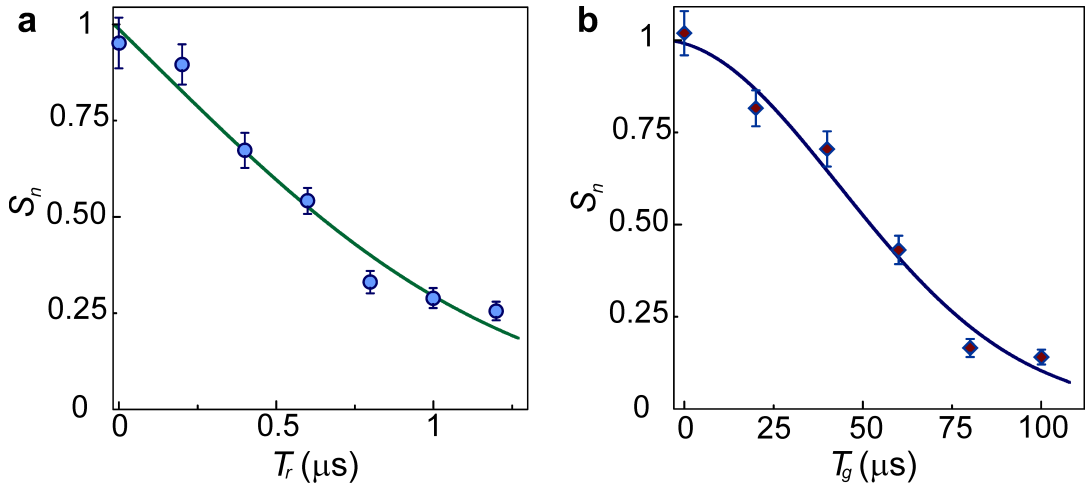

Figure 6.4.1: **Temporal dynamics of atomic polariton.** **a**, The normalized photoelectric detection rate S_n of the retrieved field is shown as a function of storage time T_r in the Rydberg state. **b**, The normalized photoelectric detection rate S_n of the retrieved field is shown as a function of storage time T_g in the ground states coherence. Error bars, ± 1 standard deviations.

on the ground-Rydberg coherence by the Ω_1 field, where $\vec{k}_1$ is the wave-vector of Ω_1, $\vec{r}$ is the atomic position, and the spin-wave period is $\Lambda_r = 2\pi/|\vec{k}_1| = 297$ nm. For a gas of atoms of mass M at a temperature T, atomic motion smears the spin-wave phase grating and leads to a $1/e$ decoherence time of $\tau_r = \Lambda_r/(2\pi\sqrt{k_B T/M})$ [16, 67], from which the inferred atom temperature is $T \simeq 10$ μK. A lower value of $T \simeq 7$ μK is measured from the thermal expansion of the cloud. The difference between the two is a possible indication of atomic heating by the repeated application of the memory protocol. The $\tau_r = 1.58(5)$ μs coherence time for the $|62p_{3/2}\rangle$ state is nearly identical to the $\tau_r = 1.58(2)$ μs found for the $|29p_{3/2}\rangle$ state (Figure 6.4.2), indicating the absence of Rydberg interaction-induced decoherence.

In order to achieve long storage time, we apply the Ω_2 field to coherently transfer the excitation from the Rydberg state $|r\rangle$ to the ground state $|b\rangle$, with the single-photon detuning $\delta_r = 0$. Due to the non-collinear geometry between the probe and control fields with respective wave-vectors $\vec{k}_p$ and $\vec{k}_c$, the atomic excitation forms a ground-states spin-wave, with phase $e^{i\Delta\vec{k}\cdot\vec{r}}$, where the wave-vector mismatch is $\Delta\vec{k} = \vec{k}_p - \vec{k}_c$,

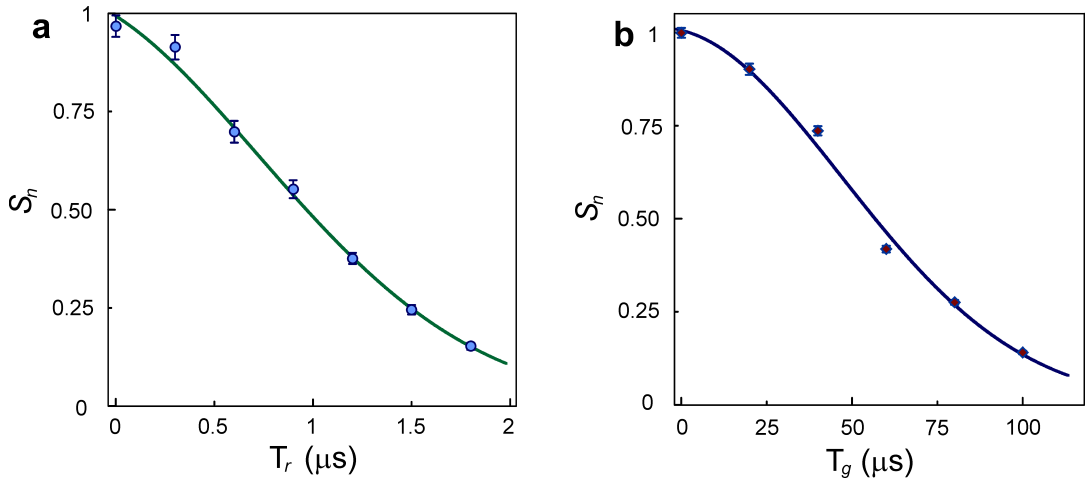

Figure 6.4.2: **Coherence time measurements.** **a**, Coherence time measurement for the $|29p_{3/2}, m_J = -3/2\rangle$ state. **b**, Coherence time measurement for ground states levels with Raman excitation.

and the spin-wave period is $\Lambda_g = 2\pi/|\Delta\vec{k}| = 15\ \mu$m. The stored excitations can be converted into a propagating field by applying a read-out field Ω_r.

To study the temporal dynamics of the quantum memory, the retrieved signal is measured as a function of the storage time T_g in the ground hyperfine sub-levels, as shown in Figure 6.4.1 (b). The data are fit with function $\exp(-(T_g + T_d)^2/{\tau_g}^2)$, where $T_d = 6\ \mu$s is the delay between the Raman excitation and the read-out for $T_g = 0$. The observed $1/e$ quantum memory lifetime is $\tau_g = 71(2)\ \mu$s, while the expected lifetime from the scaled value of the ground-Rydberg coherence is $\tau_r \times (\Lambda_g/\Lambda_r) \approx 80\ \mu$s. Assuming the difference in the two values is due to diffusion of atoms out of the ensemble in the transverse (x- and y-) dimensions, we estimate the transverse ensemble waist $(1/e^2)$ to be $\simeq 6(1)\ \mu$m, which agrees with the measured $5\ \mu$m waist of the probe field. In the future, the quantum memory lifetime can be extended into the minute range by employing a suitable state-insensitive optical lattice capable of atom confinement on a length scale smaller than the spin-wave period Λ_g [14, 41].

The Rydberg-ground coherence for $|29p_{3/2}, m_J = -3/2\rangle$ state is investigated in Figure 6.4.2 (a). The normalized photoelectric detection rate S_n of the retrieved field

is shown as a function of storage time T_r in the Rydberg state. A Gaussian function $\exp(-(T_r+T_d)^2/{\tau_r}^2)$ is used to fit the data, while $T_d = 0.4\ \mu s$ is the delay between two UV fields, Ω_1 and Ω_2, for $T_r = 0$. The coherence time $T_r = 1.58(2)\ \mu s$ is in agreement with the $1.58(5)\ \mu s$ measured coherence time for $|62p_{3/2}, m_J = -3/2\rangle$.

To study the coherence time of ground state levels, we perform Raman excitation and retrieve the stored photons without excitation to Rydberg states. The normalized photoelectric detection rate S_n of retrieved field is shown as a function of storage time T_g in the ground states coherence, Figure 6.4.2 (b). The data are fit with the function $\exp(-(T_g+T_d)^2/{\tau_g}^2)$, while $T_d = 6\ \mu s$ is the delay between Raman excitation and read-out for $T_g = 0$, and $\tau_g = 75(1)\ \mu s$.

6.4.2 Loss due to atomic diffusion

During the preparation of quantum memory, the Gaussian profile of the probe field Ω_p results in a spatial density distribution of excitations in the transverse directions (x- and y-). At zero delay between preparation and retrieval, the density distribution $n(x, T_g = 0)$ is

$$n(x, T_g = 0) = (\sqrt{2\pi{\sigma_0}^2})^{-1} \exp(-x^2/2{\sigma_0}^2), \tag{6.4.1}$$

where the cross-section radius $\sigma_0 = \omega_p/2$ and ω_p is the $1/e^2$ waist of the probe field. For an atomic cloud with temperature T, the atomic diffusion causes spatial broadening of $n(x)$ over time and leads to loss in retrievable excitations. The density distribution at a storage time T_g is given by

$$n(x, T_g) = (\sqrt{2\pi\sigma^2})^{-1} \exp(-x^2/2\sigma^2), \tag{6.4.2}$$

where $\sigma^2 = {\sigma_0}^2 + {\sigma_v}^2 {T_g}^2$, and $\sigma_v = \sqrt{k_B T/M} \sim 0.03\ \mu$m/$\mu$s. Considering the diffusion in x and y dimensions, the fraction of retrievable excitations at storage time T_g is given by

$$\begin{aligned} p(T_g) &= \frac{\int n(x,T_g)n(x,0)dx \int n(y,T_g)n(y,0)dy}{|\int n(x,0)dx \int n(y,0)dy|^2} \\ &= (1+\frac{1}{2}{\sigma_v}^2 {T_g}^2/{\sigma_0}^2)^{-1} \end{aligned} \tag{6.4.3}$$

To account for the difference between the measured 1/e lifetime of 71(2) μs in Figure 6.4.1 (b) and the expected value of 80 μs from spin-wave dephasing [67], we fit the data in Figure 6.4.1 (b) by combining spin-wave dephasing and diffusion loss and extract the cross-section radius $\sigma_0 = 3.0(5)\ \mu$m. So the $1/e^2$ transverse waist of our sample is $\omega = 2\sigma_0 = 6(1)\ \mu$m, which is in agreement with the 5 μm $1/e^2$ waist of the probe field measured with the knife edge methods. In future experiments, it is possible to compensate both motional dephasing and atomic diffusion loss by pining the spin-wave in an optical lattice [14].

6.4.3 Single quantum excitation preparation efficiency

The probability of photoelectric detection p is proportional to the single excitation preparation efficiency ξ : $p = \eta_r \eta_{td} \xi$. η_r is the efficiency of converting excitation in $|b\rangle$ into mode-matched photon field and can be extracted from $\eta_L = \eta_r \eta_s$. The overall efficiency of light storage η_L can obtained through the retrieved signal measurements and the storage efficiency η_s through the measurements of the transmitted fraction of probe field Ω_p. From the measured value of $\eta_L = 0.00069(2)$ and $\eta_s = 0.0111(2)$, we extract $\eta_r = 0.062(2)$. The photon transmission and detection efficiency η_{td} is given by $\eta_{td} = \eta_a \eta_f \eta_d = 0.24$, where $\eta_a = 0.75$, $\eta_f = 0.65$, and $\eta_d = 0.5$ are AOM diffraction efficiency, fiber coupling efficiency, and single photon detection efficiency,

respectively. As a result, the efficiency of preparing single quantum excitation in state $|b\rangle$ can be extracted from p :

$$\xi = p/(\eta_r \eta_{td}) = p \times 67(2). \tag{6.4.4}$$

With the measured value of $p = 0.12(1)\%$, we find $\xi \sim 8.1(6)\%$. The data shown in Figure 6.3.1 (b) are obtained in a similar way. N (N_R) are given by normalizing the measured values of p (p_R) by η_r and η_{td}, where p and p_R are the probabilities of photoelectric detection with and without optical coupling to the Rydberg state, respectively.

For the interaction-induced dephasing mechanism, the efficiency of preparing a retrievable single excitation is limited by $1/e$. By employing Rydberg levels of higher principal quantum number n and/or smaller ensemble volumes, transition into the regime of Rydberg excitation blockade can be achieved, with a corresponding increase in preparation efficiency ξ. The latter is also affected by the (motional) Rydberg-ground decoherence, which can be mitigated by adopting a state-insensitive trap for ground and Rydberg atoms.

6.5 Quantum statistics.

To characterize the non-classical behavior of our quantum memory, the atomic excitation is read out after a storage time of $T_g = 2$ μs, and a Hanbury Brown-Twiss measurement is performed on the retrieved field with a beamsplitter followed by two single-photon detectors D_1 and D_2. The photoelectric detection events at detectors D_1 and D_2 are cross-correlated, with the resulting second-order intensity correlation function $g^{(2)}(\tau)$ shown in Figure 6.5.1, where τ is the time delay between the detection events. Panel (a) shows the measurement for a coherent state created by the two

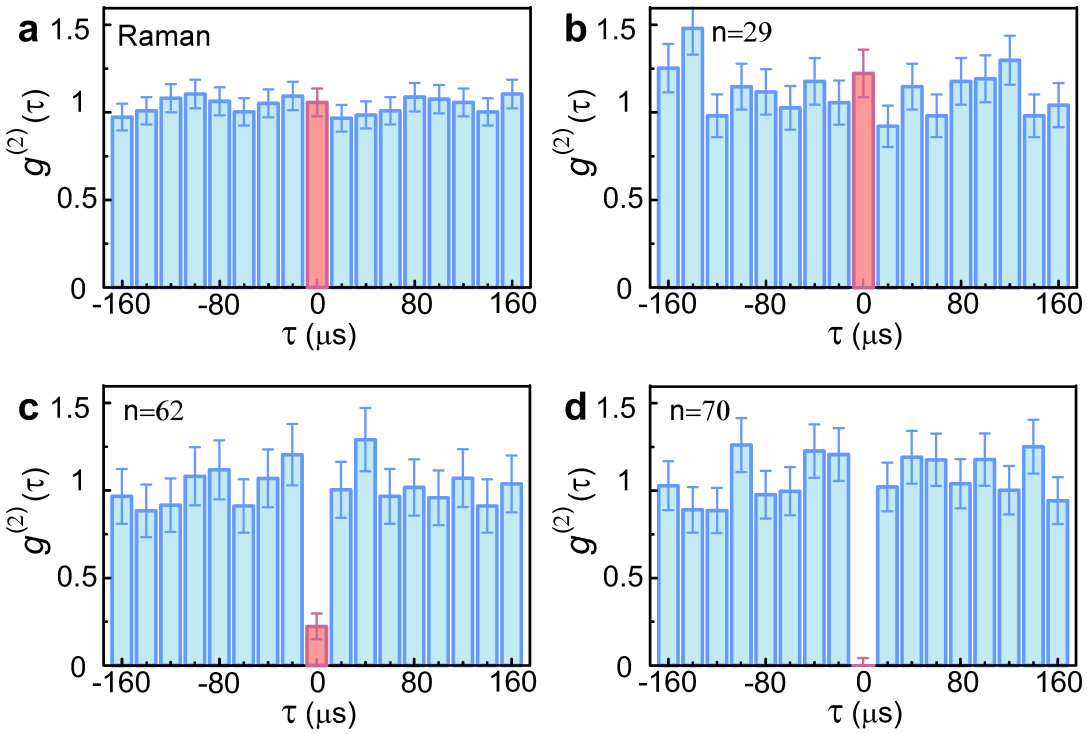

Figure 6.5.1: **Quantum statistics.** Measured second-order intensity correlation function $g^{(2)}$ as a function of delay τ. The data bins for $g^{(2)}(0)$ are highlighted. **a**, $g^{(2)}(\tau)$ is measured with retrieved coherent light created by the two Raman fields Ω_p and Ω_c. **b - d**, 297 nm fields (Ω_1 and Ω_2) couple state $|b\rangle$ to a Rydberg state $|np_{3/2}\rangle$, and $g^{(2)}(\tau)$ is measured at n = 29, 62, and 70, respectively. Error bars, ± 1 standard deviations.

Raman fields Ω_p and Ω_c. The measured second-order intensity correlation function at zero delay $g^{(2)}(0) = 1.06(8)$ is consistent with unity. Panels (b-d) show the quantum statistics of a memory coupled to Rydberg levels $np_{3/2}$, for $n = 29, 62$, and 70, respectively.

As a result of the chosen principal quantum numbers ($n \lesssim 70$) and sample size ($\sim$ 10 μm) in our experiment, interactions between the most distant Rydberg atom pairs are in the van der Waals regime, which scale as $\sim n^{11}$ [49]. For low values of n, the presence of multiple excitations is expected and the measured $g^{(2)}(0) = 1.22(14)$ for $n = 29$ is consistent with unity. The observed suppression of two-photon events at zero delay for high-lying Rydberg states $n = 62$ and 70 reflects Rydberg excitation blockade

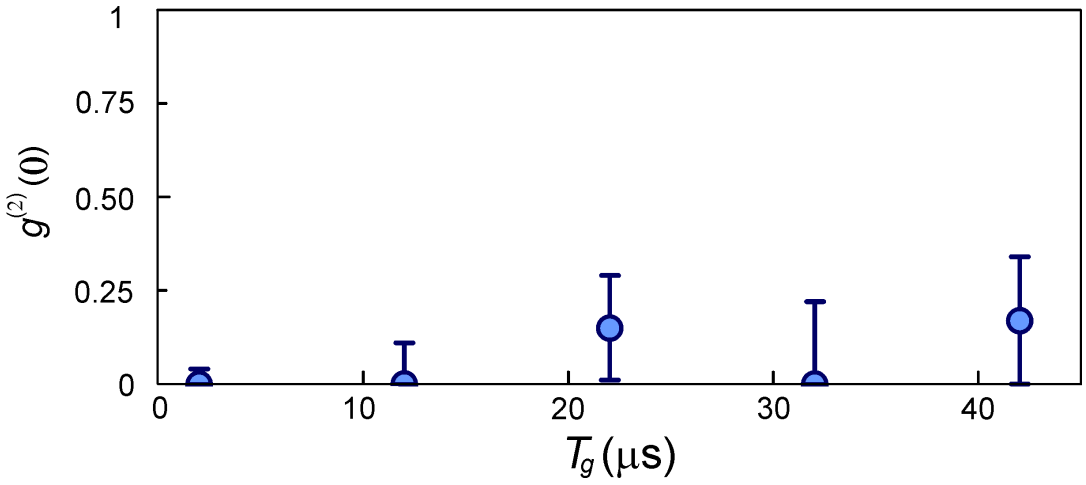

Figure 6.5.2: **Non-classical memory dynamics.** The single excitation generated with the $70p_{3/2}$ state is mapped onto the retrieved field after being stored in the ground states memory for a time T_g. The second-order intensity correlation function at zero delay $g^{(2)}(0)$ is measured at different storage times T_g. Error bars, ± 1 standard deviations.

and interaction-induced dephasing between multiple excitations and demonstrates the single-photon character of the retrieved field. The transition from the classical statistics to the manifestly quantum regime is associated with an approximately four orders of magnitude increase in the interaction strength from $n = 29$ to $n = 70$. The measured values of $g^{(2)}(0) = 0.22(8)$ for $n = 62$ and $g^{(2)}(0) = 0(0.04)$ for $n = 70$ confirm the preparation of single-quanta in the ground memory states. The quantum statistics of the retrieved light field as a function of storage time T_g are shown in Figure 6.5.2, with all the measured values for $g^{(2)}(0)$ well below unity for up to 42 μs-long storage.

6.6 Conclusion

In summary, we report the realization of a quantum memory with 8% efficiency to prepare a single excitation in less than one μs, and a memory lifetime of 70 μs. The storage times can be further extended, conceivably up to and beyond several seconds, by adopting a state-insensitive optical lattice [14, 41]. The results presented here

demonstrate that the two essential quantum network capabilities - fast quantum state generation and long-term storage - can be achieved at the same time in an atomic-ensemble-based system, opening a route toward a broad range of quantum information protocols.

Together with the recent advance in deterministic atom-photon entanglement [18], our results pave the way to long distance quantum communication with atomic-ensembles-based quantum repeater architectures [20–22]. A strongly interacting memory is also integral to the realization of global networks of atomic clocks for accurate international time keeping [23]. In particular, complex quantum states of atomic ensembles can be generated and stored in their ground states and subsequently converted into highly non-classical states of propagating light fields [50]. Such non-trivial photonic states are critical for quantum networks, linear optical quantum computing, and quantum metrology protocols beyond the standard quantum limit. Furthermore, our current protocol employs resonant optical coupling of long-lived ground state to high-lying Rydberg state, which can be extend to the off-resonant dressing regime and used to explore new physics in Rydberg-dressed many-body systems [56].

CHAPTER VII

Conclusion and outlook

In summary, we have presented our recent experiments on using cold atomic gases to study quantum optics. Long-lived quantum memory is a crucial component for realization of long distance distributed quantum systems. Ground states of cold atomic ensembles have excellent coherence properties and are promising candidates for quantum memory. By engineering a state-insensitive trap for the ground level coherence and applying dynamical decoupling sequences, we have realized a quantum memory for light, with a ultra-long lifetime on the time scale of a minute [14]. However, the weakly-interacting nature of the ground atomic levels only allows probabilistic protocols for quantum state preparation, while deterministic quantum protocols require controllable, strong, and long-range interactions. Atomic systems involving highly excited Rydberg states are excellent candidates for the study of many-body physics, quantum information science, and precision measurements. In this thesis, we have studied the novel quantum effects with strongly-interacting Rydberg atoms and their applications in quantum optics.

The strong interactions between Rydberg atoms give rise to an important phenomenon known as Rydberg excitation blockade, where the presence of one Rydberg atom prevents the rest of the nearby atoms from being promoted to Rydberg state. We have demonstrated Rydberg blockade in a mesoscopic ensemble containing a few hundred cold atoms. The many-body Rabi oscillations between the collective ground state

$|G\rangle$ and Rydberg super-atom state $|R\rangle$ is also observed with a collectively-enhanced Rabi frequency $\sqrt{N}\Omega$. The far-off-resonance optical fields that create conservative potentials for ground states are generally repulsive for Rydberg atoms. We have developed a state-insensitive optical lattice at 1004 or 1012 nm, which provides matched trapping potential for the ground and Rydberg states. With the spatial confinement provided by the magic trap, we also realized a single photon source with 5 kHz photon generation rate. It has been proposed that quantum networks of superior scaling can be achieved by using deterministic Rydberg-level interactions [20–23]. We have realized an essential element of Rydberg-atom-based quantum repeater architectures, the entanglement between light fields, and collective Rydberg excitations. To combine the strong interactions of Rydberg levels with the appealing coherence properties of the ground levels, we have employed UV laser fields at 297 nm for direct optical coupling of the ground state to Rydberg p-states. Our new system features both fast (sub-μs) quantum state generation and long-term quantum state preservation.

Important subjects for future studies include the realization of remote entanglement and quantum networks with Rydberg atoms. The idea of quantum networks has been at the center of quantum information science. However, the realization of a functional quantum network has so far remained an outstanding challenge. The preliminary quantum networks which used various physics implementations have had at most two nodes [112, 113, 115]. Alternatively, quantum networks with superior scaling properties could be achieved using entanglement between light fields and atoms in quantum superpositions of the ground and Rydberg states.

By performing two-photon excitation to high-lying Rydberg states in a small and dense sample, we demonstrated Rydberg excitation blockade for an ensemble containing a few hundred atoms. We have also generated deterministic entanglement between light and optical atomic transitions. The next step would be to generate remote entanglement between Rydberg super-atoms. The protocol is illustrated in Figure 7.0.1.

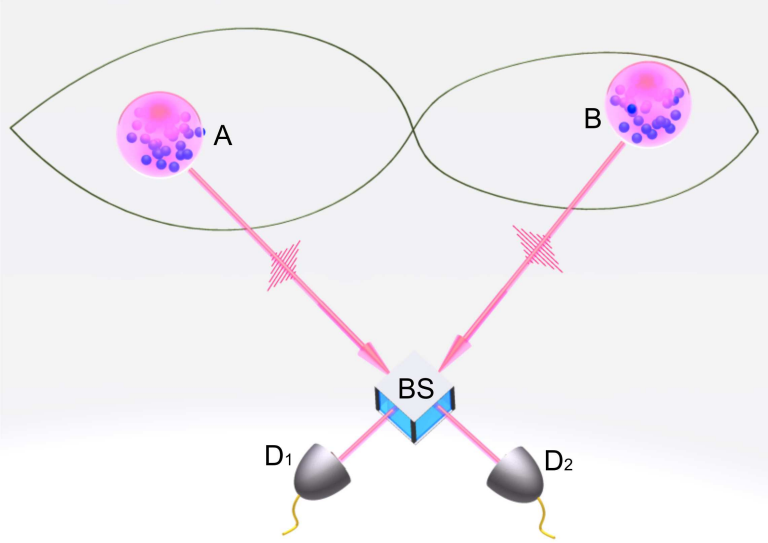

Figure 7.0.1: **Illustration for generating entanglement between remotely located Rydberg super-atoms.** Entangled atom-photon pairs are generated from two sites. The remote entanglement between two Rydberg super-atoms are established using measurement-induced entanglement with the photons from site A and B.

The entangled atom-photon pairs are created at sites A and B:

$$|R\rangle_A|0\rangle_A + |G\rangle_A|1\rangle_A,$$
$$|R\rangle_B|0\rangle_B + |G\rangle_B|1\rangle_B. \tag{7.0.1}$$

The photons from sites A and B are mixed at a beam-splitter (BS) and detected at single photon detectors D_1 and D_2. Due to the photon path indistinguishability, a photoelectric detection event at D_1 or D_2 heralds the establishment of entanglement between sites A and B:

$$|R\rangle_A|G\rangle_B + |G\rangle_A|R\rangle_B. \tag{7.0.2}$$

The entangled state (7.0.2) can be confirmed by driving many-body Rabi oscilla-

tions to rotate the super-atom qubits at two sites. Most of the measurement induced entanglement protocols are conditioned on the detection of coincidence on the two detectors. As a result, the efficiency for remote entanglement generation $\propto p^2$, where p is the efficiency of preparing atom-photon entanglement. The p^2 scaling puts limit on entanglement generation rate, making it challenging to establish a quantum network with more than two nodes. The entanglement protocol shown in Figure 7.0.1 is heralded on the single photon detection events instead of coincidences. This protocol has the potential to allow much higher entanglement rate, given that the remote entanglement rate $\propto p$ rather than p^2. The atom-photon entanglement rate could be on the order of kHz [18].

Quantum networks require the efficient conversion between matter and light. Currently, the efficiency of mapping atomic excitations into phase-matched mode of light is $\eta \sim 0.6$ for ground states and $\eta \sim 0.2$ for Rydberg states, limited by the optical depth of the sample. In future experiments, $\eta \sim 1$ can be achieved with the enhancement from an optical cavity.

Rydberg states are promising for deterministic quantum states generation and efficient quantum operations. One limitation on the quantum state preparation efficiency ($\sim 0.67(10)$) is the motional decoherence of Rydberg excitations due to short spin-wave period (~ 300 nm for single-photon excitation and ~ 1 μm for two-photon excitation). In the future, using the state-insensitive trapping techniques developed in this thesis, it should be possible to freeze the atomic motion along the direction of the spin-wave and achieve ground-Rydberg coherence time on the order of ~ 10 μs, which would allow near unity quantum state creation and more complicated quantum operations. However, it is still challenging to achieve the long storage times needed for long distance quantum networks using only Rydberg states. On the other hand, the weakly-interacting ground states offer much better coherence properties. We have realized a quantum memory with lifetime on the time scale of a minute using the magic trapping

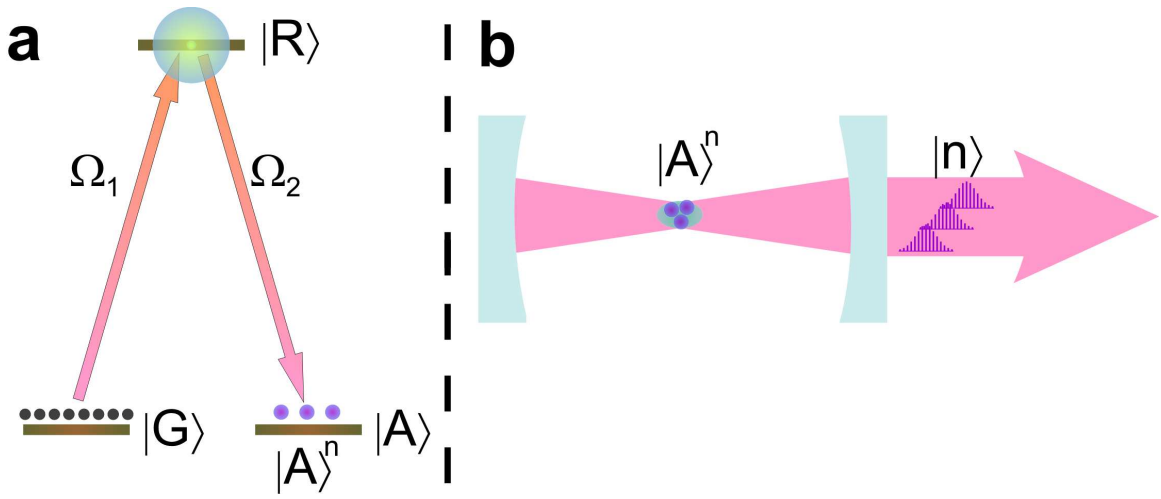

Figure 7.0.2: **Protocol for generating atomic and photonic Fock states. a**. Excitations in ground state $|A\rangle$ can be added by repeating the Ω_1 and Ω_2 fields for the generation and transfer of single excitation. **b**. The prepared atomic Fock state $|A\rangle^n$ can be efficiently mapped into photonic number state $|n\rangle$ with an optical cavity.

techniques and dynamic decoupling sequences. By using single-photon excitation to Rydberg states, a quantum memory that combines the dual capabilities of fast quantum state generation and long-term storage can be realized. Together, the experiments demonstrated in this thesis have realized some of the essential elements for quantum networks with superior scaling properties.

Atomic and photonic Fock states generation with Rydberg atoms. Creating number states (Fock states) is a long-standing goal in physics. In Ref. [50], it is proposed that arbitrary atomic state can be engineered by employing Rydberg levels for interactions and ground atomic levels for storage. Coherent transfer from Rydberg to ground state allows for better quantum state preservation, as the large electric dipole transition elements between Rydberg states lead to relatively short lifetimes with respect to spontaneous emission, black-body radiation, and ambient electric fields [49]. Furthermore, when created in proper phase-matching configurations, the synthesized atomic state shows a collectively enhanced coupling to light and thus can be transferred to a single-mode photon field through a collective emission process [35]. Non-classical

photonic states can be effectively generated with the integration of high finesse optical cavities [50].

Our recent experiment with single-photon excitation to Rydberg states has the essential elements for such a protocol, as shoen in Figure 7.0.2. With improved performances, complex quantum states, such as atomic Fock states, can be generated. By driving many-body Rabi oscillation between the collective ground ($|G\rangle$) and Rydberg ($|R\rangle$) states with Ω_1 field, single Rydberg excitation can be created and subsequently transferred to a different ground state $|A\rangle$ for storage by applying a π pulse with Ω_2 field. The repetition of such sequence creates atomic Fock states $|A\rangle^n$. The maximum achievable value of n is limited by the efficiency ζ of the $|G\rangle \rightarrow |R\rangle \rightarrow |A\rangle$ process, as the efficiency of preparing $|A\rangle^n$ is proportional to ζ^n. ζ can be improved with proper adiabatic rapid passage (ARP) pulses [125]. Photonic Fock state $|n\rangle$ can be created by converting atomic state $|A\rangle^n$ into mode-matched light field. By integrating atomic ensemble with a low- to medium-finesse optical cavity (Figure 7.0.2 (b)), the matter-light conversion efficiency η can be close to unity, allowing the preparation of large and complex photonic states.

Bibliography

[1] C. K. Kao, "Nobel lecture: Sand from centuries past: Send future voices fast," *Rev. Mod. Phys.*, vol. 82, no. 3, p. 2299, 2010.

[2] I. Akasaki, "Nobel lecture: Fascinated journeys into blue light," *Rev. Mod. Phys.*, vol. 87, no. 4, p. 1119, 2015.

[3] H. Amano, "Nobel lecture: Growth of gan on sapphire via low-temperature deposited buffer layer and realization of p-type gan by mg doping followed by low-energy electron beam irradiation," *Rev. Mod. Phys.*, vol. 87, no. 4, p. 1133, 2015.

[4] S. Nakamura, "Nobel lecture: Background story of the invention of efficient blue ingan light emitting diodes," *Rev. Mod. Phys.*, vol. 87, no. 4, p. 1139, 2015.

[5] M. Planck, "Ueber das gesetz der energieverteilung im normalspectrum," *Ann. Phys. (Berlin)*, vol. 309, no. 3, pp. 553–563, 1901.

[6] A. Einstein, "Über einen die erzeugung und verwandlung des lichtes betreffenden heuristischen gesichtspunkt," *Ann. Phys. (Berlin)*, vol. 322, no. 6, pp. 132–148, 1905.

[7] J.-W. Pan, Z.-B. Chen, C.-Y. Lu, H. Weinfurter, A. Zeilinger, and M. Żukowski, "Multiphoton entanglement and interferometry," *Rev. Mod. Phys.*, vol. 84, no. 2, p. 777, 2012.

[8] Z. Ou and L. Mandel, "Violation of bell's inequality and classical probability in a two-photon correlation experiment," *Phys. Rev. Lett.*, vol. 61, no. 1, p. 50, 1988.

[9] D. Bouwmeester, J.-W. Pan, K. Mattle, M. Eibl, H. Weinfurter, and A. Zeilinger, "Experimental quantum teleportation," *Nature*, vol. 390, no. 6660, pp. 575–579, 1997.

[10] J.-W. Zhou, P.-F. Wang, F.-Z. Shi, P. Huang, X. Kong, X.-K. Xu, Q. Zhang, Z.-X. Wang, X. Rong, and J.-F. Du, "Quantum information processing and metrology with color centers in diamonds," *Front. Phys.*, vol. 9, no. 5, pp. 587–597, 2014.

[11] F. A. Zwanenburg, A. S. Dzurak, A. Morello, M. Y. Simmons, L. C. Hollenberg, G. Klimeck, S. Rogge, S. N. Coppersmith, and M. A. Eriksson, "Silicon quantum electronics," *Rev. Mod. Phys.*, vol. 85, no. 3, p. 961, 2013.

[12] M. H. Devoret and R. J. Schoelkopf, "Superconducting circuits for quantum information: an outlook," *Science*, vol. 339, no. 6124, pp. 1169–1174, 2013.

[13] Z.-L. Xiang, S. Ashhab, J. You, and F. Nori, "Hybrid quantum circuits: Superconducting circuits interacting with other quantum systems," *Rev. Mod. Phys.*, vol. 85, no. 2, p. 623, 2013.

[14] Y. Dudin, L. Li, and A. Kuzmich, "Light storage on the time scale of a minute," *Phys. Rev. A*, vol. 87, no. 3, p. 031801, 2013.

[15] L.-M. Duan, M. Lukin, J. I. Cirac, and P. Zoller, "Long-distance quantum communication with atomic ensembles and linear optics," *Nature*, vol. 414, pp. 413–418, 2001.

[16] R. Zhao, Y. O. Dudin, S. D. Jenkins, C. J. Campbell, D. N. Matsukevich, T. A. B. Kennedy, and A. Kuzmich, "Long-lived quantum memory," *Nature Phys.*, vol. 5, p. 100, 2009.

[17] Y. Dudin, L. Li, F. Bariani, and A. Kuzmich, "Observation of coherent many-body rabi oscillations," *Nature Phys.*, vol. 8, no. 11, pp. 790–794, 2012.

[18] L. Li, Y. Dudin, and A. Kuzmich, "Entanglement between light and an optical atomic excitation," *Nature*, vol. 498, no. 7455, pp. 466–469, 2013.

[19] L. Li and A. Kuzmich, "Quantum memory with strong and controllable rydberg-level interactions," *Nature Commun. in press*, 2016.

[20] B. Zhao, M. Müller, K. Hammerer, and P. Zoller, "Efficient quantum repeater based on deterministic rydberg gates," *Phys. Rev. A*, vol. 81, no. 5, p. 052329, 2010.

[21] E. Brion, F. Carlier, V. Akulin, and K. Mølmer, "Quantum repeater with rydberg-blocked atomic ensembles in fiber-coupled cavities," *Phys. Rev. A*, vol. 85, no. 4, p. 042324, 2012.

[22] Y. Han, B. He, K. Heshami, C.-Z. Li, and C. Simon, "Quantum repeaters based on rydberg-blockade-coupled atomic ensembles," *Phys. Rev. A*, vol. 81, no. 5, p. 052311, 2010.

[23] P. Kómár, T. Topcu, E. Kessler, A. Derevianko, V. Vuletić, J. Ye, and M. Lukin, "Quantum network of neutral atom clocks," *arXiv preprint arXiv:1603.06258*, 2016.

[24] L. Marrucci, E. Karimi, S. Slussarenko, B. Piccirillo, E. Santamato, E. Nagali, and F. Sciarrino, "Spin-to-orbital conversion of the angular momentum of light and its classical and quantum applications," *Journal of Optics*, vol. 13, no. 6, p. 064001, 2011.

[25] C. Bennett, "Quantum cryptography: Public key distribution and coin tossing," in *Proc. of IEEE Int. Conf. on Computers, Systems and Signal Processing, 1984*, 1984.

[26] E. Knill, R. Laflamme, and G. J. Milburn, "A scheme for efficient quantum computation with linear optics," *Nature*, vol. 409, no. 6816, pp. 46–52, 2001.

[27] V. Giovannetti, S. Lloyd, and L. Maccone, "Advances in quantum metrology," *Nature Photon.*, vol. 5, no. 4, pp. 222–229, 2011.

[28] R. H. Brown and R. Twiss, "A test of a new type of stellar interferometer on sirius," *Nature*, vol. 178, no. 4541, pp. 1046–1048, 1956.

[29] R. H. Brown and R. Twiss, "The question of correlation between photons in coherent light rays," *Nature*, vol. 178, no. 4548, pp. 1447–1448, 1956.

[30] R. P. Feynman, "Simulating physics with computers," *Int. J. Theor. Phys.*, vol. 21, no. 6, pp. 467–488, 1982.

[31] I. Bloch, J. Dalibard, and S. Nascimbène, "Quantum simulations with ultracold quantum gases," *Nature Phys.*, vol. 8, no. 4, pp. 267–276, 2012.

[32] D. Durfee, Y. Shaham, and M. Kasevich, "Long-term stability of an area-reversible atom-interferometer sagnac gyroscope," *Phys. Rev. Lett.*, vol. 97, no. 24, p. 240801, 2006.

[33] M. Hohensee, S.-Y. Lan, R. Houtz, C. Chan, B. Estey, G. Kim, P.-C. Kuan, and H. Müller, "Sources and technology for an atomic gravitational wave interferometric sensor," *General Relativity and Gravitation*, vol. 43, no. 7, pp. 1905–1930, 2011.

[34] A. D. Ludlow, M. M. Boyd, J. Ye, E. Peik, and P. O. Schmidt, "Optical atomic clocks," *Rev. Mod. Phys.*, vol. 87, no. 2, p. 637, 2015.

[35] M. Fleischhauer and M. D. Lukin, "Dark-state polaritons in electromagnetically induced transparency," *Phys. Rev. Lett.*, vol. 84, pp. 5094–5097, 2000.

[36] D. N. Matsukevich, T. Chanelière, S. D. Jenkins, S.-Y. Lan, T. A. B. Kennedy, and A. Kuzmich, "Deterministic single photons via conditional quantum evolution," *Phys. Rev. Lett.*, vol. 97, p. 013601, 2006.

[37] Y. O. Dudin and A. Kuzmich, "Strongly interacting rydberg excitations of a cold atomic gas," *Science*, vol. 336, p. 887, 2012.

[38] D. N. Matsukevich and A. Kuzmich, "Quantum state transfer between matter and light," *Science*, vol. 306, pp. 663–666, 2004.

[39] Y.-A. Chen *et al.*, "Memory-built-in quantum teleportation with photonic and atomic qubits," *Nature Phys.*, vol. 4, p. 103, 2008.

[40] J. Simon, H. Tanji, S. Ghosh, and V. Vuletić, "Single-photon bus connecting spin-wave quantum memories," *Nature Phys.*, vol. 3, p. 765, 2007.

[41] A. G. Radnaev, Y. O. Dudin, R. Zhao, H. H. Jen, S. D. Jenkins, A. Kuzmich, and T. A. B. Kennedy, "A quantum memory with telecom-wavelength conversion," *Nature Phys.*, vol. 6, p. 894, 2010.

[42] Y. O. Dudin, A. G. Radnaev, R. Zhao, J. Z. Blumoff, T. A. B. Kennedy, and A. Kuzmich, "Entanglement of light-shift compensated atomic spin waves with telecom light," *Phys. Rev. Lett.*, vol. 105, p. 260502, 2010.

[43] K. M. Beck, M. Hosseini, Y. Duan, and V. Vuletić, "Large conditional single-photon cross-phase modulation," *arXiv preprint arXiv:1512.02166*, 2015.

[44] D. Tiarks, S. Schmidt, G. Rempe, and S. Dürr, "Optical π phase shift created with a single-photon pulse," *Sci. Adv.*, vol. 2, p. e1600036, 2016.

[45] M. Khazali, K. Heshami, and C. Simon, "Photon-photon gate via the interaction between two collective rydberg excitations," *Phys. Rev. A*, vol. 91, no. 3, p. 030301, 2015.

[46] A. Reiserer and G. Rempe, "Cavity-based quantum networks with single atoms and optical photons," *Rev. Mod. Phys.*, vol. 87, no. 4, p. 1379, 2015.

[47] O. Mandel, M. Greiner, A. Widera, T. Rom, T. W. Hänsch, and I. Bloch, "Controlled collisions for multi-particle entanglement of optically trapped atoms," *Nature*, vol. 425, no. 6961, pp. 937–940, 2003.

[48] A. Kaufman, B. Lester, M. Foss-Feig, M. Wall, A. Rey, and C. Regal, "Entangling two transportable neutral atoms via local spin exchange," *Nature*, vol. 527, no. 7577, pp. 208–211, 2015.

[49] M. Saffman, T. G. Walker, and K. Molmer, "Quantum information with rydberg atoms," *Rev. Mod. Phys.*, vol. 82, no. 3, pp. 2313–2363, 2010.

[50] M. Lukin, M. Fleischhauer, R. Cote, L. Duan, D. Jaksch, J. Cirac, and P. Zoller, "Dipole blockade and quantum information processing in mesoscopic atomic ensembles," *Phys. Rev. Lett.*, vol. 87, no. 3, p. 037901, 2001.

[51] T. F. Gallagher, *Rydberg atoms*. Cambridge University Press, Cambridge, 1994.

[52] E. Urban, T. A. Johnson, T. Henage, L. Isenhower, D. D. Yavuz, T. G. Walker, and M. Saffman, "Observation of Rydberg blockade between two atoms," *Nature Phys.*, vol. 5, no. 2, pp. 110–114, 2009.

[53] A. Gaëtan, Y. Miroshnychenko, T. Wilk, A. Chotia, M. Viteau, D. Comparat, P. Pillet, A. Browaeys, and P. Grangier, "Observation of collective excitation of two individual atoms in the Rydberg blockade regime," *Nature Phys.*, vol. 5, no. 2, pp. 115–118, 2009.

[54] Y.-Y. Jau, A. Hankin, T. Keating, I. Deutsch, and G. Biedermann, "Entangling atomic spins with a rydberg-dressed spin-flip blockade," *Nature Phys.*, vol. 12, no. 1, pp. 71–74, 2016.

[55] P. Schauß, J. Zeiher, T. Fukuhara, S. Hild, M. Cheneau, T. Macrì, T. Pohl, I. Bloch, and C. Gross, "Crystallization in ising quantum magnets," *Science*, vol. 347, no. 6229, pp. 1455–1458, 2015.

[56] J. Zeiher, R. van Bijnen, P. Schauß, S. Hild, J.-y. Choi, T. Pohl, I. Bloch, and C. Gross, "Many-body interferometry of a rydberg-dressed spin lattice," *arXiv preprint arXiv:1602.06313*, 2016.

[57] D. Maxwell, D. Szwer, D. Paredes-Barato, H. Busche, J. Pritchard, A. Gauguet, K. Weatherill, M. Jones, and C. Adams, "Storage and control of optical photons using rydberg polaritons," *Phys. Rev. Lett.*, vol. 110, no. 10, p. 103001, 2013.

[58] S. Baur, D. Tiarks, G. Rempe, and S. Dürr, "Single-photon switch based on rydberg blockade," *Phys. Rev. Lett.*, vol. 112, no. 7, p. 073901, 2014.

[59] M. Ebert, A. Gill, M. Gibbons, X. Zhang, M. Saffman, and T. G. Walker, "Atomic fock state preparation using rydberg blockade," *Phys. Rev. Lett.*, vol. 112, no. 4, p. 043602, 2014.

[60] D. Barredo, S. Ravets, H. Labuhn, L. Béguin, A. Vernier, F. Nogrette, T. Lahaye, and A. Browaeys, "Demonstration of a strong rydberg blockade in three-atom systems with anisotropic interactions," *Phys. Rev. Lett.*, vol. 112, no. 18, p. 183002, 2014.

[61] J. Zeiher, P. Schauß, S. Hild, T. Macrì, I. Bloch, and C. Gross, "Microscopic characterization of scalable coherent rydberg superatoms," *Phys. Rev. X*, vol. 5, no. 3, p. 031015, 2015.

[62] T. Peyronel, O. Firstenberg, Q.-Y. Liang, S. Hofferberth, A. V. Gorshkov, T. Pohl, M. D. Lukin, and V. Vuletić, "Quantum nonlinear optics with single photons enabled by strongly interacting atoms," *Nature*, vol. 488, no. 7409, pp. 57–60, 2012.

[63] O. Firstenberg, T. Peyronel, Q.-Y. Liang, A. V. Gorshkov, M. D. Lukin, and V. Vuletić, "Attractive photons in a quantum nonlinear medium," *Nature*, vol. 502, no. 7469, pp. 71–75, 2013.

[64] D. Tiarks, S. Baur, K. Schneider, S. Dürr, and G. Rempe, "Single-photon transistor using a förster resonance," *Phys. Rev. Lett.*, vol. 113, no. 5, p. 053602, 2014.

[65] H. Gorniaczyk, C. Tresp, J. Schmidt, H. Fedder, and S. Hofferberth, "Single-photon transistor mediated by interstate rydberg interactions," *Phys. Rev. Lett.*, vol. 113, no. 5, p. 053601, 2014.

[66] M. Saffman and T. Walker, "Creating single-atom and single-photon sources from entangled atomic ensembles," *Phys. Rev. A*, vol. 66, p. 065403, 2002.

[67] P. R. Berman and V. S. Malinovsky, *Principles of laser spectroscopy and quantum optics*. Princeton University Press, 2010.

[68] M. D. Lukin, "Colloquium: Trapping and manipulating photon states in atomic ensembles," *Rev. Mod. Phys.*, vol. 75, pp. 457–472, 2003.

[69] S. Kuhr, W. Alt, D. Schrader, I. Dotsenko, Y. Miroshnychenko, A. Rauschenbeutel, and D. Meschede, "Analysis of dephasing mechanisms in a standing-wave dipole trap," *Phys. Rev. A*, vol. 72, p. 023406, 2005.

[70] S. Kuppens, K. Corwin, K. Miller, T. Chupp, and C. Wieman, "Loading an optical dipole trap," *Phys. Rev. A*, vol. 62, p. 013406, 2000.

[71] Y. O. Dudin, R. Zhao, T. A. B. Kennedy, and A. Kuzmich, "Light storage in a magnetically dressed optical lattice," *Phys. Rev. A*, vol. 103, p. 020505, 2009.

[72] A. Derevianko, "Theory of magic optical traps for Zeeman-insensitive clock transitions in alkali-metal atoms," *Phys. Rev. A*, vol. 81, p. 051606, 2010.

[73] E. L. Hahn, "Spin echoes," *Phys. Rev.*, vol. 80, no. 4, p. 580, 1950.

[74] L. Viola and S. Lloyd, "Dynamical suppression of decoherence in two-state quantum systems," *Phys. Rev. A*, vol. 58, no. 4, pp. 733–2744, 1998.

[75] M. J. Biercuk, H. Uys, A. P. VanDevender, N. Shiga, W. M. Itano, and J. J. Bollinger, "Optimized dynamical decoupling in a model quantum memory," *Nature*, vol. 458, no. 7241, pp. 996–1000, 2009.

[76] Y. Sagi, I. Almog, and N. Davidson, "Process tomography of dynamical decoupling in a dense cold atomic ensemble," *Phys. Rev. Lett.*, vol. 105, p. 053201, 2010.

[77] L. Vandersypen and I. Chuang, "Nmr techniques for quantum control and computation," *Rev. Mod. Phys.*, vol. 76, no. 4, pp. 1037–1069, 2004.

[78] D. J. Szwer, S. C. Webster, A. M. Steane, and D. M. Lucas, "Keeping a single qubit alive by experimental dynamic decoupling," *J. Phys. B*, vol. 44, no. 2, p. 025501, 2010.

[79] A. Ajoy, G. A. Álvarez, and D. Suter, "Optimal pulse spacing for dynamical decoupling in the presence of a purely dephasing spin bath," *Phys. Rev. A*, vol. 83, no. 3, p. 032303, 2011.

[80] J. Bylander, S. Gustavsson, F. Yan, F. Yoshihara, K. Harrabi, G. Fitch, D. G. Cory, Y. Nakamura, J.-S. Tsai, and W. D. Oliver, "Noise spectroscopy through dynamical decoupling with a superconducting flux qubit," *Nature Phys.*, vol. 7, no. 7, pp. 565–570, 2011.

[81] S. Meiboom and D. Gill, "Modified spin-echo method for measuring nuclear relaxation times," *Rev. Sci. Instr.*, vol. 29, no. 8, pp. 688–691, 1958.

[82] D. J. Griffiths, *Introduction to quantum mechanics*. Pearson Prentice Hall, 2005.

[83] I. Rabi, S. Millman, P. Kusch, and J. Zacharias, "The molecular beam resonance method for measuring nuclear magnetic moments," *Phys. Rev.*, vol. 55, no. 6, pp. 0526–0535, 1939.

[84] R. H. Dicke, "Interaction-free quantum measurements: A paradox?," *Am. J. Phys.*, vol. 49, no. 10, pp. 925–930, 1981.

[85] F. Cummings and A. Dorri, "Exact solution for spontaneous emission in the presence of n atoms," *Phys. Rev. A*, vol. 28, no. 4, p. 2282, 1983.

[86] W. Li, I. Mourachko, M. Noel, and T. Gallagher, "Millimeter-wave spectroscopy of cold Rb Rydberg atoms in a magneto-optical trap: Quantum defects of the ns, np, and nd series," *Phys. Rev. A*, vol. 67, p. 052502, 2003.

[87] J. Han, Y. Jamil, D. Norum, P. J. Tanner, and T. Gallagher, "Rb n f quantum defects from millimeter-wave spectroscopy of cold rb 85 rydberg atoms," *Phys. Rev. A*, vol. 74, no. 5, p. 054502, 2006.

[88] M. Mack, F. Karlewski, H. Hattermann, S. Höckh, F. Jessen, D. Cano, and J. Fortágh, "Measurement of absolute transition frequencies of rb 87 to ns and nd rydberg states by means of electromagnetically induced transparency," *Phys. Rev. A*, vol. 83, no. 5, p. 052515, 2011.

[89] N. Ramsey, *Molecular Beams*. Clarendon Press, Oxford, 1985.

[90] L. Allen and J. H. Eberly, *Two-level atoms and optical resonance*. Dover Publications, Mineola, 1987.

[91] J. Stanojevic and R. Côté, "Many-body rabi oscillations of rydberg excitation in small mesoscopic samples," *Phys. Rev. A*, vol. 80, no. 3, p. 033418, 2009.

[92] F. Cummings and A. Dorri, "Exact solution for spontaneous emission in the presence of N atoms," *Phys. Rev. A*, vol. 28, no. 4, pp. 2282–2285, 1983.

[93] M. Viteau, M. G. Bason, J. Radogostowicz, N. Malossi, D. Ciampini, O. Morsch, and E. Arimondo, "Rydberg excitations in bose-einstein condensates in quasi-one-dimensional potentials and optical lattices," *Phys. Rev. Lett.*, vol. 107, no. 6, p. 060402, 2011.

[94] K. Singer, M. Reetz-Lamour, T. Amthor, L. Marcassa, and M. Weidemuller, "Suppression of excitation and spectral broadening induced by interactions in a cold gas of Rydberg atoms," *Phys. Rev. Lett*, vol. 93, p. 163001, 2004.

[95] T. Vogt, M. Viteau, J. Zhao, A. Chotia, D. Comparat, and P. Pillet, "Dipole blockade at forster resonances in high resolution laser excitation of Rydberg states of cesium atoms," *Phys. Rev. Lett.*, vol. 97, p. 083003, 2006.

[96] D. Tong, S. Farooqi, J. Stanojevic, S. Krishnan, Y. Zhang, R. Cote, E. Eyler, and P. Gould, "Local blockade of Rydberg excitation in an ultracold gas," *Phys. Rev. Lett.*, vol. 93, p. 063001, 2004.

[97] T. Liebisch, A. Reinhard, P. Berman, and G. Raithel, "Atom counting statistics in ensembles of interacting Rydberg atoms," *Phys. Rev. Lett.*, vol. 95, p. 253002, 2005.

[98] R. Heidemann, U. Raitzsch, V. Bendkowsky, B. Butscher, R. Loew, L. Santos, and T. Pfau, "Evidence for coherent collective Rydberg excitation in the strong blockade regime," *Phys. Rev. Lett.*, vol. 99, p. 163601, 2007.

[99] M. Reetz-Lamour, T. Amthor, J. Deiglmayr, and M. Weidemüller, "Rabi oscillations and excitation trapping in the coherent excitation of a mesoscopic frozen rydberg gas," *Phys. Rev. Lett.*, vol. 100, no. 25, p. 253001, 2008.

[100] T. A. Johnson, E. Urban, T. Henage, L. Isenhower, D. Yavuz, T. Walker, and M. Saffman, "Rabi oscillations between ground and rydberg states with dipole-dipole atomic interactions," *Phys. Rev. Lett.*, vol. 100, no. 11, p. 113003, 2008.

[101] F. Bariani, Y. O. Dudin, T. A. B. Kennedy, and A. Kuzmich, "Dephasing of Multiparticle Rydberg Excitations for Fast Entanglement Generation," *Phys. Rev. Lett.*, vol. 108, p. 030501, 2012.

[102] F. Bariani and T. A. B. Kennedy, "Retrieval of multiple spin waves from a weakly excited, metastable atomic ensemble," *Phys. Rev. A*, vol. 85, p. 033811, 2012.

[103] J. Stanojevic and R. Cote, "Many-body rabi oscillations of rydberg excitation in small mesoscopic samples," *Phys. Rev. A*, vol. 80, p. 033418, 2009.

[104] T. G. Walker and M. Saffman, "Consequences of zeeman degeneracy for the van der waals blockade between rydberg atoms," *Phys. Rev. A*, vol. 77, no. 3, p. 032723, 2008.

[105] J. Deiglmayr, M. Reetz-Lamour, T. Amthor, S. Westermann, A. L. de Oliveira, and M. Weidemüeller, "Coherent excitation of rydberg atoms in an ultracold gas," *Opt. Comm.*, vol. 264, no. 2, pp. 293–298, 2006.

[106] H. Weimer, M. Mueller, I. Lesanovsky, P. Zoller, and H. P. Buechler, "A Rydberg quantum simulator," *Nature Phys.*, vol. 6, no. 5, pp. 382–388, 2010.

[107] S. Anderson, K. Younge, and G. Raithel, "Trapping rydberg atoms in an optical lattice," *Phys. Rev. Lett.*, vol. 107, no. 26, p. 263001, 2011.

[108] M. Saffman and T. Walker, "Analysis of a quantum logic device based on dipole-dipole interactions of optically trapped rydberg atoms," *Phys. Rev. A*, vol. 72, no. 2, p. 022347, 2005.

[109] Y. Dudin, F. Bariani, and A. Kuzmich, "Emergence of spatial spin-wave correlations in a cold atomic gas," *Phys. Rev. Lett.*, vol. 109, no. 13, p. 133602, 2012.

[110] C. Monroe and J. Kim, "Scaling the ion trap quantum processor," *Science*, vol. 339, no. 6124, pp. 1164–1169, 2013.

[111] J. Volz, M. Weber, D. Schlenk, W. Rosenfeld, J. Vrana, K. Saucke, C. Kurtsiefer, and H. Weinfurter, "Observation of entanglement of a single photon with a trapped atom," *Phys. Rev. Lett.*, vol. 96, no. 3, p. 030404, 2006.

[112] T. Chanelière, D. N. Matsukevich, S. D. Jenkins, S.-Y. Lan, T. A. B. Kennedy, and A. Kuzmich, "Storage and retrieval of single photons transmitted between remote quantum memories," *Nature*, vol. 438, p. 833, 2005.

[113] M. D. Eisaman, A. André, F. Massou, M. Fleischhauer, A. S. Zibrov, and M. D. Lukin, "Electromagnetically induced transparency with tunable single-photon pulses," *Nature*, vol. 438, pp. 837–841, 2005.

[114] D. N. Matsukevich *et al.*, "Entanglement of remote atomic qubits," *Phys. Rev. Lett.*, vol. 96, p. 030405, 2006.

[115] J. Hofmann, M. Krug, N. Ortegel, L. Gérard, M. Weber, W. Rosenfeld, and H. Weinfurter, "Heralded entanglement between widely separated atoms," *Science*, vol. 337, no. 6090, pp. 72–75, 2012.

[116] S. Ritter, C. Nölleke, C. Hahn, A. Reiserer, A. Neuzner, M. Uphoff, M. Mücke, E. Figueroa, J. Bochmann, and G. Rempe, "An elementary quantum network of single atoms in optical cavities," *Nature*, vol. 484, no. 7393, pp. 195–200, 2012.

[117] A. Stute, B. Casabone, P. Schindler, T. Monz, P. Schmidt, B. Brandstätter, T. Northup, and R. Blatt, "Tunable ion-photon entanglement in an optical cavity," *Nature*, vol. 485, no. 7399, pp. 482–485, 2012.

[118] A. Acín, J. I. Cirac, and M. Lewenstein, "Entanglement percolation in quantum networks," *Nature Phys.*, vol. 3, no. 4, pp. 256–259, 2007.

[119] A. Mohapatra, T. Jackson, and C. Adams, "Coherent optical detection of highly excited rydberg states using electromagnetically induced transparency," *Phys. Rev. Lett.*, vol. 98, no. 11, p. 113003, 2007.

[120] P. Schauß, M. Cheneau, M. Endres, T. Fukuhara, S. Hild, A. Omran, T. Pohl, C. Gross, S. Kuhr, and I. Bloch, "Observation of spatially ordered structures in a two-dimensional rydberg gas," *Nature*, vol. 491, no. 7422, pp. 87–91, 2012.

[121] S. Tan, D. Walls, and M. Collett, "Nonlocality of a single photon," *Phys. Rev. Lett.*, vol. 66, no. 3, p. 252, 1991.

[122] C. Hong, Z. Ou, and L. Mandel, "Measurement of subpicosecond time intervals between two photons by interference," *Phys. Rev. Lett.*, vol. 59, no. 18, p. 2044, 1987.

[123] B. Hessmo, P. Usachev, H. Heydari, and G. Björk, "Experimental demonstration of single photon nonlocality," *Phys. Rev. Lett.*, vol. 92, no. 18, p. 180401, 2004.

[124] O. Firstenberg, C. S. Adams, and S. Hofferberth, "Nonlinear quantum optics mediated by rydberg interactions," *arXiv preprint arXiv:1602.06117*, 2016.

[125] I. Beterov, M. Saffman, E. Yakshina, V. Zhukov, D. Tretyakov, V. Entin, I. Ryabtsev, C. Mansell, C. MacCormick, S. Bergamini, *et al.*, "Quantum gates in mesoscopic atomic ensembles based on adiabatic passage and rydberg blockade," *Physical Review A*, vol. 88, no. 1, p. 010303, 2013.